EXPERIMENTAL INVESTIGATION OF NOVEL DESIGNS FOR AERODYNAMIC FLOW CONTROL OVER AIRFOILS

A Dissertation
Submitted to the Graduate Faculty
of the
North Dakota State University
of Agriculture and Applied Science

By

William Refling

In Partial Fulfillment of the Requirements
for the Degree of
DOCTOR OF PHILOSOPHY

Major Department:
Mechanical Engineering

April 2024

Fargo, North Dakota

North Dakota State University
Graduate School

Title

EXPERIMENTAL INVESTIGATION OF NOVEL DESIGNS FOR AERODYNAMIC FLOW CONTROL OVER AIRFOILS

By

William Refling

The Supervisory Committee certifies that this ***disquisition*** complies with North Dakota State University's regulations and meets the accepted standards for the degree of

DOCTOR OF PHILOSOPHY

SUPERVISORY COMMITTEE:

Dr. Jordi Estevadeordal
Chair

Dr. Y. Bora Suzen

Dr. Yan Zhang

Dr. Adam Gladen

Dr. Jason Boynton

Approved:

04/12/2024
Date

Dr. Chad Ulven
Department Chair

ABSTRACT

This study investigated three innovative flow control strategies to enhance the aerodynamics of rotorcraft wings, specifically using the Boeing-Vertol VR-12 and NACA 0012 airfoils. The research focused on active and passive control methods employing smart materials and structural adaptations to manage airflow effectively.

The first two strategies employed active controls integrating macro fiber composites (MFCs), a type of piezoelectric actuator, placed at the 25% and 85% chord lengths on the VR-12 airfoil. These actuators facilitated two approaches: morphing of the airfoil's leading and trailing edges to alter its shape during flight, and to use the piezoelectric actuator to perform and acoustic resonance.

The third strategy involved a passive control using a microcavity structure on the pressure side of the leading edge of a NACA 0012 airfoil. This design aimed to reduce transient separation and dynamic stall by subtly altering the airfoil's surface topology to influence airflow.

These systems were tested under two conditions in an open-loop wind tunnel within an advanced flow diagnostics lab at NDSU. Firstly, the airfoils were examined in a static state with a consistent freestream velocity. Secondly, they underwent dynamic testing through sinusoidal pitching motions to simulate real flight dynamics.

The effectiveness of these strategies was analyzed using two-dimensional particle image velocimetry, an optical diagnostic method that captures flow dynamics across the airfoil surface. This technique was crucial in providing detailed insights into the flow patterns during various test conditions.

Results indicated performance enhancements across all strategies. The active morphing strategy proved most effective, maintaining airflow attachment throughout the pitch tests and

showing a marked improvement over traditional droop techniques. The acoustic resonator also improved performance in both static and dynamic conditions, although its efficacy varied with changes in the angle of attack, necessitating frequency adjustments. The passive cavity structure demonstrated modest benefits during mild dynamic stall scenarios but was limited by the current experimental setup for more conclusive validation.

Overall, these novel flow control strategies show promising potential for improving aerodynamic performance in rotorcraft applications, with active morphing and acoustic modifications offering notable benefits over traditional methods.

ACKNOWLEDGMENTS

The author would like to thank the Mechanical Engineering Department at North Dakota State University for the continued support, as well as the defense committee members Dr. Jason Boynton, Dr. Adam Gladen, Dr. Y. Bora Suzen, Dr. Yan Zhang and principle advisor Dr. Jordi Estevadeordal for the continued support and direction given over the years. Further thanks are needed to be extended to both Dr. David Gonzalez of the Office or Naval Research and Dr. Miguel Visbal and Dr. Daniel Garmann of the Air Force Research Laboratories. Without the funding and knowledge shared this work would not be possible.

Additionally, the author would like to extend thanks to Rob Sailer and Francisco Valenzuela within the Mechanical Engineering department for the assistance in fabrication of various components. In addition to Rob and Frank, thanks are owed to Dr. Al Habib Ullah, Ellen Steffes, Joshua Yurek and Dr. Charles Fabijanic for their contributions in data collection and completing a fully controllable pitching mechanism. Thanks, is also needed to be extended to Dr. Erin Gillam, Professor of Biological Sciences at NDSU, for her time and use of the Avisoft sound recording equipment. Without it the acoustic measurements of the LEAR system would not be possible.

Lastly the author would like to acknowledge his father Charles Refling. Who took the time to assist in data collection during various holidays, as well as inspiring the author to follow in his footsteps and pursue a mechanical engineering degree.

DEDICATION

The author would like to dedicate this paper to his wife Chandler and his parents Kathleen and Charles Refling. Without their support, this work would not have been possible.

TABLE OF CONTENTS

LIST OF TABLES

LIST OF FIGURES

LIST OF SCHEMES

LIST OF ABBREVIATIONS

LE.....Leading Edge

TE.....Trailing Edge

PIV .....Particle Image Velocimetry

IMU.....Inertial Measurement System

PCB.....Printed Circuit Board

DOF.....Degree of Freedom

LSB .....Laminar Separation Bubble

TEV.....Trailing Edge Vortex

DSV.....Dynamic Stall Vortex

LEAR .....Leading Edge Acoustic Resonance

AoA.....Angle of Attack

DEHS .....Di-Ethyl-Hexyl-Sebacate

PTU .....Programable Timing Unit

PWM.....Pulse Width Modulation

MFC .....Microfiber Composite

PLC .....Programmable Logic Circuit

WEDM.....Wire Electric Discharge Machining

LIST OF SYMBOLS

Re .....Reynolds Number

U, V .....Velocity

V_∞ .....Freestream velocity

L .....Characteristic length

k.....reduced frequency

ω .....angular velocity

f, F .....frequency

C .....Chord length

S .....Arclength from center chord

A.....Amplitude

α .....AoA

$\emptyset$ .....Phase offset

Θ.....Droop angle

D.....Depth

St .....Strouhal number

M .....Mach number

LIST OF APPENDIX FIGURES

1. INTRODUCTION

In the forefront of aerospace engineering, airfoil technology stands as a critical component in the quest for enhancing aircraft performance, safety, and efficiency. Among the myriad challenges faced in this domain, the phenomenon of airfoil stall presents a significant hurdle. Airfoil stall, characterized by a sudden reduction in lift, poses considerable risks to flight safety and operational efficiency. The mitigation of stall effects through innovative control mechanisms is thus a research area of paramount importance.

This dissertation focuses on the exploration and evaluation of unique and cutting-edge methods for stall mitigation in airfoils, specifically through open-loop control strategies involving variable leading and trailing edge droop, microcavity systems, and leading-edge acoustic actuation. These methods represent a blend of passive and active control mechanisms, each with the potential to significantly alter the aerodynamic performance of airfoils under stall conditions. This research's objective is to provide a comprehensive analysis of these strategies, assessing their effectiveness, applicability, and potential integration into future airfoil designs.

The justification for this research is rooted in its potential to revolutionize airfoil technology, contributing to safer and more efficient flight capabilities. By advancing our understanding of these innovative stall mitigation strategies, the dissertation aims to pave the way for the development of more resilient aircraft capable of navigating the complexities of varied flight dynamics.

Integrating the proposed advanced diagnostics into a detailed research methodology that encompasses both theoretical analyses and experimental studies, this work is positioned to provide a comprehensive evaluation of the investigated methods. By employing advanced diagnostic tools for flow field measurements such as time-resolved particle image velocimetry

the study aims to delve deep into the complexities of active and passive control mechanisms for airfoils in unsteady flow fields [1-8]. The scope of this research is meticulously defined to concentrate on specific stall mitigation techniques, such as LE drooping, dynamic morphing of wing shapes using novel smart material actuators designs, and novel passive control strategies for LSB stabilization such as employing cavity flow resonances to produce LE Rossiter waves [9, 10] and acoustic resonance forcing employing MFC [Refling et al. 55]. This targeted approach ensures an impactful investigation into the potential of these techniques to significantly increase aircraft range, reduce drag, and enhance lift, while also reducing direct operating costs through improved cruise efficiency. The incorporation of the advanced diagnostics is crucial for supporting critical aircraft missions that require external lift of increasing payload weights, heightened operations in mountainous regions, and adaptive maneuverability within highly unsteady flows, such as ship air wakes encountered during shipboard landings. The subsequent sections will provide detailed insights into the techniques, their implementation for unsteady flows characterization and control, and the focus on both active and passive flow control strategies, marking an innovative approach to enhancing aerodynamic performance within the outlined research methodology.

Expected to make significant contributions to aerospace engineering, this dissertation enhances our understanding of stall and its management and aims to inspire further research and development in airfoil technology. Through the investigation of variable leading and trailing edge droop, microcavity systems, and leading-edge acoustic actuation, this research holds the potential to influence the future of aircraft design and operation, leading to advancements in safety, efficiency, and overall flight performance.

1.1. Motivation

This research aimed to design, manufacture and evaluate passive and active control strategies for airfoils used in both fixed wing and rotary aircraft. Both fixed and rotary winged aircraft experience steady and unsteady flow conditions, whether it is in the form of cruising flight such as a commercial airliner or actively changing flow fields. As such much work has been spent on the improvement and development of various airfoil geometries to improve the performance of an airfoil for these various operations. Active or passive control strategies provide the opportunity extend the performance of these various airfoil geometries throughout their operations. Active control strategies can manipulate their shape or introduce disturbances in the flow to allow for adjustment and optimization to match conditions experienced by the airfoil. Whereas passive systems are much akin to a new geometric design. Where modification of existing geometries can improve the performance of the airfoil throughout a range of scenarios. This research aims to introduce and showcase three such systems two active control strategies and one passive. The following text will discuss the design of the strategies as well as the methodology to validate their effectiveness.

1.2. Research Focus

The three primary areas of focus are active airfoil design, passive airfoil design, unsteady aerodynamics measurements. Each of these areas will be discussed in detail throughout the paper but a summarization of the intended outcomes are as follows:

- Modified existing wind tunnel by adding a diffuser to the test section within the advanced flow diagnostics laboratory to allow for increased velocity and minimized turbulence.

- Designed and developed a positional control system that allows for repeatable angle of attack positioning between 90 to –90 AoA. While also allowing for repeatable pitching between two AoA at a maximum pitching frequency of 40 Hz.
- Fabricated four statically deformed VR-12 airfoils including a baseline model
- Designed, developed, and built a novel active morphing leading and trailing edge airfoil through smart material. With on board processor and inertial measurement system providing feedback control of the LE and TE positions.
- Designed, developed, and built two passive micro-cavity geometries.
- Pioneering a new methodology for precision fabrication of said geometries
- Designed and developed a novel leading-edge acoustical resonance system (LEAR)
- Performed particle image velocimetry measurements to demonstrate performance in both steady and unsteady capabilities of:
    - Statically deformed
    - Microcavity
    - Active Morphing Airfoil
    - Leading Edge Acoustical Resonance (LEAR)
- Identified locations for sensor placement to allow for true closed loop feedback system for the morphing airfoil
- Determined the operational limitations of the current wind tunnel to fully detect the passive micro-cavity system benefits (deep stall mitigation)

2. LITERATURE REVIEW

In this section a discussion of the backgrounds and theories of these various systems will be elaborated. First the topic of what steady and unsteady aerodynamics is will be covered. Addressing the background fluid dynamics theory on separation needed for better understanding of the research. A breakdown of the various types of methods attempted to modify airfoils geometry or flow manipulation will be discussed. With a final discussion associated with theory associated with how data was collected primarily through the use of PIV.

2.1. Leading Edge and Trailing Edge Aerodynamics

The primary flow regime that that this study is focused on is the Reynolds number regime R_e <500,000 based on the wing chord length. At these low-moderate Reynolds numbers, the effect of the boundary layer is paramount. As such a description of the phenomena at work will be described in the following section. Stall in low Reynolds incompressible flow is primarily caused by the deterioration of the boundary layer. This is caused by the development of the laminar separation bubble within the boundary layer, due to adverse pressure gradients. These pressure gradients cause a separation to occur and small recirculation or vortex to form. [11-15] Figure 1 below shows this reverse flow vortex. The flow preceding the start of the is primarily laminar. Once this bubble is formed due to the adverse pressure gradient the flow can be broken into two main sections, where the dividing line WJ'R separates the slow recirculation or laminar separation bubble from rest of the flow within the boundary layer. The remaining flow between the line W"J"R" and WJ'R is the free shear layer. This free shear layer is where the flow traverses over the recirculation region encounters a transition from laminar to turbulent. The flow may reattach or it may separate causing a large region of separation to occur. As such much of

the work conducted in flow manipulation is focused on stabilizing this LSB or effectively removing it, by causing a tripping of the boundary layer to turbulent regime.

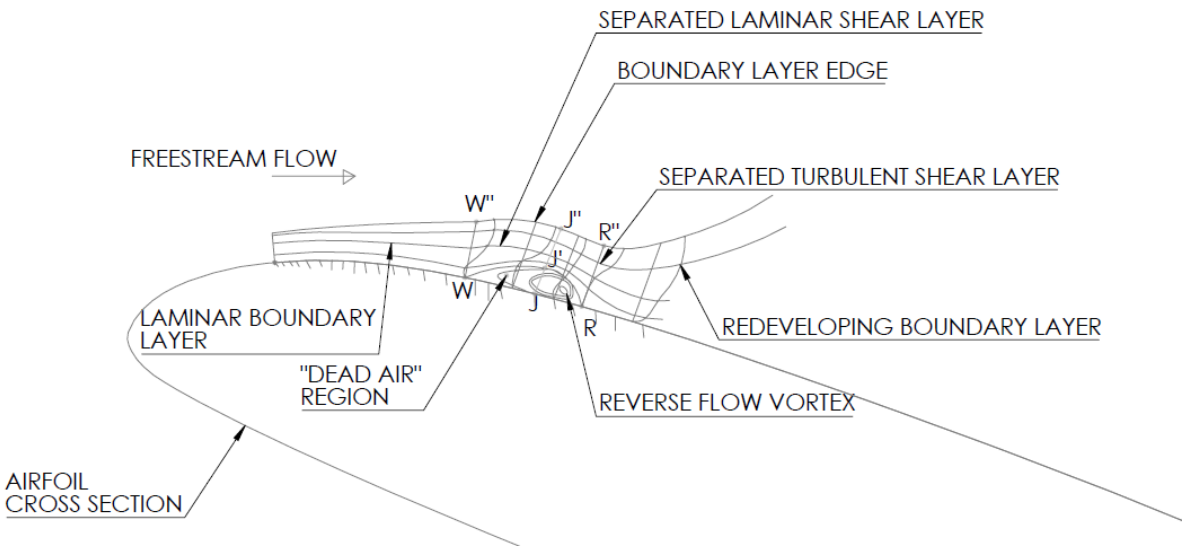

Figure 1. Section view of laminar separation bubble.

Depending upon the effects of the LSB on the free shear layer, vortex shedding may occur. To define this shedding the usage of the Strouhal number can be used given by the equation:

$$S_t = \frac{fL}{U} \tag{1}$$

Where f is the frequency at which of the vortexes, L is the characteristic length and U is the free stream velocity. Most commonly known for the vortex shedding that occurs from wind over a wire causing it to sing. The Strouhal number will play a part on the effect of dynamic stalls.

The details of airfoil aerodynamics have been studied extensively [12-15]. Basically by design of the airfoil the flow is intended to travel faster over the top surface (suction surface) of the airfoil than the lower surface(pressure surface), if the upper surface has a longer path the flow will have to travel at an increased velocity when compared to the lower surface due to mass

continuity. This higher speed on the upper surface has a lower dynamic pressure than the lower surface and lift is generated due to the pressure difference between the two surfaces. One other effect this pressure causes, is the slippage of fluid from one side to the other at the leading or trailing edges. This low pressure induces flow from high pressure to the low. At the trailing edge this slippage causes a recirculation referred to as the trailing edge vortex. Details pertinent to this dissertation on the separation phenomena along the wing and stall process can be found in recent literature [10-11]. These details will be discussed herein.

2.2. Flow Manipulation

Flow manipulation or (flow control) is the methodology of applying some additional stimulus to fluid flow over or before the airfoil. This can be done by a number of means such as:

- Excitation of the fluid flow over an airfoil through a high voltage ionizing ('plasma') system that increases the energy of the air molecules exciting them to higher speeds. [19-20]
- Zero- net mass flux jets, where a piston cylinder style device creates a low suction area pulling mass into the cavity and then blowing the said mass back out into the flow disturbing the flow and causing turbulence [16-18]
- Tripping devices such as the dimples on the golf ball, vortex generators, etc.
- Geometry changes to the airfoil such as; slats, flaps, LE extensions, TE extensions, or compliant manipulations. [28-34]
- Vibro-acoustics systems [52-54]

The common theme amongst all of these systems is the attempt to avoid the creation of a separation and recirculation of the flow from the airfoil. This can be contributed to either disturbing the viscous sublayer where adverse pressure gradient in the boundary layer causes

flow separation or increasing the amount of flow increasing the Reynolds number at a given location.

All of these systems can be categorized with two main distinctions, these being passive and active. Where passive systems will operate the same whether the airfoil undergoes a change in the flow conditions or not. Active systems are able to be modified or manipulated actively to adjust depending upon the conditions that occur. It is worth noting that these definitions are much like a square is a rectangle, an active system can be operated passively but a passive system cannot be actively controlled.

2.2.1. Passive Manipulation Microcavity Control

Passive flow control methods have the positive impact of not requiring external control and energy to produce better performance, the performance increase is vastly limited [10]. Dynamic stall and pitching wing research implementing a novel cavity producing Rossiter waves [11] show potential for increased performance by reducing or eliminating the dynamic stall vortexes (DSV) normally formed on the suction side of the leading edge. These DSV's roll down the suction surface and eventually coalesce with the trailing edge vortex. This event is seen on the downward sweep of the airfoil from its highest angle of attack and can be seen in figure 2 below [11].

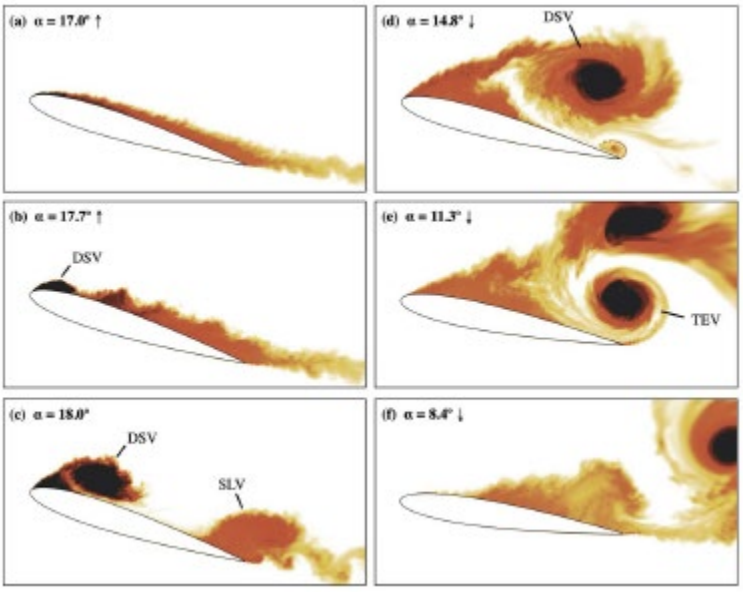

Figure 2. Contours of entropy for baseline NACA 0012 at select angles of attack [11].

Visbal et al, [11] proposed the introduction of microcavity to mitigate the transient separation and dynamic stall by means of a technique based on a properly sized and located microcavity located on the pressure side leading edge. This cavity is positioned such that it is ahead of the stagnation point of the point of the flow on the wing at high angles of attack. The flow that occurs over the cavity is of higher speed and generates a resonance within the cavity. These resonances act as a perturbance that is around the leading edge and through the boundary layer to the laminar separation bubble (LSB). The disturbances are amplified by the LSB and if designed correctly to match the naturally occurring Rossiter modes to the LSB frequencies, the LSB is delayed in bursting thus reducing or eliminating the DSV. Computational results including the micro cavity can be seen in figure 3 below [11].

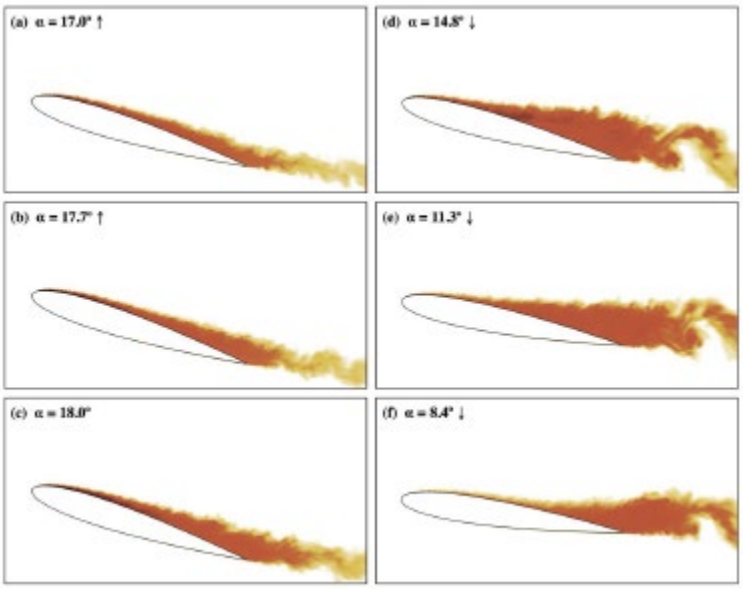

Figure 3. Contours of entropy at select angles of attack for airfoil with micro-cavity [11].

2.2.2. Active Manipulation Morphing Airfoils

Active control methods could ideally alter the object geometry and the flow properties by inducing small temperature, pressure, or electrical inputs into actuators in real-time to best correct the airflow for optimized performance under varying environmental flow conditions. As active flow control gained more interest in the past decades, different methods of achieving active flow control became popular research topics such as those based on flaps, synthetic jets, plasma actuators, etc. [19-20], and those based on shape changing airfoils [16-18]. Active flow control has also seen the impact of "smart" materials in fluid dynamics applications by incorporating Smart Memory Alloy's (SMA) [21-23,31-37], piezoelectric materials such as macro-fiber composites (MFC) [22,23], ionic polymer metal composites (IPMC) [17], and electroactive polymers (EAP) into the airfoils or even fabricating an entire airfoil out of smart materials [15, 16]. The different types of actuation have pros and cons and the main distinction between SMA and the other categories is that SMA offers more actuation amplitudes for significant geometric changes but at lower frequencies [18].

2.2.3. Active Manipulation Acoustic Resonance

Flow control using acoustics involves the manipulation of fluid flow characteristics through the application of sound waves. This is done by the interaction between the acoustic waves and fluid particles inducing vibrations or oscillations in the fluid flow. Due to its low intrusive nature has the benefit of allowing for control without physical contact. Techniques that have been used are surface mounted speakers or speakers directed at the flow of interest. By inducing fluctuations, the transition to turbulence can be accomplished, mitigating flow separation. [52-54]

2.3. Flow Diagnostics

In this section the main flow diagnostic methods based upon particle image velocimetry will be described.

2.3.1. Particle Image Velocimetry

Particle image velocimetry is used to characterize the flow field and its interactions with objects. It is able to provide quantitative values for the velocity, vorticity as well as the acceleration of the fluid flow. Acceleration measurement is possible if time resolved methods are used. This accomplished by seeding the flow field upstream of the test object with small particles. A laser sheet is used to illuminate the particles interaction with the flow and test object, and two images often referred to as frames are taken by use of high-speed cameras. The images are taken in quick succession with a known time period. These two images allow for correlation of particle motion, by means of a method called cross correlation. This methodology is used to measure the displacement between the particles and thereby measure the velocity [2,3].

3. METHODOLOGY

The following chapter will be broken into three sections. The first being the design and fabrication of the various models. The second explains the methods used to position and move the airfoil models to replicate various operating conditions seen in both fixed wing aircraft and rotorcraft. The final section will explain the advanced flow diagnostic techniques used to measure and quantify the performance of the models.

3.1. Airfoil Fabrication and Design

For all of the systems tested a baseline model was fabricated and tested as well. The purpose of this is to set a control for the experimentation and allow for a measurement of the improvements. There were two airfoil geometries used as baselines throughout. The first being the Boeing-Vertol VR-12, a non-symmetric variable camber airfoil. As well as a NACA 0012 airfoil, a symmetric airfoil. Four strategies were designed to manipulated the flow they are broken out and described as follows:

- Statically deformed
    - A statically deformed airfoil is defined herein as one where the geometry of the airfoil is permanently modified. This modification is a permanent deflection of a portion of the airfoil. The amplitude of the angle and the location of the deflection are further defined within the statically deformed section. The baseline airfoil geometry used for comparison was the VR-12.
- Active Morphing
    - Active morphing is defined herein as a mechanism that is able to actively modify the angle of deflection of a portion of the airfoil. I.e the amount of deflection is continuously variable, up to a predefined limit. The magnitude of the angle of deflection is a function of the angle of attack and the fluid flow that the airfoil interacts with. These limits correspond to the same maximum and minimum angles of deflection used in the statically deformed cases. The baseline airfoil geometry used for comparison was the VR-12.
- Micro Cavity
    - A Micro cavity is a small channel located along the span of the airfoil that is located at a strategic position along the pressure surface to achieve flow control. The use of the term micro is in reference to size of the geometry

formed. The channel is a permanent fixture and does not change. The baseline airfoil geometry used for comparison was the NACA 0012.

- Leading Edge Acoustical Resonance
    - The leading-edge acoustical resonance is a novel device that makes use of MFC's to generate vibrational waves that form acoustic radiation.

3.1.1. Statically Deformed

In line with the smart morphing approach, a model was made for each of the four designs listed in the following table with descriptions of each of the three deviations from the baseline VR-12.

Table 1. Statically deformed models built

Description	Locations of deflection along the chord (% of Chord)	Angle of deflection
Baseline	0	0°
Trailing Edge	85%	4°
Leading Edge	25%	6°
Combined leading and trailing edge	25% & 85%	6° & 4°

Of the four that were fabricated only one was machined without internal cavities. The intent of providing these cavities is to allow for the installation of pressure ports into the airfoil thereby allowing the measurement of the surface pressure via pressure transducers and implementation of a control loop to be described later. It did also present the opportunity for access to the inner surfaces for the eventual installation of the smart structure. The models with internal cavities were constructed of and upper and lower portion. The first model, the baseline, was designed with a snap lock feature. When pushed together the top and the bottom halves snapped together with interlocking parts. This system worked well, however the locking mechanism was able to be disengaged by flexing the upper and lower surface. This would be counterproductive for the project objectives. The second and third model were prepared with the

upper and lower portions. However, this system made use of two rods slid into holes located in the airfoil. The holes were formed by the combination of the upper and lower surface geometries. The rod would then not allow the removal of the upper portion from the lower without removal of the rod as can be seen in Figure 4. This would in turn allow for the deflection of the upper and lower system while still allowing them remain together. The last model that was made was of solid material, this was done due to current time constraints. All four models are shown below in Figure 5 with both the CAD drawing and the physical model shown.

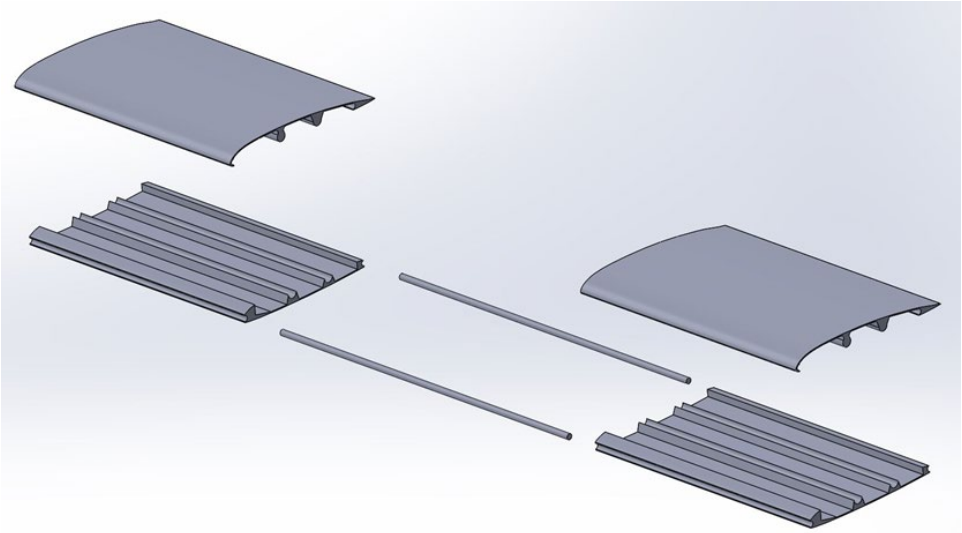

Figure 4. Exploded view of one of the trailing edge deflection assembly.

Figure 5. Comparison of the models as-built vs. drawn.

Each of the four models was fabricated out of 6061-T6 aluminum, done by a wire electrical discharge machine (WEDM). This methodology was chosen over traditional machining due to the complex features needed inside the airfoil. The thin side walls and complex curves would have proven to be difficult and time consuming to machine conventionally. Due to the length and simple profile when viewed from a 2-D perspective the WEDM seemed the best solution. Each upper and lower portion of the model was cut out of a 152.4 mm tall block of aluminum. The baseline model and the trailing edge model were made by combining these two 152.4 mm lengths to achieve the full 304.8 mm span. The four different internal geometries were modified as each configuration was made

3.1.2. Active Morphing Airfoil

The Boeing VR-12 was selected due to is abundant use in rotorcraft industry. With many references to its modification to both its leading edge and trailing edge [28-31]. Most of these modifications were done by means of a flapping mechanism with notable exceptions using other methods such as leading-edge drooping [25]. As such, more effort could be expended on developing the morphing mechanism and the control if an airfoil with known performance was chosen. Sprengeler et al [24]. provided the basis for the locations of the deflection for both the leading edge and the trailing edge. Examples of the various angles of the leading edge and trailing edge droop can be seen below in figure 6. Their work is expanded upon by the use of computational fluid dynamics to provide quick analysis of multiple angles of deflection. To help reduce the computational time initial assessment XFLR5 was used to quickly identify leading edge and trailing edge deflection angles that provide improvements in lift, drag, and pressure coefficients (C_L, C_D, and C_p). From these calculations three shapes were identified for

experimentation. This work is thus done by a combination of numerical methods with details reported in Sprengeler et. al [24].

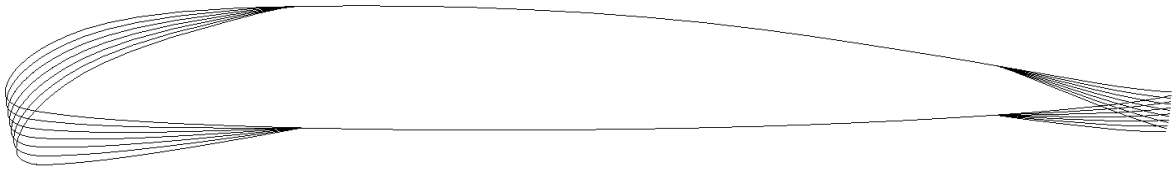

Figure 6. XFLR 5 variation of leading and trailing edged deflections of a VR-12 airfoil. [24**]**

Ultimately the XFLR5 results indicated a combination of deflection of the leading edge and trailing edge to provide the most aerodynamic improvements over a wide range of angles of attack -10 to 22°. These conditions being 6° for the leading edge with the pivot position being at the 25% of the chord line, as well as a 4° deflection of the trailing edge at 85% of the chord. The graphs of lift and drag coefficients calculated using XFLR5 can be seen below in figure 7 for a variety of combined leading and trailing edge deflections as well as the effects of independent trailing and leading-edge deflection. The combination of the 6° LE deflection and 4° TE deflection provides an increase in the coefficient of lift while maintaining a lower coefficient of drag. Furthermore, if the system was designed to independently deflect the leading and trailing edge further benefits could be capitalized on.

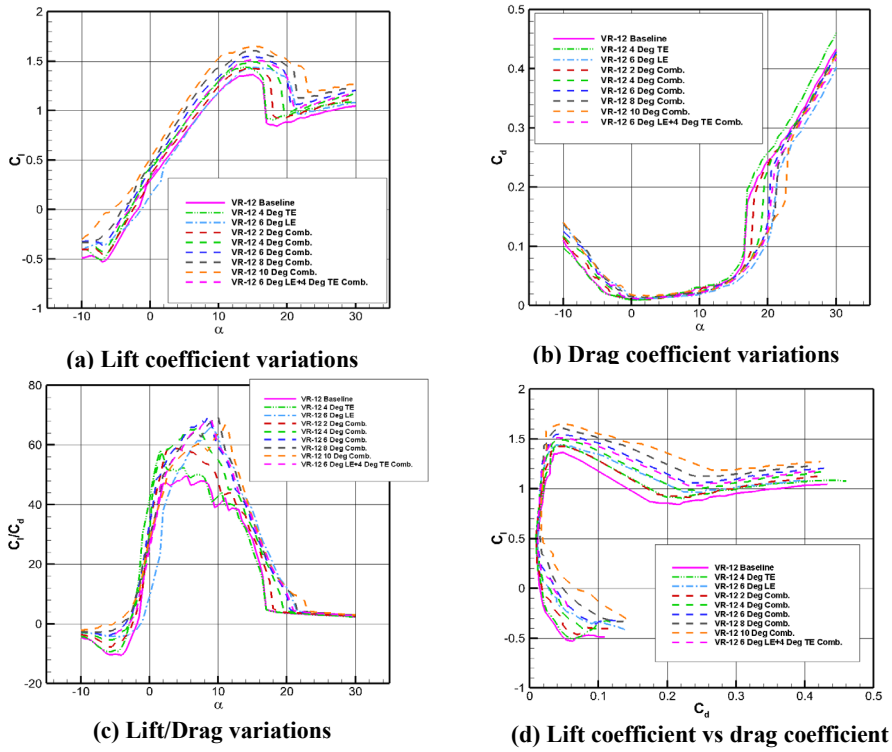

(a) Lift coefficient variations **(b) Drag coefficient variations**

(c) Lift/Drag variations **(d) Lift coefficient vs drag coefficient**

Figure 7. XFLR5 computation results for various leading and trailing edge deflection; coefficient of lift vs AoA (a) coefficient of drag vs AoA (b) ratio of coefficient of lift to drag vs AoA (c) and lift vs drag coefficient (d) [24].

Macrofiber Composites (MFC) were chosen for the actuation methodology for their quick response times, long life and their frequent use in other designs [22, 23]. The MFC's were assembled in a unimorph configuration by adhering their backside to the inside surface of the leading and trailing edge. This would then provide the out of plane bending to achieve the desired deflection. The leading and trialing edges are both able to be operated independently, by means of two separate bus bars fed 400 volts by two ENCO DC-DC converters. Images of the installation of the actuators to the respective leading and trailing edges can be found below. Both systems were tested prior to installation to the wind tunnel. The trailing edge deflection was successfully able to deflect. However, when the MFC's were adhered to the leading edge were sprung in the opposite direction. This was caused by the mechanism used to apply pressure while

the glue cured. The MFC's were still able to move the leading edge but not to the final location desired. Static testing of the leading edge could still be completed as the leading edge could be pinned into its deflected state. But a new airfoil was fabricated and assembled which can be seen the figure 8 below. Again, there are issues with the leading edge, as the deflection is getting hung up on the 3D printed parts that can be seen in the image of Fig. 8c.

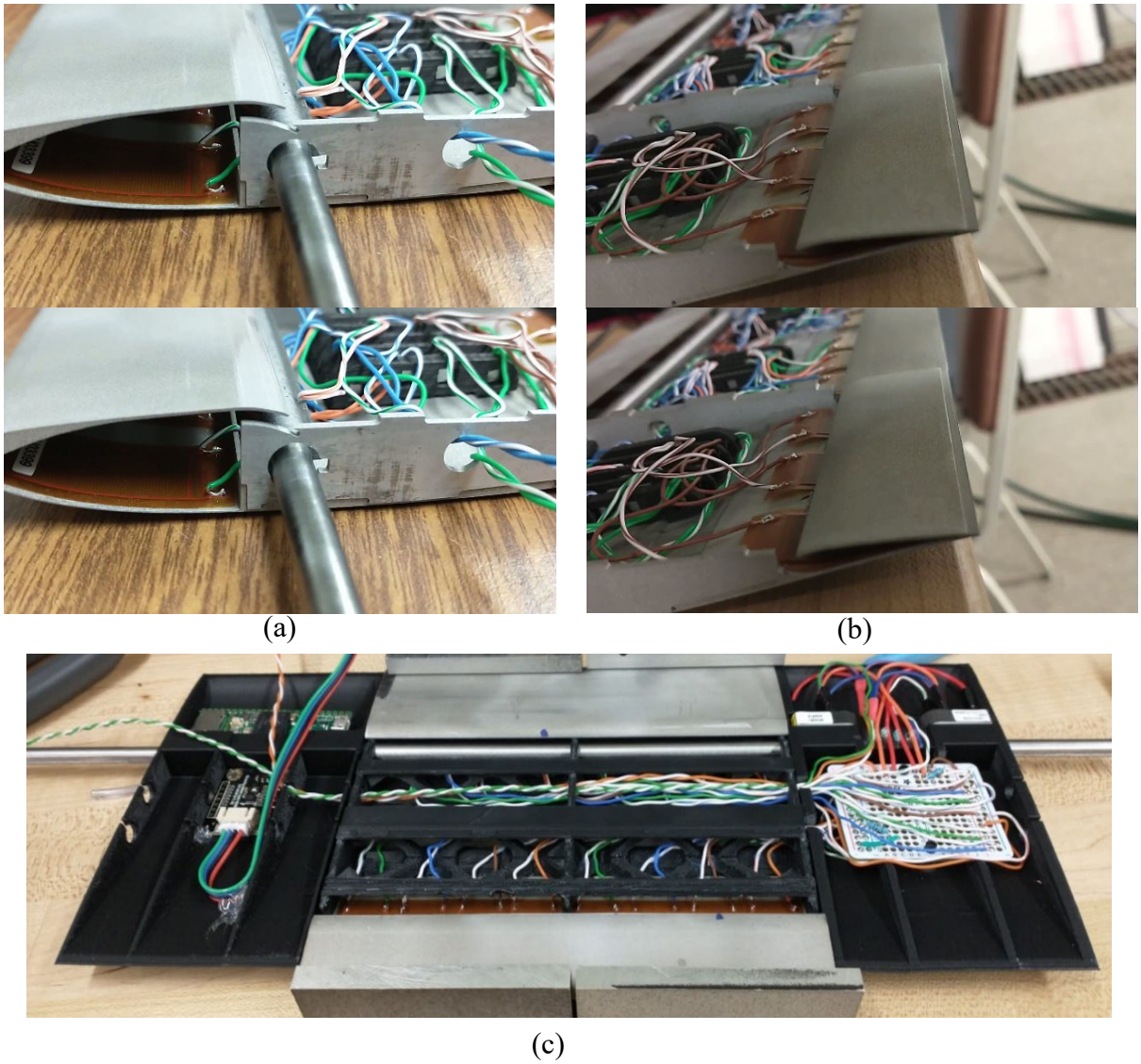

(a) (b)

(c)

Figure 8. Initial smart morphing airfoil deflection comparisons LE (a) TE (b) and the components integrated to the interior of the wing of the new smart morphing airfoil. (c).

While inspecting the 2nd iteration's interaction with the 3-D printed internal support structure it became apparent that the forces acting upon the leading edge by the MFC were causing a reaction of the LE to move more in the chord wise direction then thickness direction. The initial cause of this was determined to be the location of the actuator being close to the LE. To rectify this the position of the actuator was moved further along the chord direction, additionally the thickness of the skin was reduced from 0.015 in to 0.010 in. This change can be seen in figure 9.

The airfoil was tested on a bench and the PIV camera was used to image the displacement from an application of 500 volts to the actuators. The image capture software was used to measure the leading-edge tip and a deflection was measured to be 2.46 mm. The comparison of the two images can be seen in the image below.

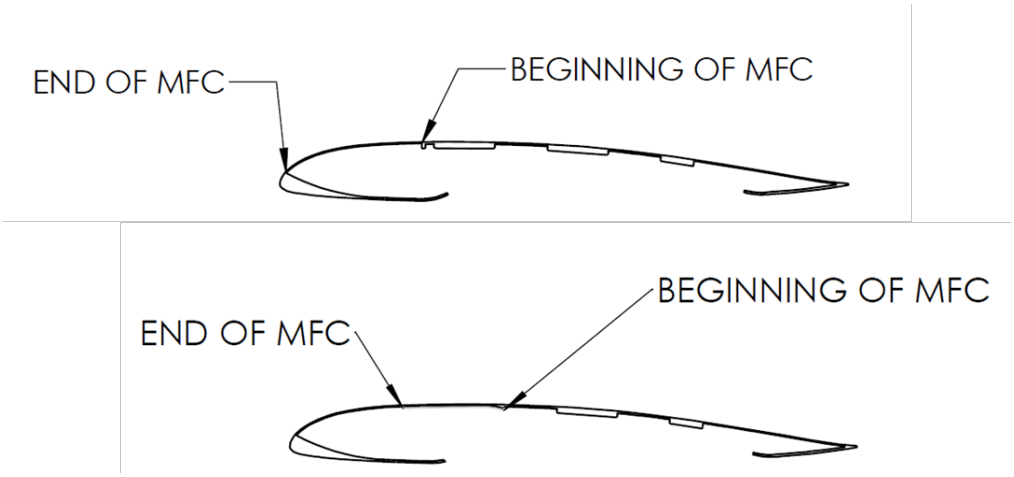

Figure 9. MFC location change between iterations.

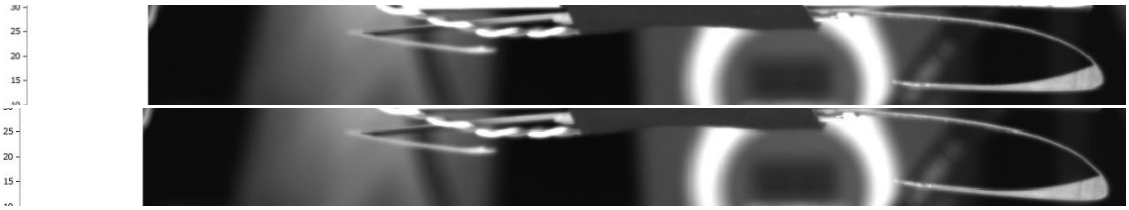

Figure 10. Deflection of LE at 500 Volts (Top) baseline, (Bottom) deflected.

When the system was fully assembled the same issue continued to persist where the LE bound on the internal ribs. It was at this point that the second cause of the bind was realized. It was due to the internal stresses of the raw aluminum billet used to fabricate the skin. These internal stresses come from the extrusion process of associated with making the aluminum billet, molten aluminum alloy is forced through a die to form the rectangular geometry. This molten aluminum cools in air and the crystalline structure forms and the aluminum contracts building large internal stresses in the block. When the EDM removes the material from the aluminum block it does not reduce the internal stresses, this is one of the allures of WEDM as it has little effect on the material being machined. These internal stresses cause the pressure surface of the LE to spring back on itself slightly, binding on the internal ribs. To counter act this a spacer was inserted into the LE to maintain the appropriate gap between the suction surface and the pressure surface. A compliant hinge was added to the structure to counter act the internal stresses that maybe pulling the LE down and to help guide the motion of the deflection. Lastly this hinge also acts to counter act any adverse forces caused by the momentum of the freestream interacting with the LE. The compete assembly can be seen in figure 11 below.

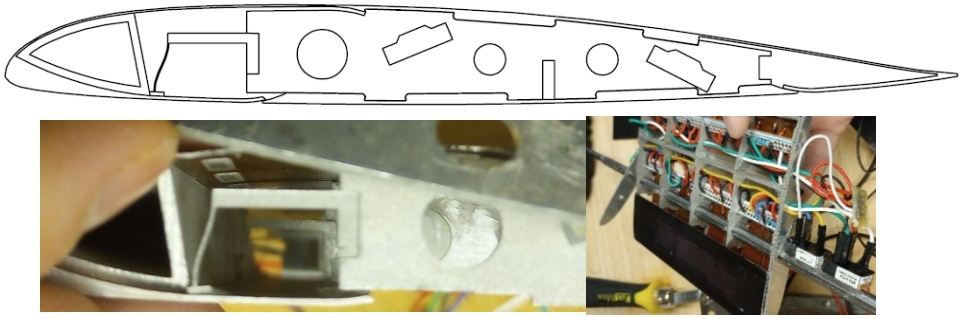

Figure 11. Morphing Assembly Photo, (Top) CAD image, (Bottom left) Complaint Hinge, (Bottom Right) Internal View.

These internal stresses could be resolved by annealing the aluminum block, but they are useful as they actively assist the LE to droop. However, this actually acted as a slight negative

during the glue process as slight amount of droop was not corrected. Causing the LE to be permanently stuck at a -2° angle. This is not ideal but part of the learning process, to counter act this in the future. A form that matches the exact airfoil geometry could be made to hold the system in its proper location, during the gluing procedure.

3.1.2.1. Morphing Implementation

An open loop feedback system was implemented to control the deflection of the leading and trailing edges. This achieved measuring the airfoils angle of attack with a 9 degree of freedom (DOF) Inertial Measurement Unit (IMU). A Bosch BMX160 9 DOF was selected for its size, robustness, and relative ease to implement. Preliminary tests indicated that a similar sensor, the Bosch BNO055 could not provide accurate angle measurements while the airfoil is pitching. A Teensy 4.1 microcontroller running Arduino IDE was utilized to read the 9 DOF IMU. A Mahony filtering algorithm was applied to the individual accelerometer, gyroscope, and magnetometer sensor readings being used to determine the sensor angle. The airfoils current angle was related to the percentage of deflection of the leading and trailing edge by the equations provided by Sprengeler et al. [24]

$$\theta_{LE} = \theta_{LEo} + A_{LE}\, cos(\, 2\pi f_{LE} t + \varphi_{LE}) \tag{2}$$

$$\theta_{TE} = \theta_{TEo} + A_{TE}\, cos(\, 2\pi f_{TE} t + \varphi_{TE}) \tag{3}$$

where equations 1 and 2 are time dependent equations for theta, the angle of deflection corresponding to the leading and trailing edges respectively as seen in Figure 12.

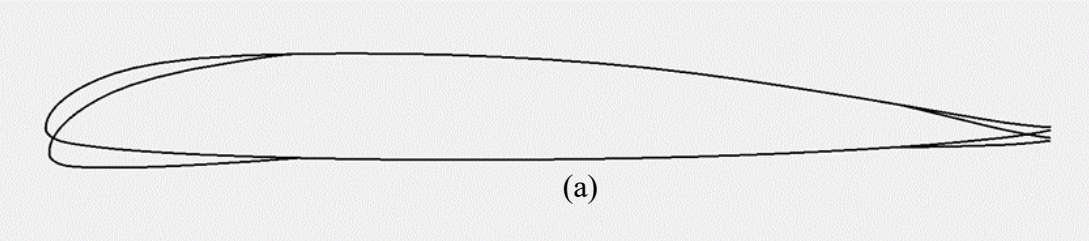

(a)

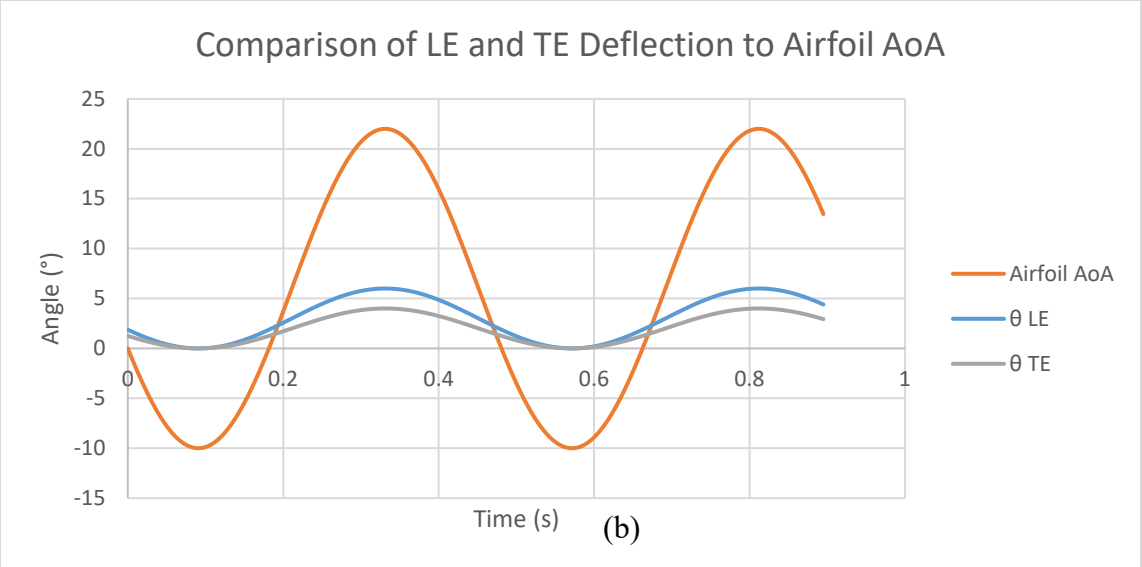

(b)

Figure 12. Expected Deformation as predicted by equations 1 and 2 at max AoA (a) and the comparison of AoA to deflection angles from equations 1 and 2 (b).

The actual control of the morphing mechanism will be done by means of pulse width modulation (PWM); an Arduino IDE program was written to vary the voltage applied to the MFC according to sensor feedback. Existing Arduino IDE functions are capable of simulating an analog output up to the full Voltage Common Collector (VCC) of the board, which is 5 V for the Teensy 4.1 development board. This is done by writing an 8 bit value (between 0 and 255) to specified PWM capable output pins which adjusts the frequency of the timer on Arduino such that 0-255 corresponds with 0-100% duty cycle. Two PWM pins were set up to individually output voltage to the leading and trailing edge MFCs based on the angle readings of the 9 DOF sensor. In accordance with equations 1 and 2, maximum and minimum VCC is programmed to occur at 18° and -10° respectively for the leading edge and -10° and 22° respectively for the

trailing edge. The program also accounts for potential angle exceedance of the specified operating range by maintaining the output voltage associated with the last detected angle in range. The frequency of output voltage from Teensy 4.1 is then fed into the dc-dc converter's built in switch. This switch then regulates the 5-volt line input to the converter which then causes the output voltage to increase; Table 2 shows a calibration of the output voltage, by means of the Teensy 4.1, The code used for this can be made available upon request at the discretion of the author.

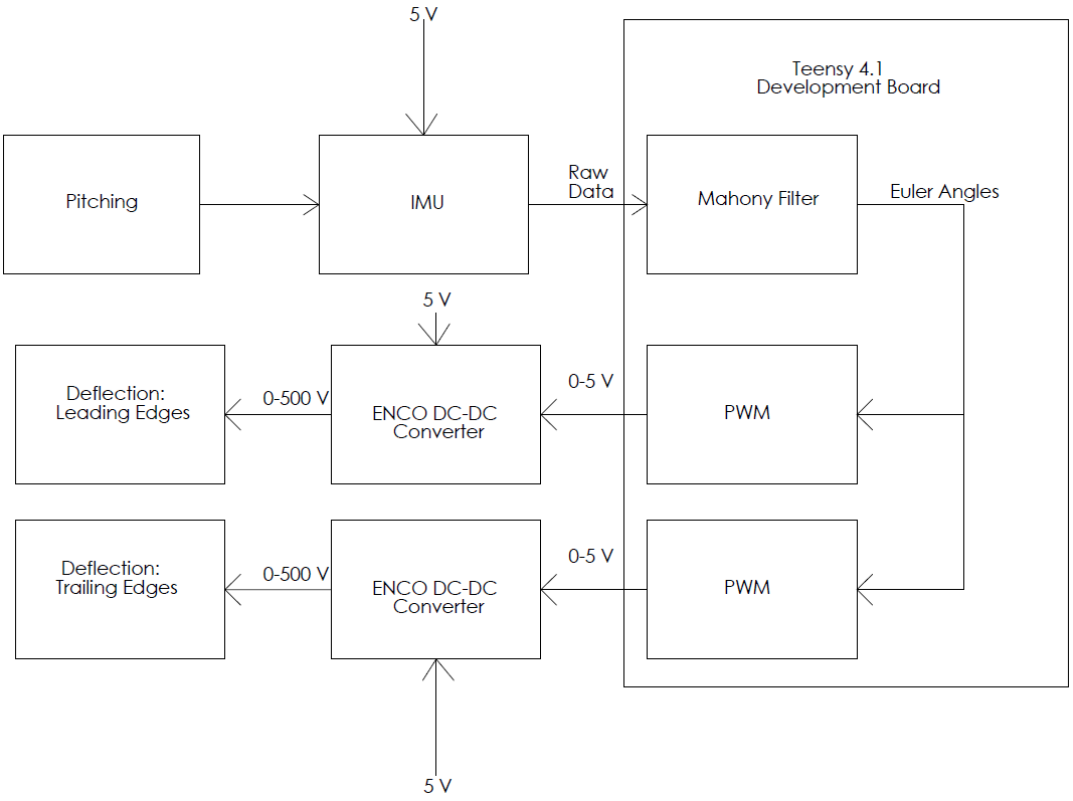

Schematic 1. Active morphing control schematic.

Table 2. Output Voltage Calibration

% of internal clock	DC-DC converter output voltage (V)
10	55
20	168
30	259
40	338
50	400
60	453
70	495
80	533
90	570
100	622

3.1.3. Flow Manipulations

The following section will specify the fabrication and design of two flow manipulation strategies, the first being a micro-cavity placed upon the pressure side of the leading edge. The second made use of MFC's was a novel implementation to generate acoustical radiation. These flow control methods make use of high frequency low pressure waves to stabilize the LSB. It is noted that these frequencies are on the order of 1-100 kHz.

3.1.3.1. Micro-Cavity

The NACA0012 airfoil profile was used to match the computational results presented by Visbal and Garmann's work [11]. Four wings in total were fabricated and tested, two configurations of the micro cavity as well as two baseline models. The geometry of the

microcavity was machined to the specifications presented in Visbal and Garmann's work [11]. Where the width, depth and placement of the cavity is dependent upon the chord. As shown in the following figure 13, where L/c=0.01, and s_1/c=0.01 with and aspect ratio of L/D=7. S_1 being the starting location of the cavity located along the surface of the pressure side of the airfoil, L being the length of the cavity and D being the depth. Lastly c is the chord length of the airfoil.

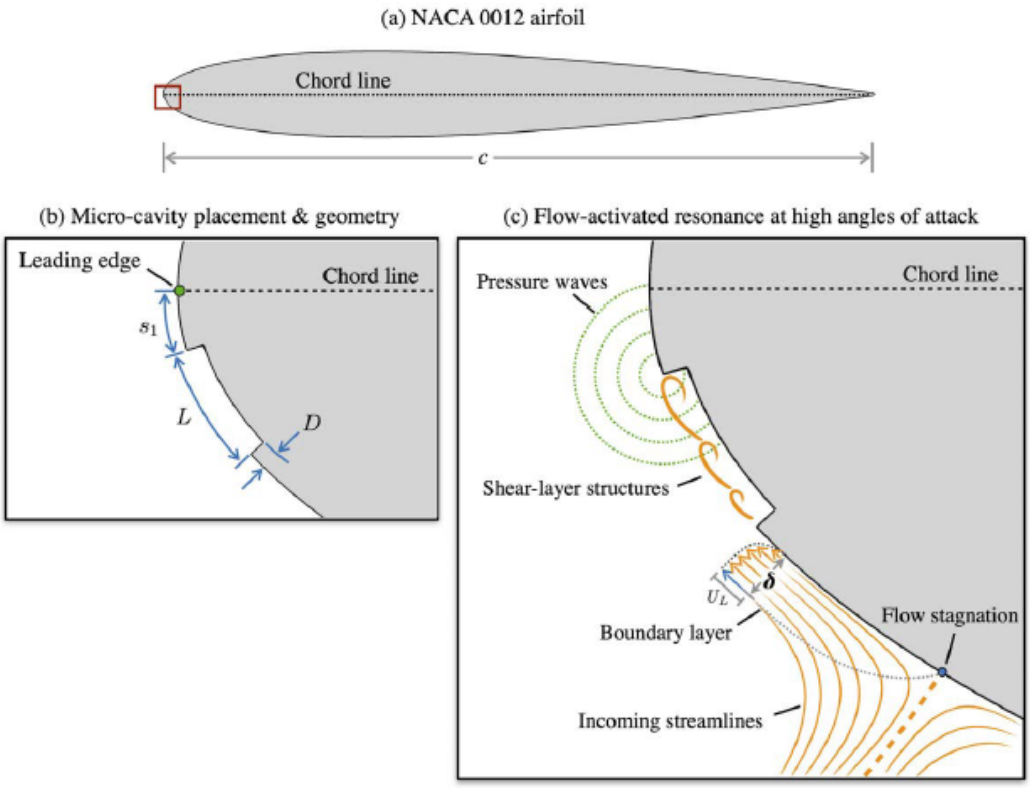

Figure 13. Micro-cavity actuator configuration [11].

Both airfoils were designed and constructed with a span of 304.8 mm and a chord of 127 mm. The span consisted of three sections. One section 152.4 mm in length is centered on a 7.9375 mm keyed shaft. Two 76.2 mm sections are placed on either side of the 152.4 mm section. There by providing a continuous test section for the PIV laser plane at the center of the 152.4 mm section. To minimize weight and to place the center of gravity at the zero-moment

location of 0.25 of the chord a cavity was cut from the interior of the airfoil. This added feature also allowed for the keying of the airfoil to the shaft as can be seen as can be seen in Figure 14 below where the calculated center of gravity is shown in pink.

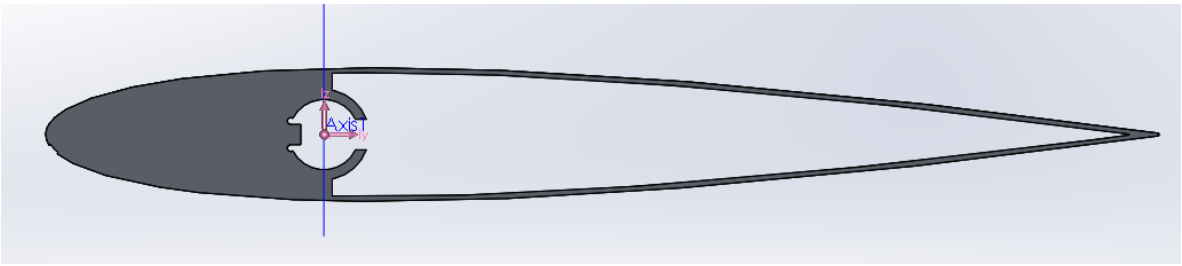

Figure 14. NACA0012 airfoil design with microcavity.

Details of the microcavity are shown in Figure 15 below where the location of the microcavity is positioned at 1.285 mm along the curvature of the pressure side from the leading edge. This same length is used for the cavity and was cut with an intended depth of 0.1778 mm. In an effort to provide as light of a test piece as possible, in addition to hollowness, 6061 aluminum was used for the material. All sections were machined out of solid extruded bars of aluminum using a Sodick ALN400G wire electro-discharge machine. A 0.1016 mm wire was used to machine the cavity, as shown in Figure 15. Deviation from the desired models occurred in fabrication of the first microcavity airfoil. This is due to the need to develop custom machining parameters for a 0.1016 mm wire through 152.44 mm of aluminum. As such some deviation from the model can be seen in the images of the as fabricated piece in Figure 16.

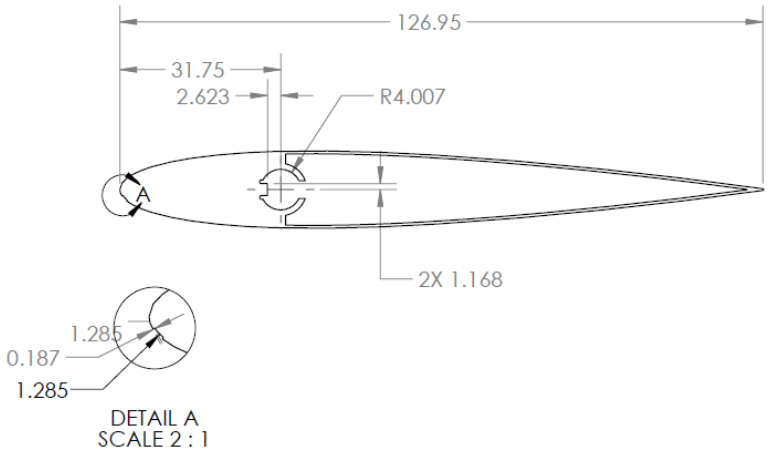

Figure 15. Dimensional details of the microcavity design for NACA 0012 airfoil.

The section of the microcavity airfoil was sliced off for measurement. The microcavity measurements were then completed using a machinist microscope with x-y plane measurement capabilities. It can be seen that the overall depth is larger at the beginning of the cavity at a depth of 0.2794 mm. The depth then reduces along the length of the cavity to a depth of 0.0762 mm. The beginning of the cavity is also slightly closer to the leading edge by 0.1016 mm, resulting in a length of 1.1938 mm. The length of the cavity was machined to 1.397 mm. Further refinement of the cut parameters will be a point of investigation to better match the CFD setup. The dimensions of the designed piece versus the machined dimensions are shown in Table 3.

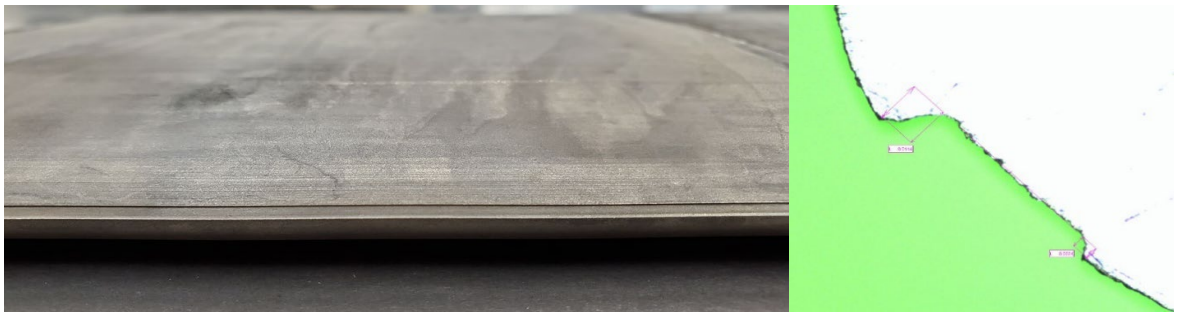

(a) (b)

Figure 16. Photography of leading edge with microcavity (a) and microscope image detail of the microcavity cross section (b).

Table 3. Dimensions of the first designed piece versus the machined dimensions

Description	Designed	Fabricated	Deviation
Distance to Cavity	1.285	1.1938	0.0912, 7%
Depth of Cavity	0.187	Max 0.2794, Min 0.0762	0.0924, 49% 0.1108, -59%
Length of Cavity	1.285	1.397	0.112, 9%

Initial testing indicated little difference in the performance between the micro-cavity and the baseline model. This was attributed to the deviations from the fabrication as can be seen in the table and images above. As such a new fabrication method is necessary to create more precise microcavities with consistent cavity geometry and sharp interior corners. To accomplish this the airfoil profile was fabricated in two pieces. A larger cavity and a core piece that would slide into the enlarged core. Thereby providing sharp edges. The details and configurations can be seen below in figure 17. This new airfoil has been tested and the results are shown in the microcavity results section.

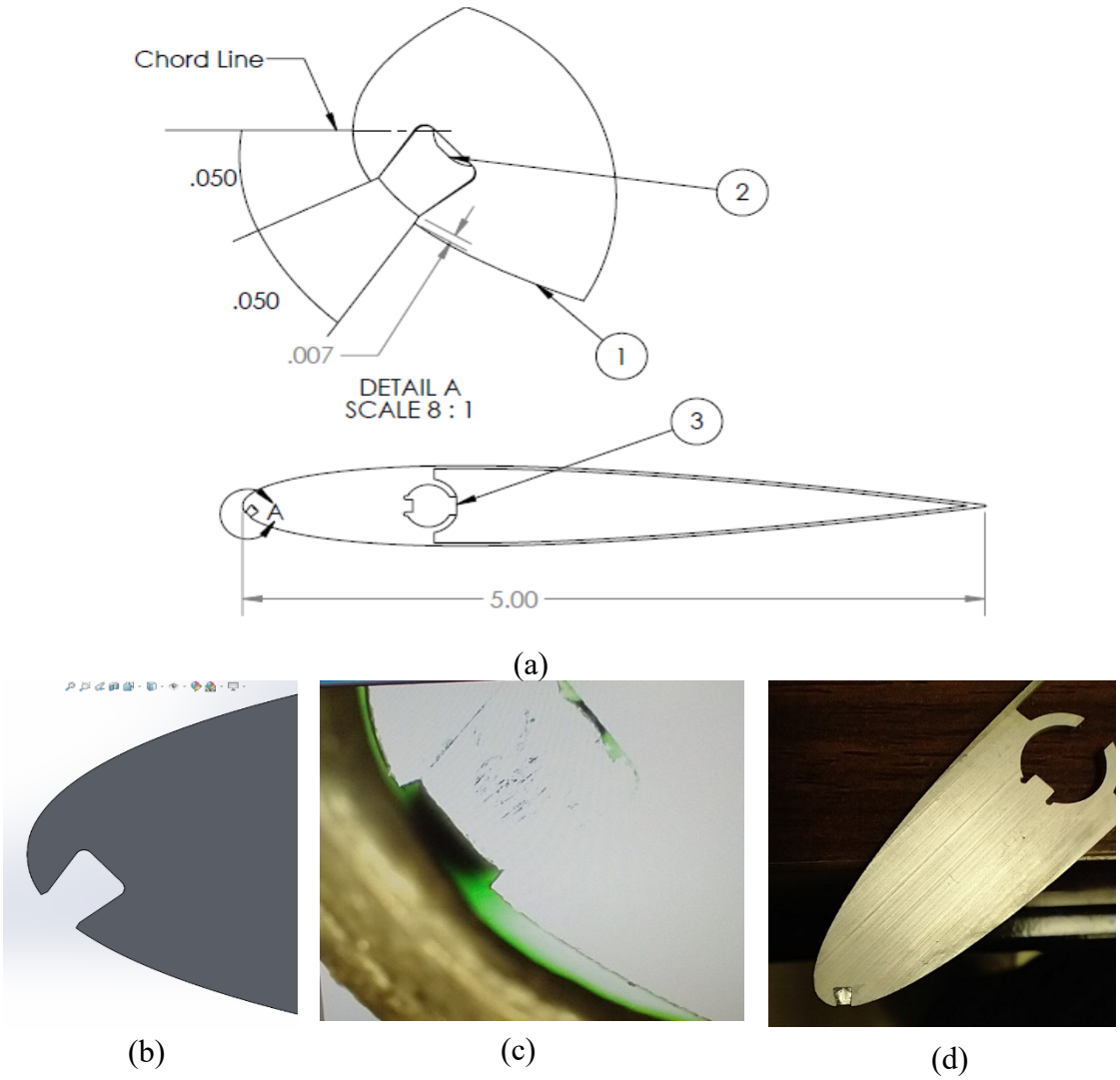

Figure 17. New design of microcavity with insert to sharpen geometry edges: drawings(a), Solidworks detail (b), Microscope image (c), and photography (d).

One additional configuration was made, first the chord length was increased to 152.4 mm to allow for a larger cavity geometry thereby making manufacturing easier. The position of the cavity was also changed to improve the performance of the system, as there were concerns that the deviation in our flow conditions from those used in the simulations, was not allowing the cavity to resonate creating the pressure waves that would stabilize the LSB. This will be further

discussed in the results and discussion section of the paper. The new geometry and its fully assembled airfoil can be seen in the following figure 18.

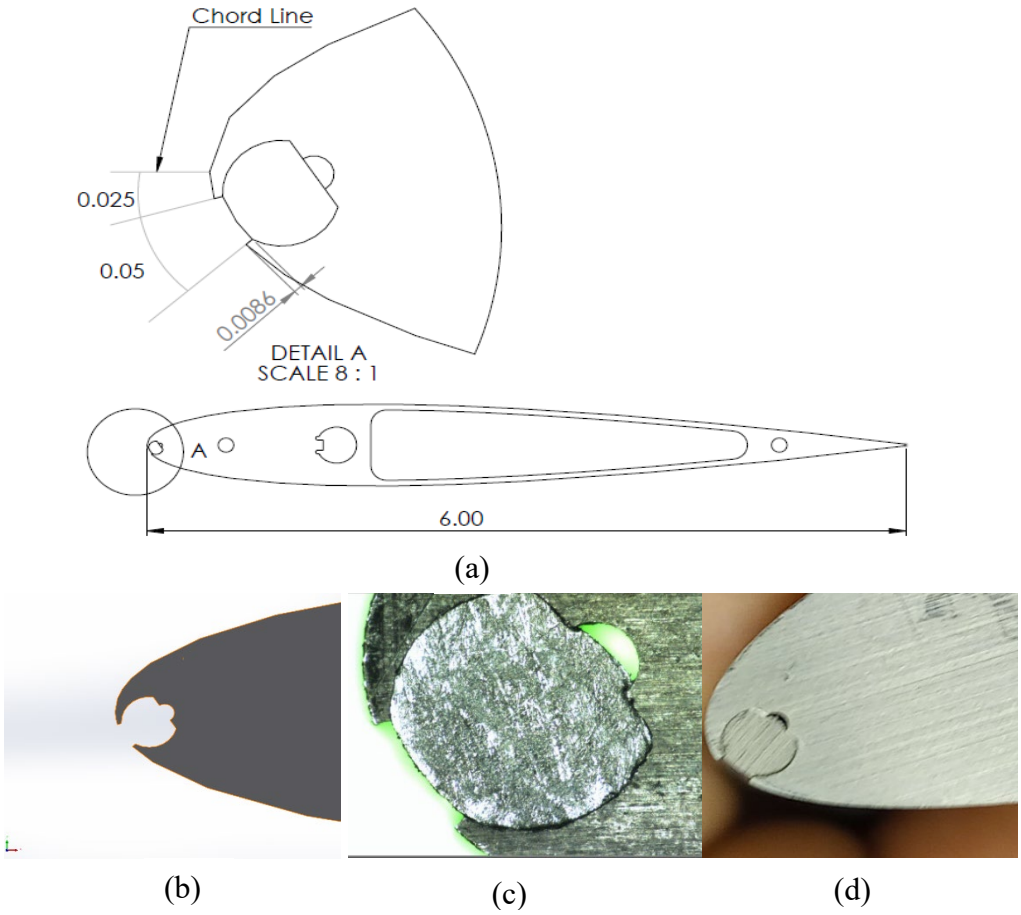

Figure 18. New design of microcavity with insert to sharpen geometry edges: drawings(a), Solidworks detail (b), Microscope image (c), and photography (d).

3.1.3.2. Novel Leading-Edge Acoustical Resonance

The proposed effect of the microcavity is the generation of small pressure waves that exit the cavity and curve around the leading edge and stabilize the LSB preventing bursting. The downside to the microcavity methodology is the need to match flow conditions to the cavity geometry and location. It was noticed that MFC's generate sound waves from audible to high frequencies. Thus, to generate an active control system another small pressure wave will be

generated using the MFC's. To accomplish this task MFC's will again be used, due to their ability to be actuated at high frequencies they are the perfect candidate to generate sound waves. To do so a function generator was used to generate the high frequency low voltage signal 20 volts peak to peak, a wiring diagram is provided below.

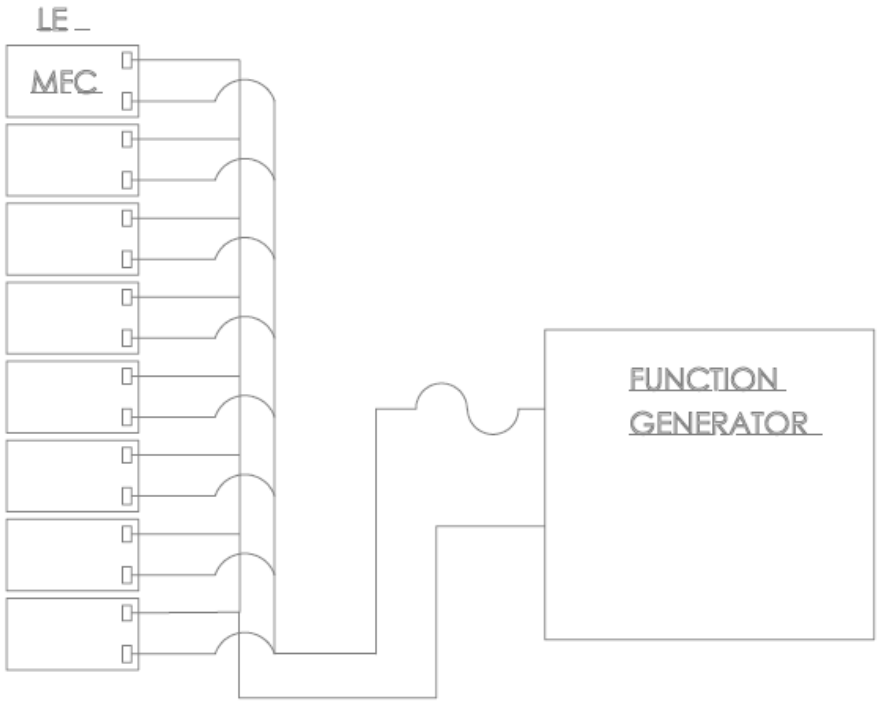

Schematic 2. LEAR MFC to function generator wiring diagram.

To test this theory the second iteration of the active morphing airfoil was recycled for use in this test. Two new 76.2mm sections were 3-D printed and mounted on either end of the center test section and can be seen below. The leading edge was pinned in place by use of glue to prevent the leading edge from vibrating during testing.

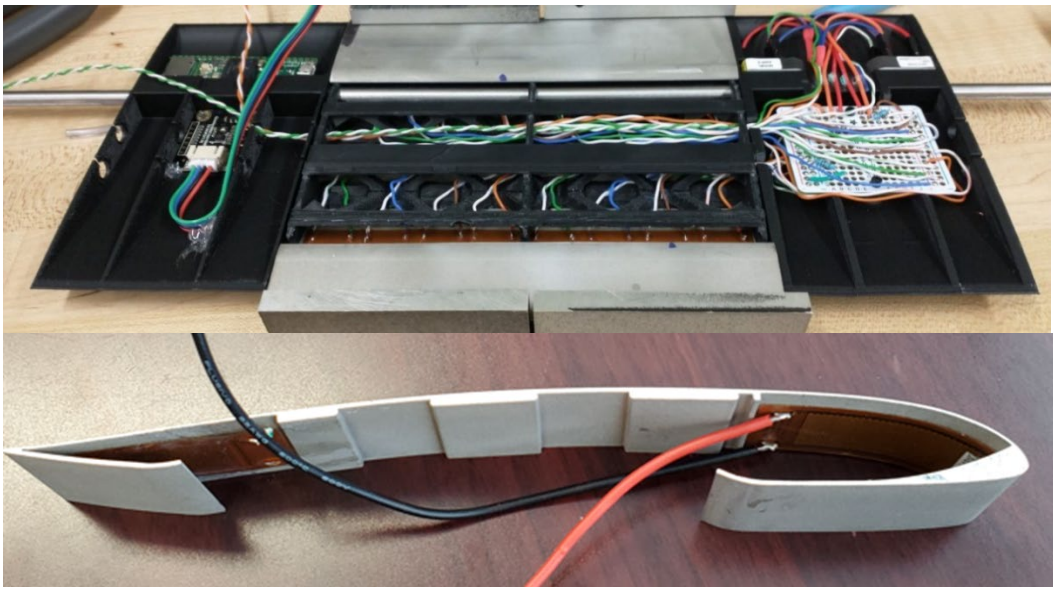

Figure 19. Interior view of the electrical circuitry associated with the LEAR (Top) MFC actuator placement (Bottom).

To ensure that the results of these tests were due to the resonant frequency of the MFC's and not due to motion of the leading edge a measurement was conducted using a Brown and Sharpe dial indicator with a resolution of 1.27µm. The dial indicator was placed on the leading edge with a preload and measured displacement of 25.4µm. The function generator was then turned on and ran through a range of 1-21 kHz. No movement of the dial indicator was seen. Indicating any fluctuation caused by the MFC to be less than.1.27 µm. The test setup can be seen below.

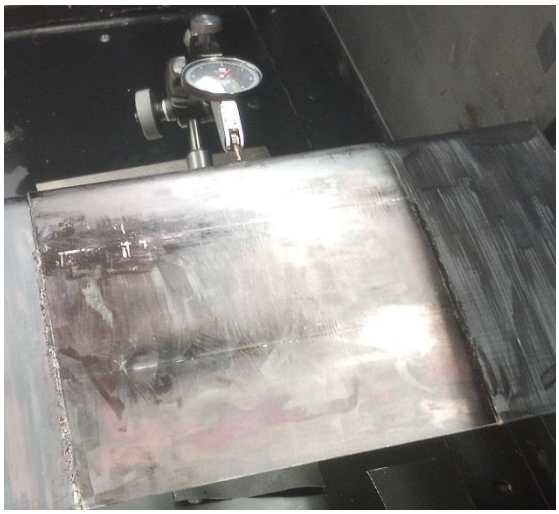

Figure 20. Dial indicator test setup within the wind tunnel.

The sound waves were measured by use of an Avisoft Accoustic Array system, typically used for investigating animal acoustic communication. It comes with sound wave analysis tool Avisoft-SASLab pro. To ensure the wide range of frequencies three frequencies were measured. 9 kHz, 21 kHz and 50 kHz were recorded with common Vpp of 20V.

Table 4. Measured MFC Frequency Output.

Description kHz Playback	Duration (sec) *This is arbitrary	Loudest Freq (Hz)	Minimum Freq (Hz)	Maximum Freq (Hz)	Bandwidth (Hz)	First Harmonic Loudest Freq (Hz)	First Harmonic Minimum Freq (Hz)
9 kHz	0.0117	9000	8600	9600	900	17900	17900
21 kHz	0.0136	20900	20600	21600	900		
50 kHz	0.0057	50000	49600	50500	800		

From this table it can be seen that all output frequencies from the MFC match the input from the function generator. At lower frequencies a harmonic can be seen to occur. An example of the raw data taken during a sampling can be seen below in figure 21. This was for a test where the wind tunnel was on and a 6.6 kHz actuation was ran at an AoA of 16° (lower) versus and no forcing at an AoA of 0°.

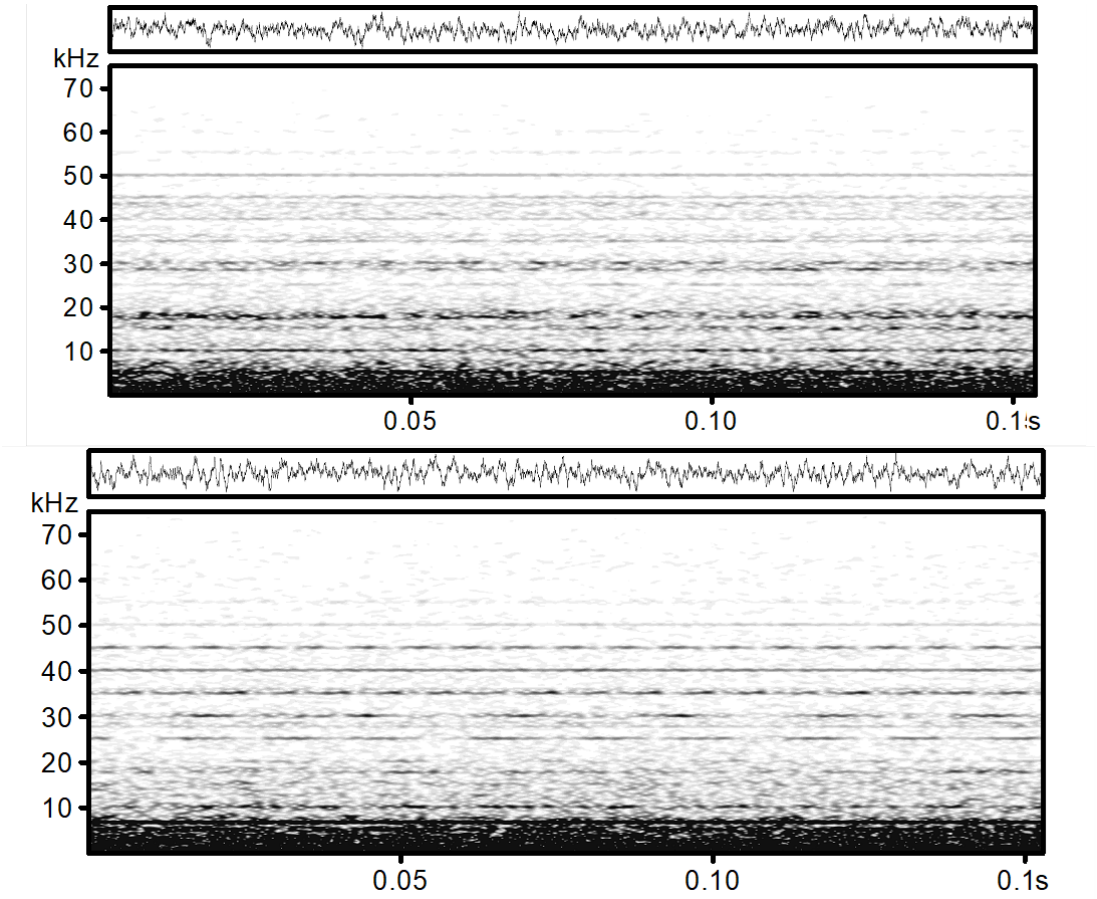

Figure 21. Raw data result for no forcing and at AoA of 0°(Top) and forcing at 6.6 kHz and at AoA of 16° (Bottom).

The airfoil was then tested both in a static configuration as well as pitching. The results associated with both can be found the results section.

3.2. Pitching and Positioning Mechanism

To simulate the pitching demonstrated in the numerical simulations study, which has a reduced frequency of k= 0.04, an apparatus capable of actuating an airfoil with sinusoidal motion was constructed at NDSU. A stepper motor controlled by a driver and Arduino DUE was utilized to pitch the airfoil at the desired angles and frequencies.

The images in Figure 22 depict the pitching test setup and control system, respectively. The stepper motor utilized was a NEMA 34, model 34HS61-6004S1, available from

STEPPERONLINE. The digital stepper motor driver selected was model DM860T and is available from the same vendor. This driver allows for micro stepping and 3200 steps per revolution was selected for testing since it provided sufficient angular accuracy at 0.1125 degrees per step. When powered at full voltage and current this combination provides a holding torque of 13 newton-meters and was sufficient to pitch the airfoil at frequencies up to 30 Hz.

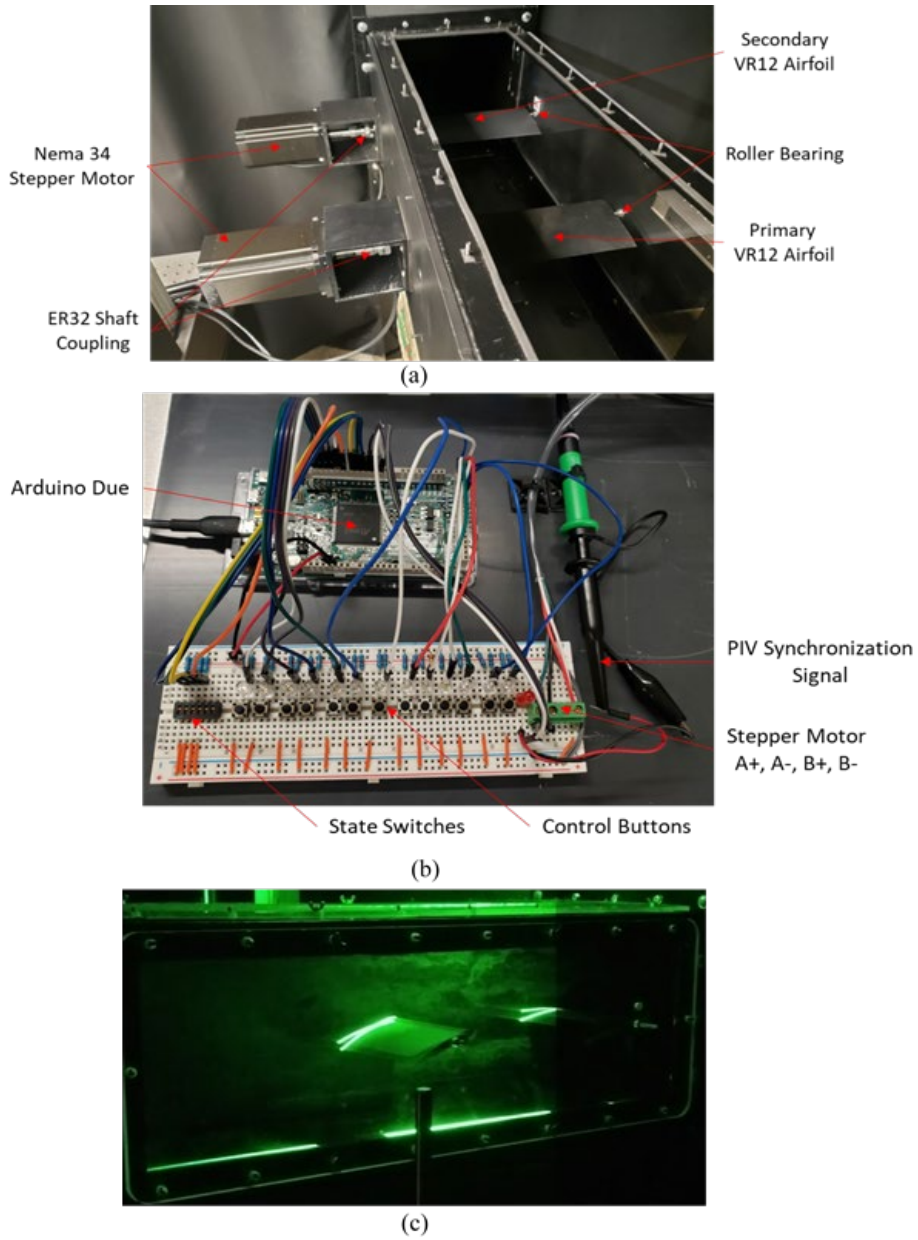

Figure 22. Pitching Test Setup (a), Arduino Control System (b), Tandem Pitching laser-sheet illuminated sample(k=0.04) (c).

As shown in Figure 22 (a) the test setup consists of VR-12 airfoils on keyed shafts. Each airfoil is supported by a roller bearing pressed into the optically clear front viewing panel and attached to a stepper motor with an ER32 shaft coupling. The wind tunnel test section is 12 inches square by 36 inches long. The primary airfoil is positioned at both the vertical and horizontal midline of the test section while the secondary airfoil is located at the horizontal midline, 13 inches upstream of the primary airfoil.

To control the stepper motor driver, a code was written in Arduino IDE and ran with an Arduino Due, as shown in Figure 22 (b). Each driver/stepper motor/airfoil combination required its own Arduino Due to run. The code utilizes the predefined Arduino library "AccelStepper" and allows the operator to set the maximum angle of attack, minimum angle of attack, speed of rotation, acceleration of rotation, as well as various other parameters. Knowing these parameters, the code works by moving the airfoil to the maximum angle of attack, where it outputs a signal, then moves to the minimum angle of attack, and repeats this cycle until stopped. The signal output at the maximum angle of attack acts as a synchronization trigger for the PIV circuitry, allowing data to be taken at any intended angle of attack or set to complete a full interrogation of the wing performance. The code was setup to allow the operator to switch between four different states. Each state enables specific buttons which then allows the operator to perform various actions with the airfoil. The first state allows the operator to set a home position for the stepper motor/airfoil and to run the stepper motor back to this position. In the second state the airfoil can be stepped up or down one step per button press, set home, and run home. The third state toggles the airfoil between user defined angles and the fourth state enables continuous pitching. During the continuous pitching state, the pitching frequency, minimum angle of attack, maximum angle of attack, and the time phase between the primary and secondary airfoils can be manipulated

without stopping the pitching. To ensure no skipping occurs within the stepper motors a “soft-start” and “soft-stop” was implemented in the Arduino code which gradually increased the acceleration until the desired pitching frequency was achieved or decreased the acceleration. To set the frequency, an iterative method was chosen where the airfoil was pitched to determine its frequency based on the PIV synchronization signal. The method was iterative due to the airfoil pitching frequency being dependent on pitching amplitude, pitching speed, and pitching acceleration.

To setup a test, the airfoil shaft was inserted into the ER32 collet, tightened, and the front viewing panel was bolted to the test section. With the airfoil secured in the test section a digital protractor and gauge block were used to set the airfoil to an angle of attack of 0 degrees using state 2 of the Arduino code. Using the third state of the Arduino code and the PIV cameras, static images without the wind tunnel on were taken at all angles of attack required for PIV testing. During testing and data processing the laser sheet illumination on the blade surface provides a means to verify the angle of attack by comparing the position in the image with that from wind-off conditions. Once the correct pitching angles and frequencies were validated, PIV testing was performed. Figure 22 (c) was acquired with the PIV camera with long exposure time to capture the full pitching range motion during a tandem airfoil test.

3.3. PIV Methodology

The following section will discuss the two variations in particle image velocimetry used this this experimental study. These being phase locked PIV and time resolved PIV.

3.3.1. Phase Locked PIV

Experiments are carried out in a NDSU wind tunnel driven by an upstream blower with a variable frequency drive and for the current work a long diffuser was designed and added to the

wind tunnel to achieve speeds up to 60 m/s (Mach ~ 0.17) with turbulence levels ~ 1% and flow uniformity with minimal wall effects in the test section. The design is modular, allowing for removal or insertion of flow conditioning devices such as screens and honeycombs for turbulence conditioning. A section upstream of the contraction was designed to allow for seeding of Di-Ethyl-Hexyl-Sebacate (DEHS) particles from spray nozzles into the test section for Particle Image Velocimetry (PIV). The front and top test section walls are made of clear acrylic to allow for optical access for laser illumination and camera viewing. The rear and bottom walls are modular aluminum panels that allow for mounting of various models in the test section.

Fundamentally, PIV will capture two sequential instances of flow, separated by a few microseconds. Cross-correlation can then be used to determine the displacement of particle ensembles in the flow. Once displacement and time separation are known for each particle ensemble, velocity can be determined. Here velocity fields are captured on the suction side with a global views, leading-edge view, and trailing-edge views to assess the dynamic stall features at several pitching cases. Data captured from the flow field is collected from several points of interest to be compared to computational data. It is important to note that although this is an oscillating system due to airfoil pitching, the point of interest is at specified angles of attack. This requires the PIV to be synchronized ('phase-locked') in order to capture data at the desired point/phase. The control system described in the pitching system design was incorporated to consistently capture data at a desired moment of actuation and is discussed in the subsequent sections.

The fundamental setup of the PIV system can be seen in Figure 23 (a) and photography of the actual setup in Figure 23 (b). The test section of the wind tunnel is illuminated by a double-pulsed Nd:YAG laser (such as Litron Bernoulli PIV or New Wave PIV Lasers) emitting

two laser pulses of 100 mJ at a wavelength of 532 nm with a repetition rate of 15 Hz. The laser beam is then shaped to a laser sheet (thickness <1 mm) by using various prisms, spherical, and cylindrical lenses and is centered in the middle of the wind tunnel. The flow is seeded with atomized Di-Ethyl-Hexyl-Sebacate oil droplets to achieve particles with less than 1μm characteristic diameter. The flow is imaged by three LaVision IMAGER LX 2M cameras with a resolution of 1608 x 1208 and interframe capability of 200 ns set up with their axis perpendicular to the laser sheet for image acquisition as shown in Figure 23. For the desired flow speed, the time between images taken was set to $\Delta t = 10$ μs. One camera captures a global view of the full wing while the others capture the leading-edge and trailing-edge regions. The cameras and the Nd:YAG lasers are connected to a workstation and controlled with a LaVision Programmable Timing Unit (PTU) which controls the timing of the laser illumination and the image acquisition along with the trigger from the stepper motor pitching phases. LaVision DaVis 10 software [4] was used for control of the parameters of the imaging and controlled by the external trigger from the pitching wing. For each test angle, 100 image pairs were collected and the PIV processing was performed using two passes with correlation windows down to 32 x 32 pixels at 75% overlap yielding a spatial resolution of ~ 2 mm (global view) and ~ 1 mm (LE view).

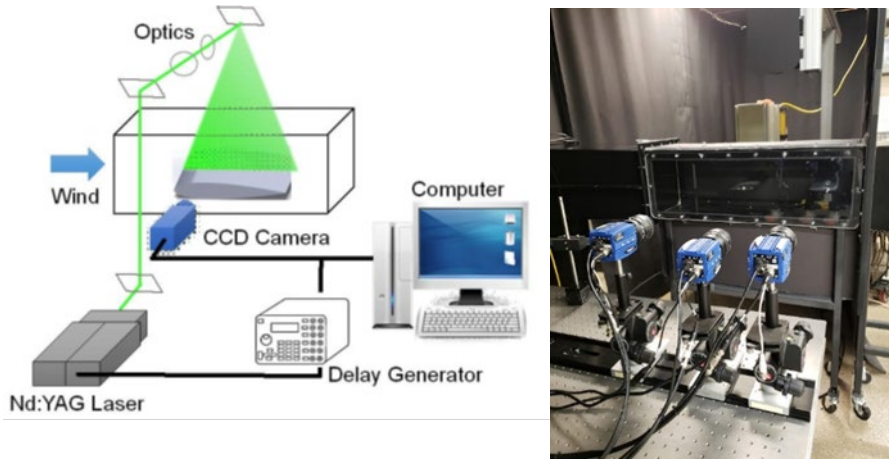

Figure 23. Schematic of Standard PIV system (left) and Setup Photography (right).

3.3.2. Time Resolved PIV

Time resolved PIV is an extension of the regular PIV or as previously defined phase locked PIV. It makes use of high-speed cameras and laser systems, to take high volumes of data in short periods of time. In regular PIV you are able to use cross correlation to assess the displacement of the particles between two frames. Time resolved PIV allows for the tracking of the particle through multiple frames. Thereby adding a time component to the data. With this information, measurements like acceleration are also possible. The laser system is a Photonics DM200-532DH Nd-YAG laser capable of outputting 20 mJ per pulse with a max pulse rate of 30 kHz. Two Photron FASTCAM NOVA S12 cameras (capable of 12.8 kHz rate at full resolution of 1024 x 1024 pix and 40 kHz at 640 x 480 pix) were used to capture the data. One camera was placed toward the front of the airfoil so LE data could be taken, with the potential to see the shear layer form. A second camera capturing the suction side of the air foil was used, giving a global detail. The laser configuration and camera configuration can be seen below in figure 24.

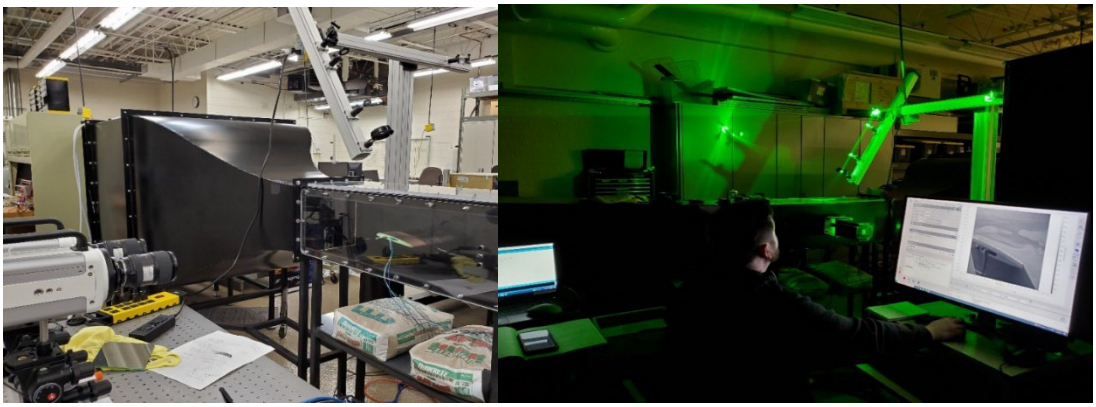

Figure 24. PIV test setup with angled laser optics.

4. RESULTS AND DISCUSSION

The following section is broken out into four main categories; statically deformed airfoils, active morphing, microcavity, and LEAR. The results of the experiments described in the methodology section as well as pertinent discussion are presented.

4.1. Statically Deformed

Following the earlier parameter design section and 3D URANS simulations [24, 31] the performance with angle of attack based on coefficient of lift, drag, and lift over drag were the starting point for the experimental design. The upper and lower limits of the pitching domain were increased to ensure dynamic stall was seen through all configurations. Further testing was performed from a 22° to -10° and it was found that dynamic stall initiates from 14 to 16° for all airfoils, with full stall occurring between 18° to 22°.

The results are presented as phase-averaged velocity field plots (magnitude contour, vectors, and streamlines) for representative deflection cases and the baseline and pitching angles. It is noted that in the global view presented here, the LE location is hidden due to obstruction of the view from the wing and thus the actual flow around the LE is not visible. The below velocity fields have been non dimensionalized with respect to their average free stream velocity:

$$V^* = \frac{V}{V_\infty} \tag{4}$$

Results are presented for three angles of attack: the maximum (22º) (Fig. 25) and intermediate pitching down 16º (Fig. 26) and 10º (Fig. 27). In these figures the actual airfoil geometries are shown. These selections are corresponding to pitching down motion and reflect most prominently flow separation and stall characteristics. The main indicators of performance are separation regions and wake properties as they directly relate to lift and drag. Details such as starting point, size, extend, and direction of these regions can be measured from the velocity

field. From the velocity field, prominent separation regions are revealed by the lower velocity magnitude, flow reversal, and recirculation regions.

In line with this reasoning, it can be seen that the best performing static airfoil is the 6º deflected LE, consistent with previous experimental [29, 31, 38] and computational [24] findings from literature. The deflection effect is less noticeable at the full stall angle α (22°, max), such as those seen in Fig. 25, although the patterns are different for each case, based on the showing size and shape of each stall bubble and when compared with the baseline. The benefits of LE deflection are quite revealing in the 16º pitching down motion (Fig. 26) showing that this LE configuration is the only one without a recirculation and with a smaller wake; its comparison with baseline using streamlines is shown in Fig. 28. The leading and trailing edge deflected airfoil is performing similarly at the lower α's. The worst performing airfoil would be the one with only trailing-edge deflection.

Distinguishable difference can also be detected in terms of performance associated with the four variations for the 10º pitching down (Fig. 27) Both the leading-edge deflection and the combined leading and trailing edge deflections perform similarly. As they both have the have similar beginning of the wake and their size. It can be noted that the leading-edge deflected case appears to have a lower overall velocity within its stall wake. The baseline VR-12 and the trailing-edge deflected cases both performed similarly, there appears to be a slight performance enhancement associated with the trailing-edge deflection with the stall wake being smaller and more attached.

As the airfoils sweeps back up little effect was perceived between the four different airfoils that were fabricated. This was to be expected with most dynamic stall conditions

occurring in the downward sweep of the airfoil [43-45]. Data for those other different angles have been reported in the work by Refling et al. [31].

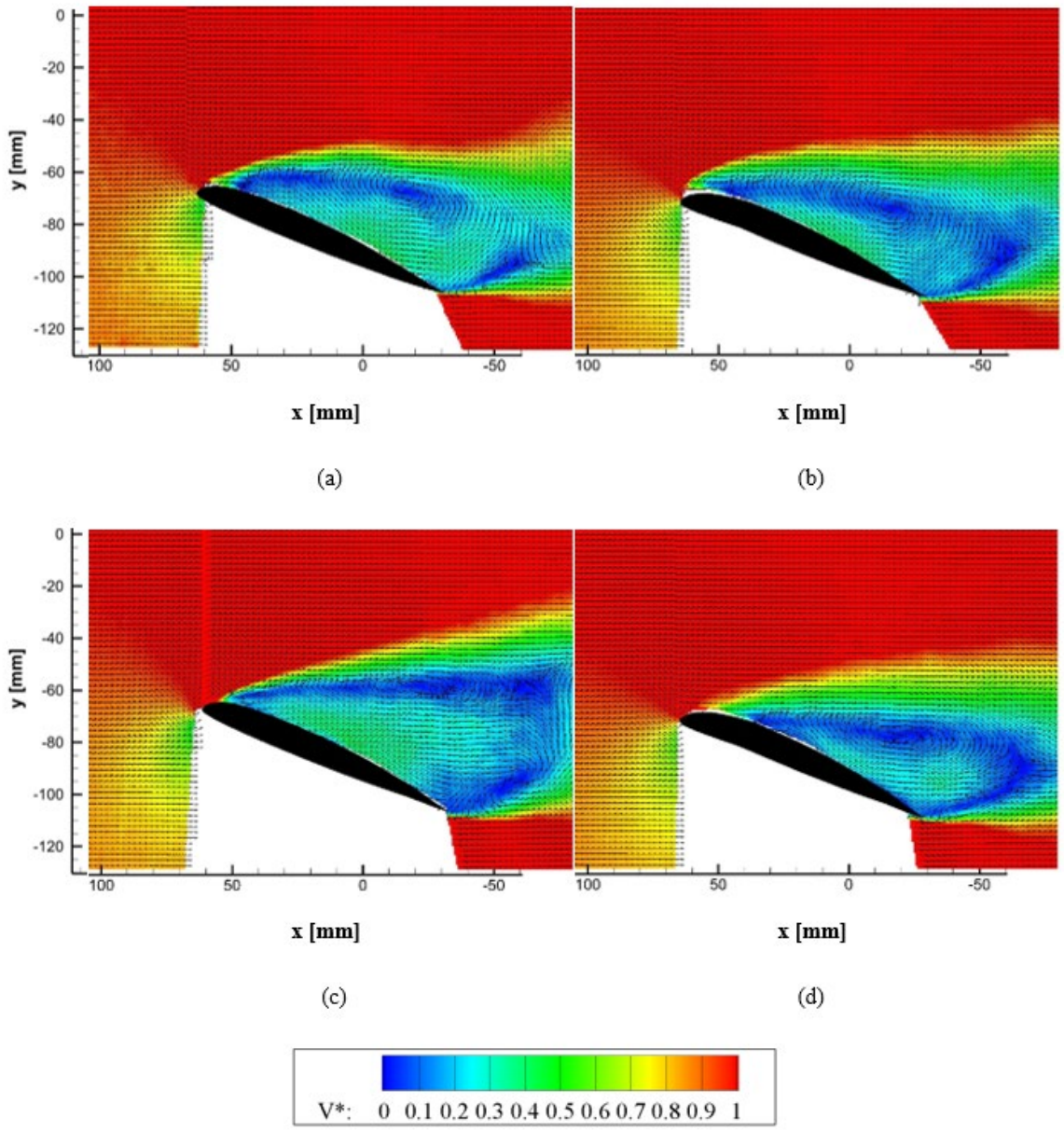

Figure 25. Velocity fields for 22° max-AoA of the pitching motion for the deflected airfoil variations: (a) Baseline, (b) LE deflected, (c) TE deflected, (d) LE&TE deflected.

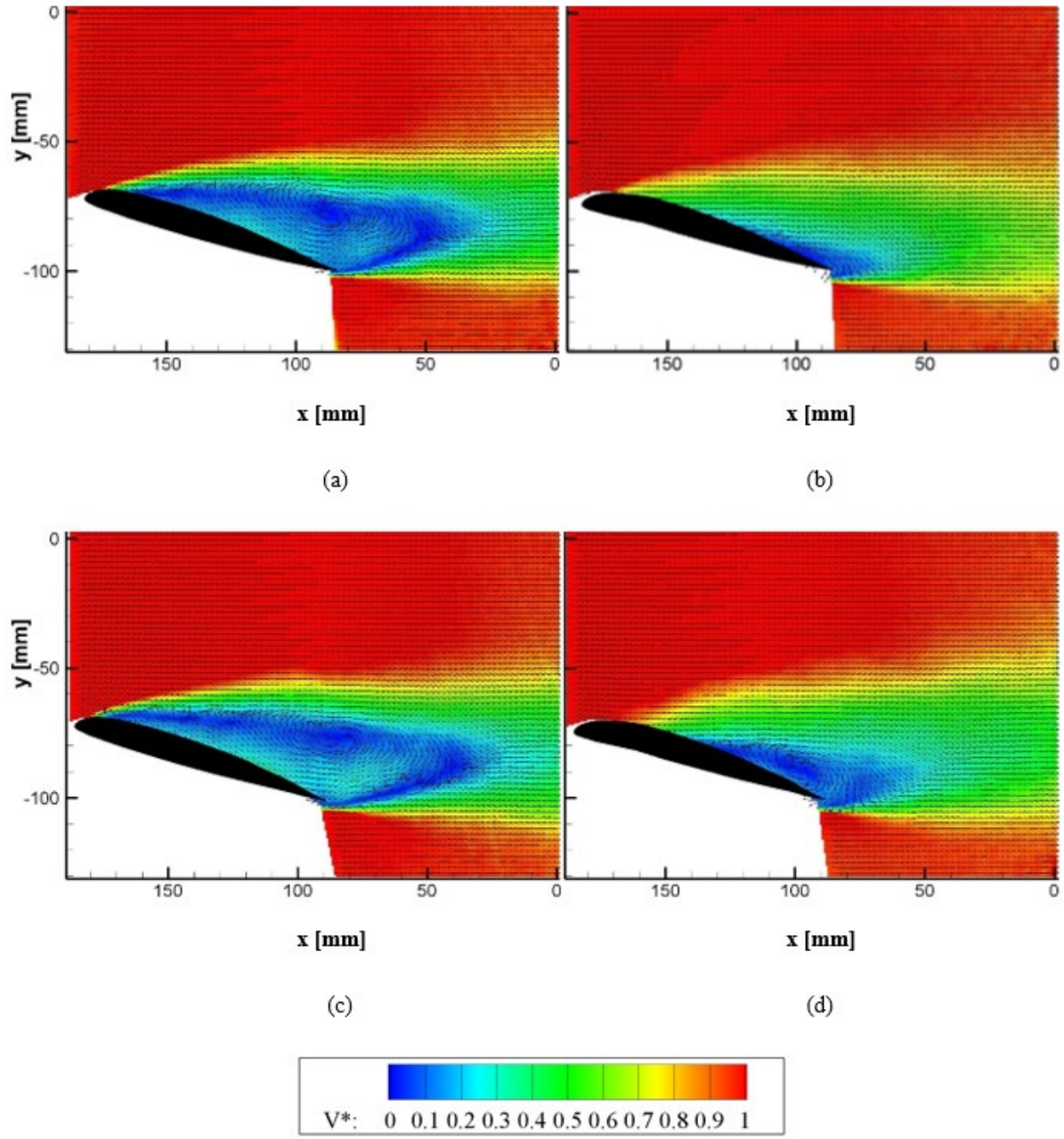

Figure 26. Velocity Fields for 16° AoA pitching down (↓) for deflected airfoil variations: (a) Baseline, (b) LE deflected, (c) TE deflected, (d) LE&TE deflected.

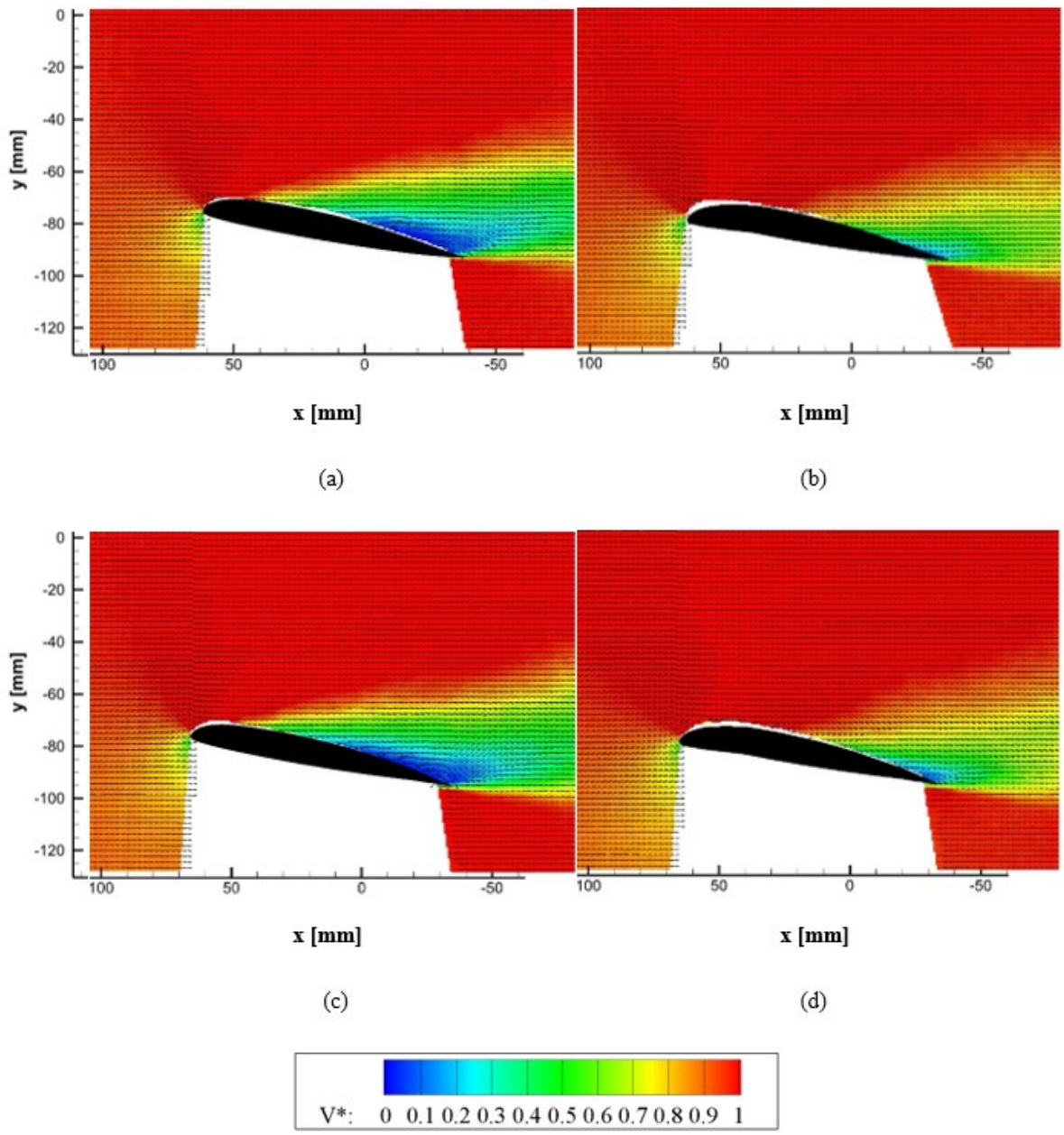

Figure 27. Velocity Fields for 10° AoA pitching down (↓) for deflected airfoil variations: (a) Baseline, (b) LE deflected, (c) TE deflected, (d) LE&TE deflected.

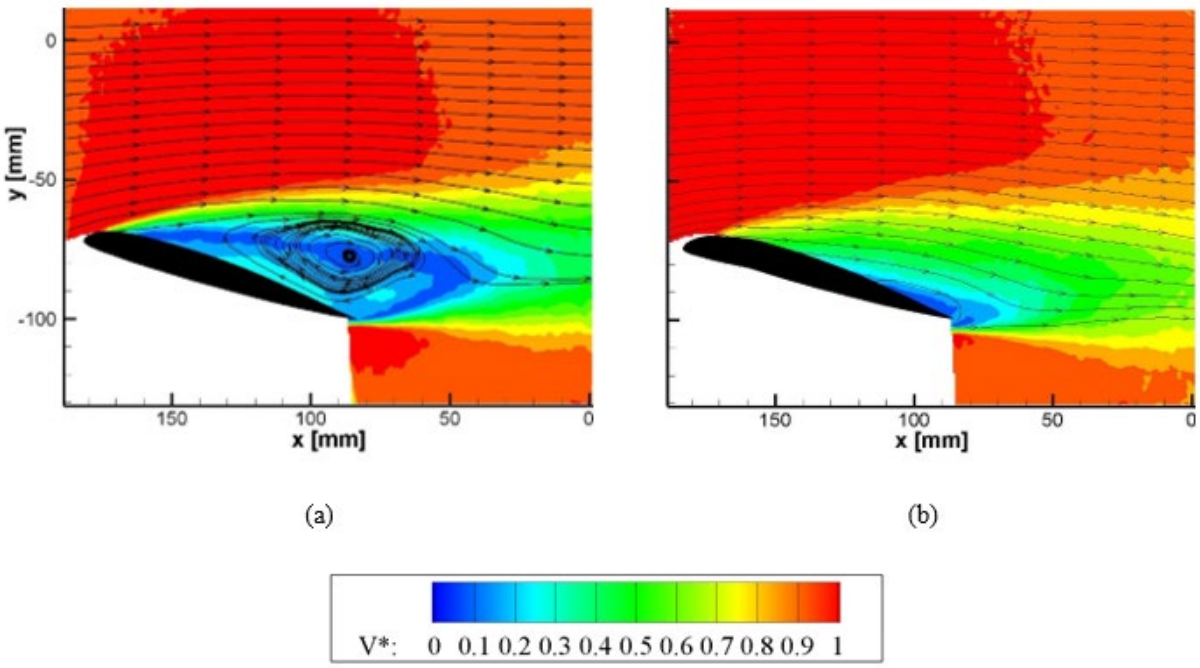

Figure 28. Streamline velocity fields streamlines for 16° AoA pitching down (↓) for deflected airfoil variations showing Dynamic-Stall control: (a) Baseline, (b) LE deflected.

4.2. Tandem Pitching

Following the proof-of-concept for the design functionality with the pitching and tandem configurations and assessing the basic performance of the deflected airfoils, the main relevant results in the tandem design are presented in this section. This campaign investigated both in-phase pitching where both the primary and secondary airfoils reached the maximum and minimum angles of attack at the same time and out-of-phase where the primary airfoil read the maximum angle of attack as the secondary airfoil reached its minimum angle of attack [55].

From the many relative phases incurred during pithing of both airfoils in tandem configuration, here we focus on the two most extreme, in-phase and out-of-phase; studying other interactions from other phase combinations are expected to fall in between these two cases although the flow patterns can be unpredictable and chaotic; their study is out of the scope of this current investigation. Here, few pertinent performance phases of the two cases are presented

using the phase-averaged PIV described above. It is noted that analysis of instantaneous patterns and their variability within and between cycles could be performed using reduced order models to establish the phase-coherence from the phase-locked data [55] or more readily with high-speed PIV systems that can track time resolved motion.

The discussion here pertains to the two-relative phase tandem test cases (in and out of phase) performed from the four statically deformed airfoils to highlight the phase flow distinctions and highlight the benefits from having LE deflection in certain conditions. The relevant cases for in-phase and out-of-phase are shown in Figures 30-31 and Figures 32-33, respectively, and for the downstream airfoil at the maximum phase (22°) and at the 16° phase pitching down. Other phases have been reported by the authors in Refling et al. [55]. Since most effects are expected to be in the downstream wing, the PIV region of interest was only from the TE of the front wing to the TE of the back wing.

For illustrative purposes of the phases between the two wings, the single airfoil data for the upstream wing is used in the plots. It is worth noting here that the front wing is the baseline (a limitation of the current set up) but still defines the main flow effects on the deflected back wing for the current purposes. We also note that the broad effect of having an airfoil in front of another is threefold (front wake flow, actual α, and blockage) that is affected by their distancing. While the velocity field generated from the pitching wing ahead is associated with the much more chaotic separation and wake flow than a free stream flow, the velocity magnitude is much lower and the effective Reynolds number and angle of attack diminished. At the distancing studied, the effect of blockage is similar in all cases at the higher back-wing α cases and much less pronounced at lower α's, as expected. The data illustrate how these factors influence the in-phase scenarios preventing stall even with baseline at the maximum phase (Fig. 30 a), but still

more so with LE deflection (Fig. 30 b), with the out-of-phase scenario showing full dynamic stall (Fig. 32) regardless the wing deflection. The TE and LE/TE deflections show less benefits as shown in Fig. 32 (c, d) and are omitted from the remaining cases (fully reported in ref. [55]). Graphs comparing the difference between the angles of attack of the leading airfoil and the can be seen below. Figure 29a shows how the angles of attack for the upstream airfoil and the downstream airfoil are the same during pitching. Instead, the out-of-phase pitching of the two airfoils can be seen to be offset by one half of the period in Figure 29b.

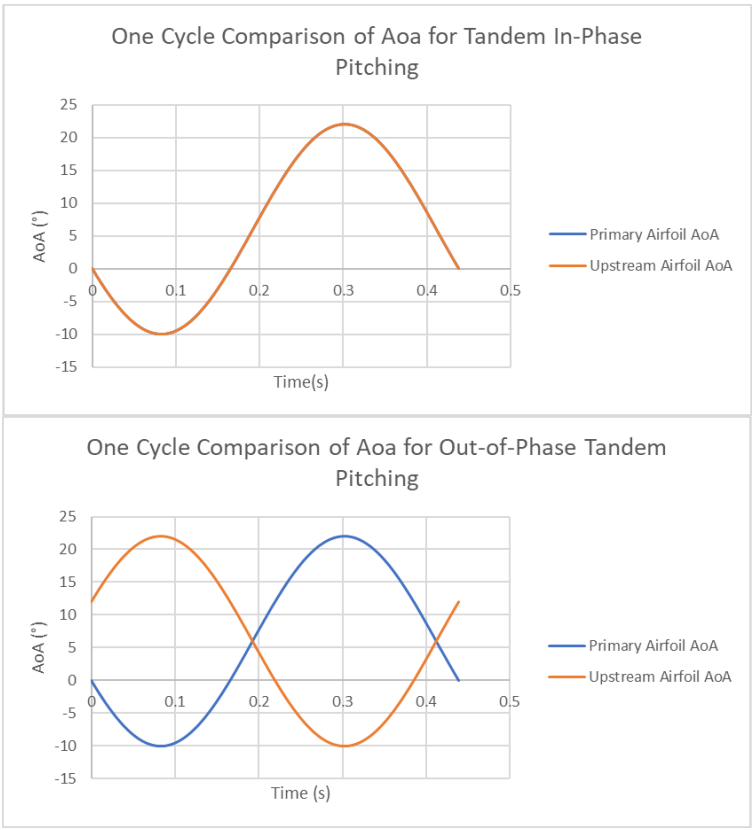

Figure 29. Comparison of AoA for Upstream and Downstream Airfoils for (a) In-phase pitching and (b) out of phase pitching.

The effect of the various deflections during tandem is shown for the in-phase case in Figure 29 during the maximum phase of the downstream airfoil (22°) with the LE deflected airfoil appearing as having the best performance. As it can be clearly seen, the stall wake is the

smallest with least amount of recirculation for this LE deflection case (Fig. 30 b). Both, the leading and trailing edge deflected combination and the trailing edge deflected airfoil performed similarly to each other with what appears to be attached flow up until about the 25% chord length (Fig. 30 c and d). At which point the flow separates quickly, follows an upward motion clearly marked by the 70% of the maximum velocity ('yellow' velocity contour region) and the upward direction of the vectors, and form larger wakes with downward motions and recirculation (blue contoured regions). These motions are opposite to the baseline and LE deflected airfoil flows. It is worth noting that when compared to the single airfoil the overall performance is improved for the 'tandem-effect' reasons aforementioned.

Note that the phase-averaged flow between the two wings is repeatable in all these cases, instilling assurance in that comparisons between the four cases have matched upstream conditions. The other phase shown for the in-phase arrangement is the 16° pitching down (Fig. 32) and reveals a different pattern near the LE deflected airfoil which is delaying the onset of low speed and separation point along the suction surface. In the case of the out-of-phase pitching more unsteady interactions are observed for the 22° case shown in Figure 31 where the flow can be seen having a large separation/recirculation across the suction side of the airfoil, reflecting that dynamic stall is occurring (the region just after the first wing TE is noisy due to poorer PIV illumination from one of the lasers in that section during that particular test). Indeed, in the out-of-phase scenario the upstream wake velocity is much higher and the wake thinner than in the in-phase case and thus produce conditions leading to dynamic stall like in the single airfoil cases. For lower phases, such as the 16° pitching down (Fig. 33), the LE deflection reveals again an improvement in the separation control.

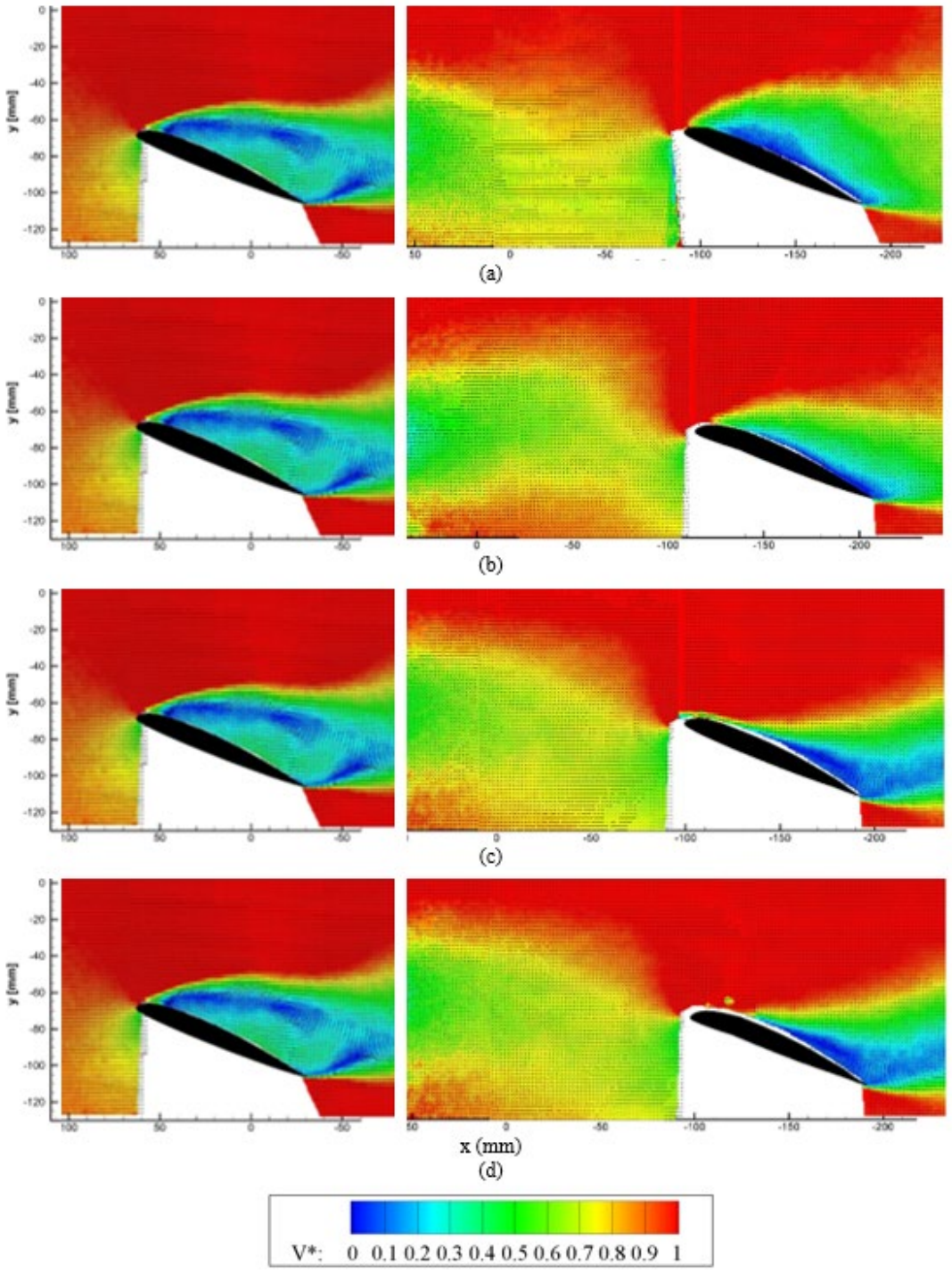

Figure 30. Velocity fields for linear tandem airfoils pitching in-phase at 22° max-AoA : baseline (a), LE deflected (b), TE deflected (c), and LE/TE deflected (d).

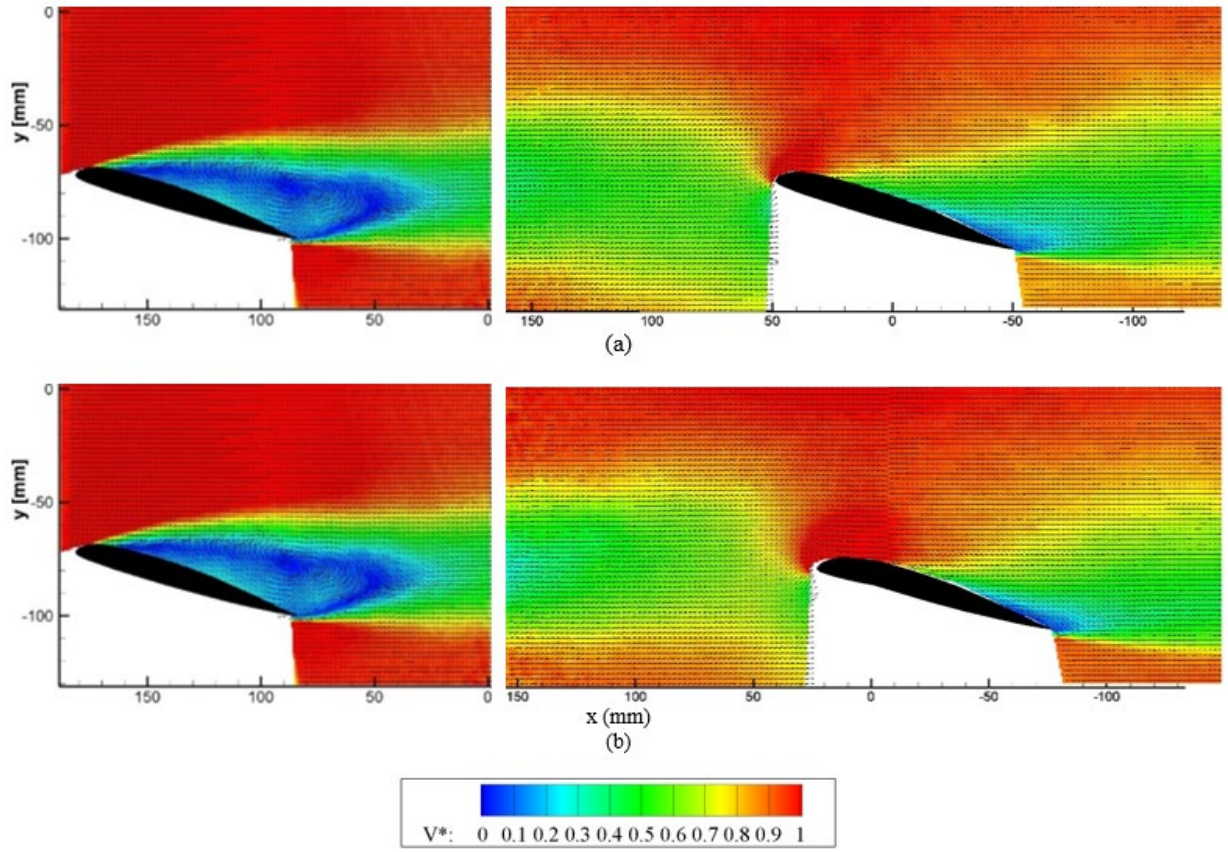

Figure 31. Velocity fields for linear tandem airfoil pitching in-phase at 16° AoA (↓): baseline (a), LE deflected (b).

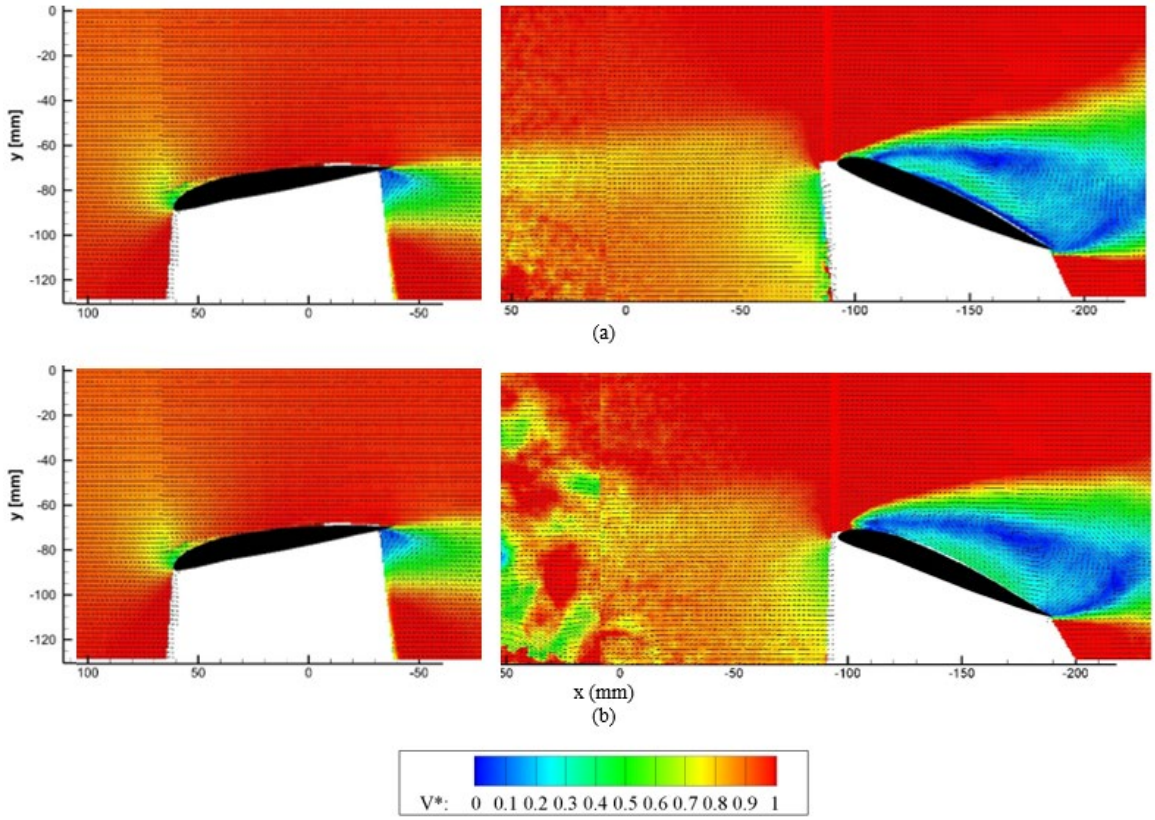

Figure 32. Velocity fields for linear tandem airfoil pitching out-of-phase -10° (front wing) and 22° max (back wing) AoA: baseline (a), LE deflected (b).

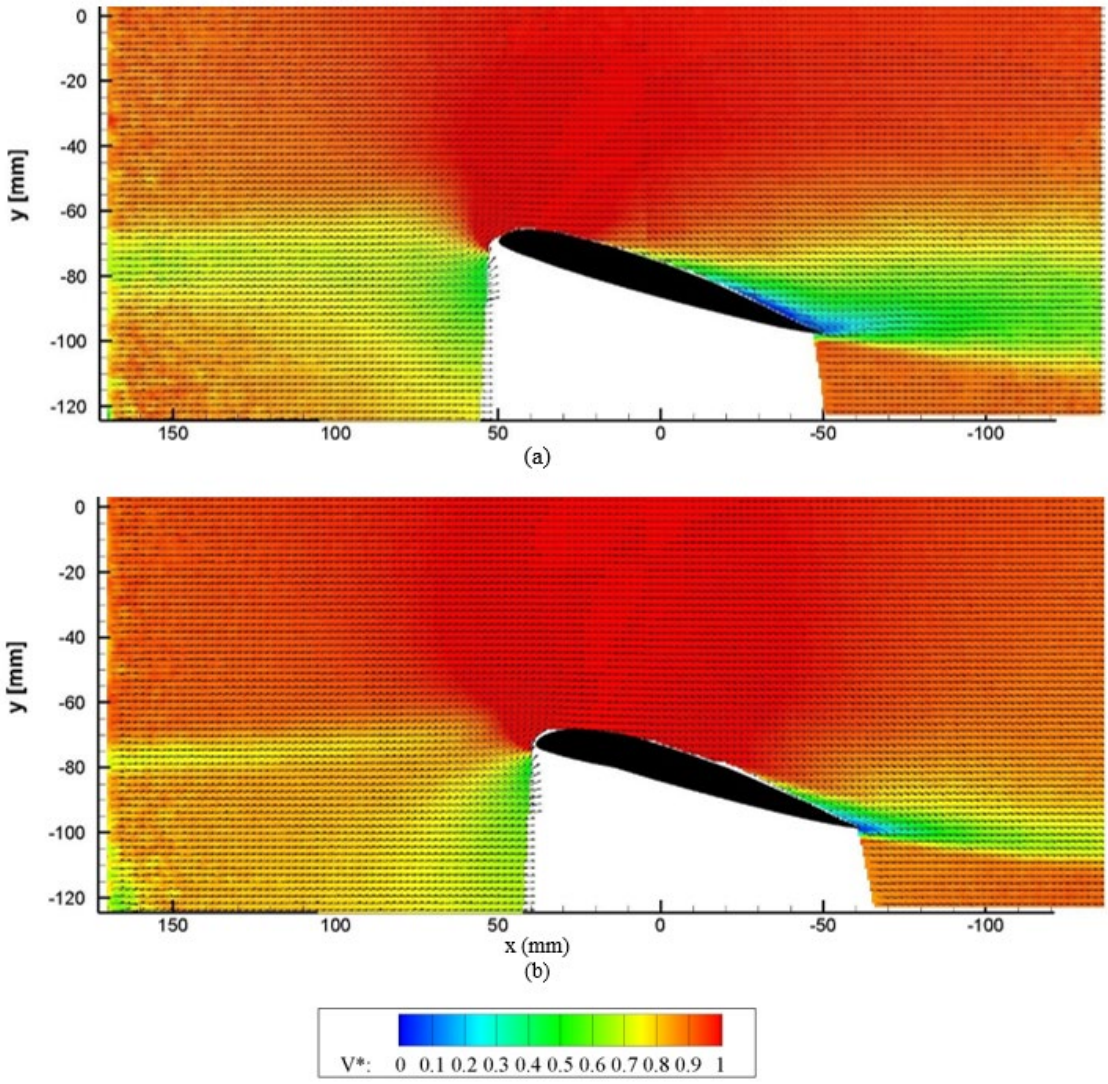

Figure 33. Velocity fields for linear tandem airfoil pitching out-of-phase -4° AoA (↑) (front wing) and 16° AoA (↓) (back wing) AoA: baseline (a), LE deflected (b).

4.3. Morphing Airfoil

Active morphing testing was completed for a velocity of 25 m/s and pitching frequency of 2.28 Hz. The range tested was from -10 to 18 degrees. Instead of the previously planned testing at 22°. This was done due to the extreme dynamic stall that was seen for all test cases whether morphing was engaged or not. As such a reduction down to 18 seemed to be the most logical as this showed a full dynamic stall for the baseline VR-12 within the wind tunnel. Testing

then proceeded using the baseline VR-12 with no morphing or deformation, the morphing airfoil with no control operating and finally, active morphing airfoil. The reason for this being the approximate 2° of deformation that the morphing airfoil had on the leading-edge during glue up as indicated in the methods section.

The results of these three test objects can be seen in the figures 34 thru 36. The first representing the raw flow visualization for both the leading and global views, the second group is of the processed instantaneous velocity fields.

It can be seen from these raw images that the baseline VR-12 is undergoing deep dynamic stall, while the 2° drooped LE shows a light dynamic stall condition. Where a light DSV forms and traverses down the suction surface of the airfoil, eventually combining with the TEV to form a region of flow separation. When compared to the active morphing airfoil there is no DSV to be seen instead a light TEV seems to form but no true separation wake forms. This can be further seen in the PIV results. Again, the baseline model incurs a large DSV that merges with the TEV and develops into a full stall wake. The light stall persists for the drooped LE.

From the raw data collected from the teensy development board. The IMU has moments of incorrect measurement of AoA. In the sense that it tends to overestimate the angle, due to the offset put into the code, this could be in part due to not using a high enough sample frequency. This is however handled by the code as any measurement greater than the minimum and maximum AoA results in the maximum PWM value being used to provide power to the MFC's. This testing was replicated a total of eight times. For each of the tests the system performs as shown, providing a high confidence in the methods ability to mitigate stall.

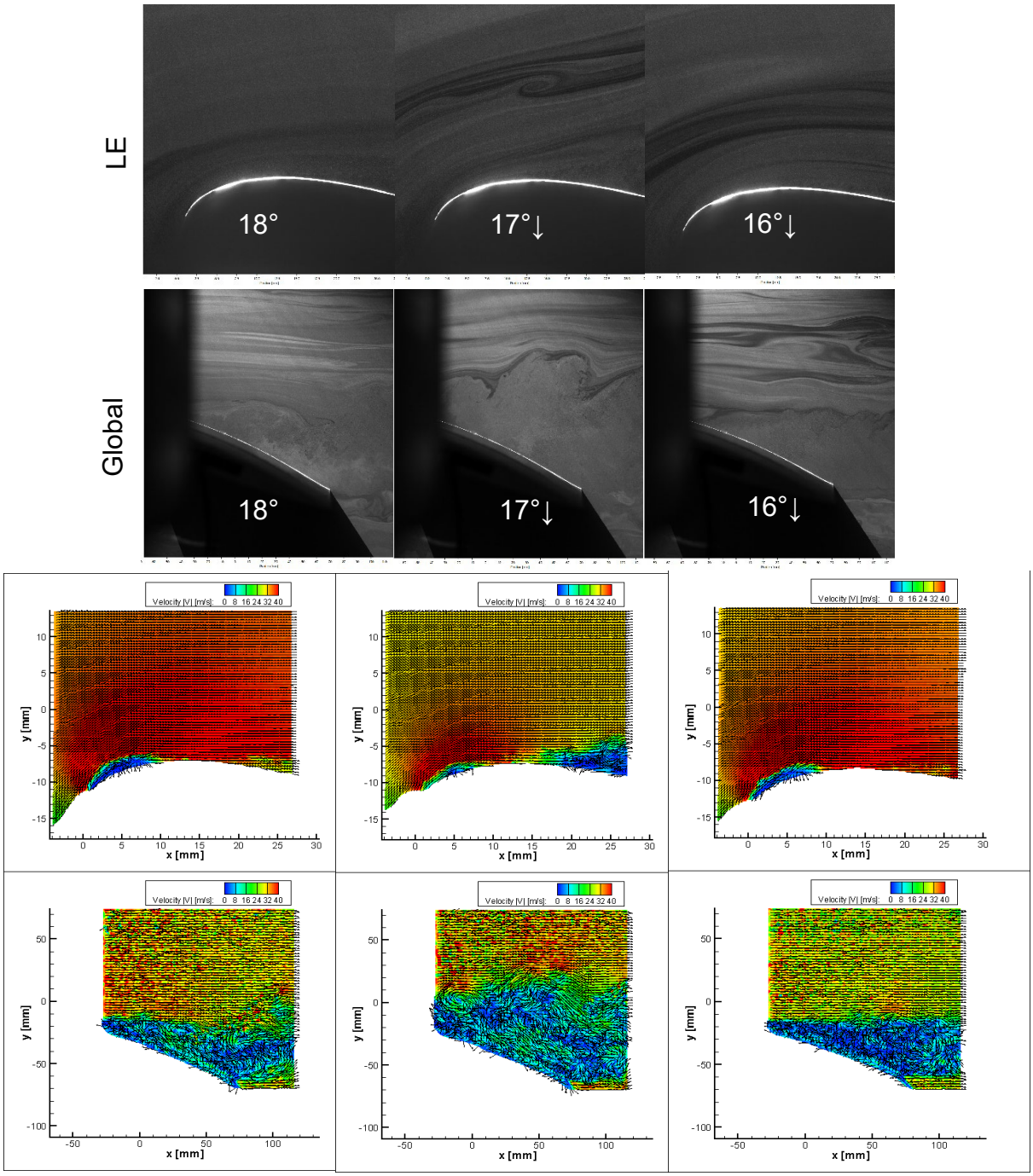

Figure 34. Flow visualization images and corresponding PIV results for baseline VR-12 airfoil for various AoA during pitching cycle.

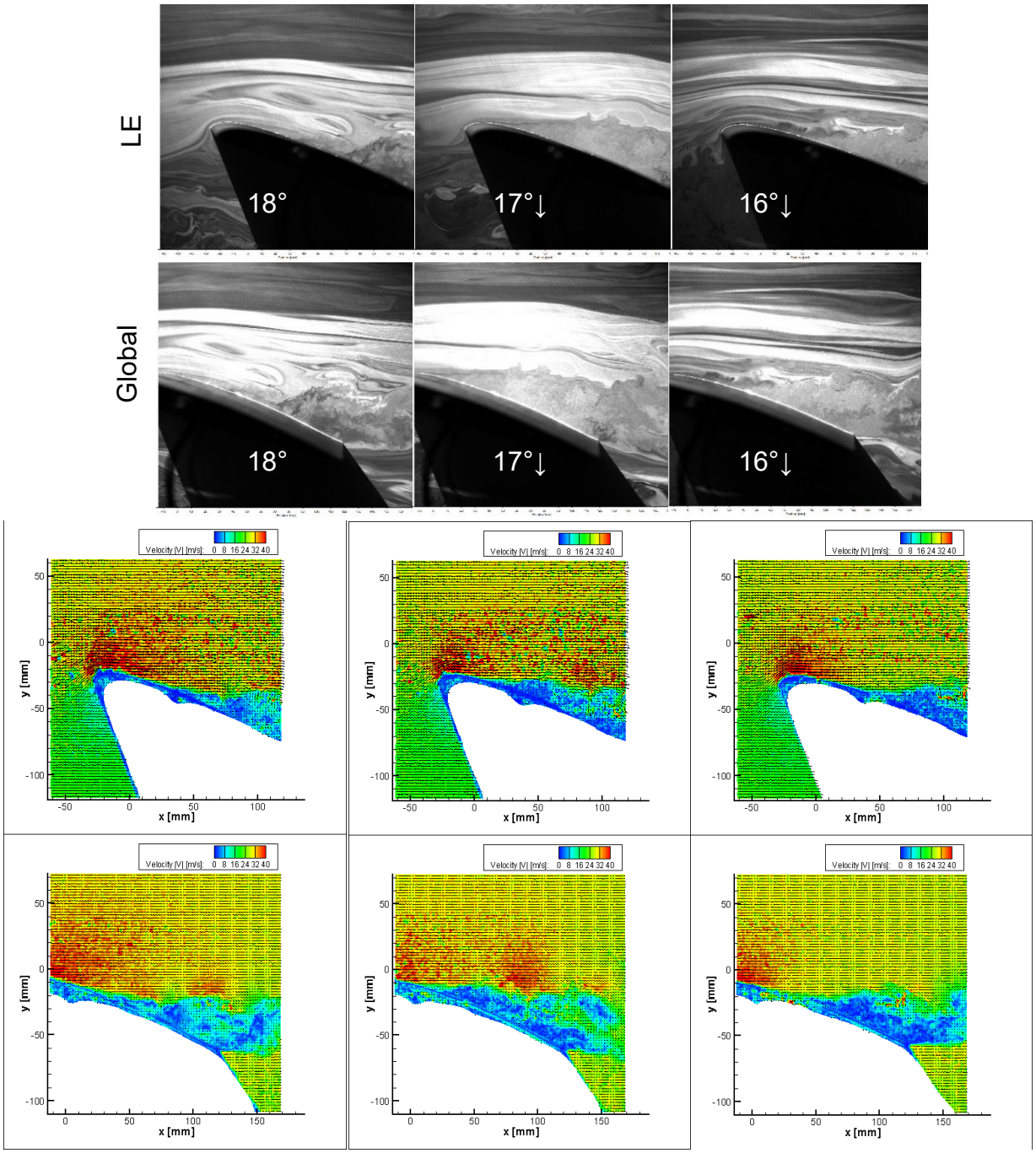

Figure 35. Flow visualization images and corresponding PIV results for a VR-12 airfoil with 2° drooped LE for various AoA during pitching cycle.

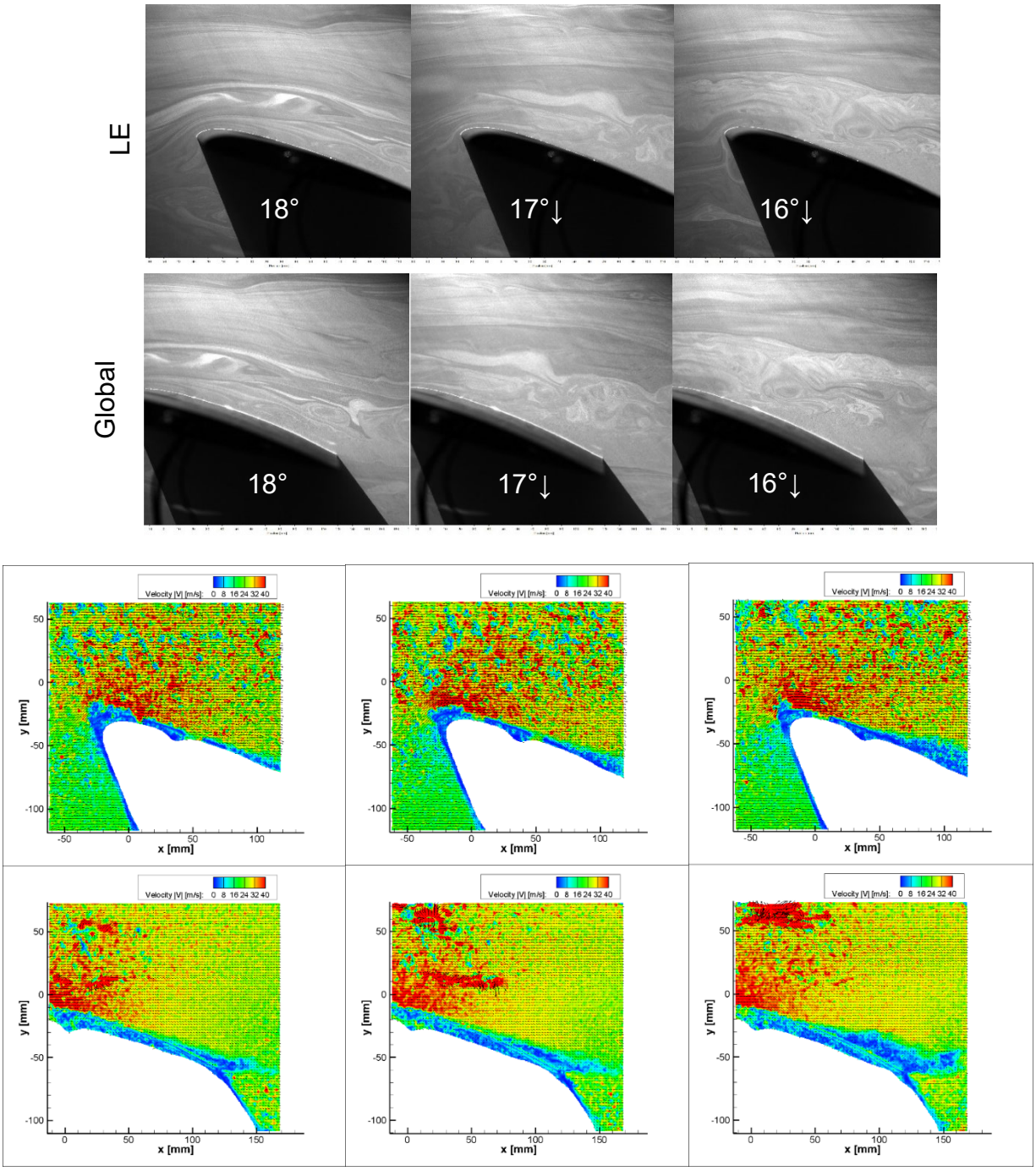

Figure 36. Flow visualization images and corresponding PIV results for a VR-12 airfoil with active morphing LE and TE for various AoA during pitching cycle.

4.4. Micro-Cavity

4.4.1. 127 mm Chord Preliminary Results

In this section, PIV results for two Reynolds numbers (300K and 500K) are reported. Flow visualization was performed first to qualitatively explore the experimental ranges (frequencies, angles of attack, Re) needed to detect dynamic stall and microcavity effectiveness. Figure 37 shows some relevant samples for the Re = 300K (k=0.2) for the baseline and the wing with the micro-cavity. This case readily reveals qualitatively the dynamic stall of the baseline compared to the micro-cavity cases. The baseline is showing large separation at maximum angle followed by trailing edge vortex as the pitching goes down. These are not observed in the microcavity case, indicating a separation control.

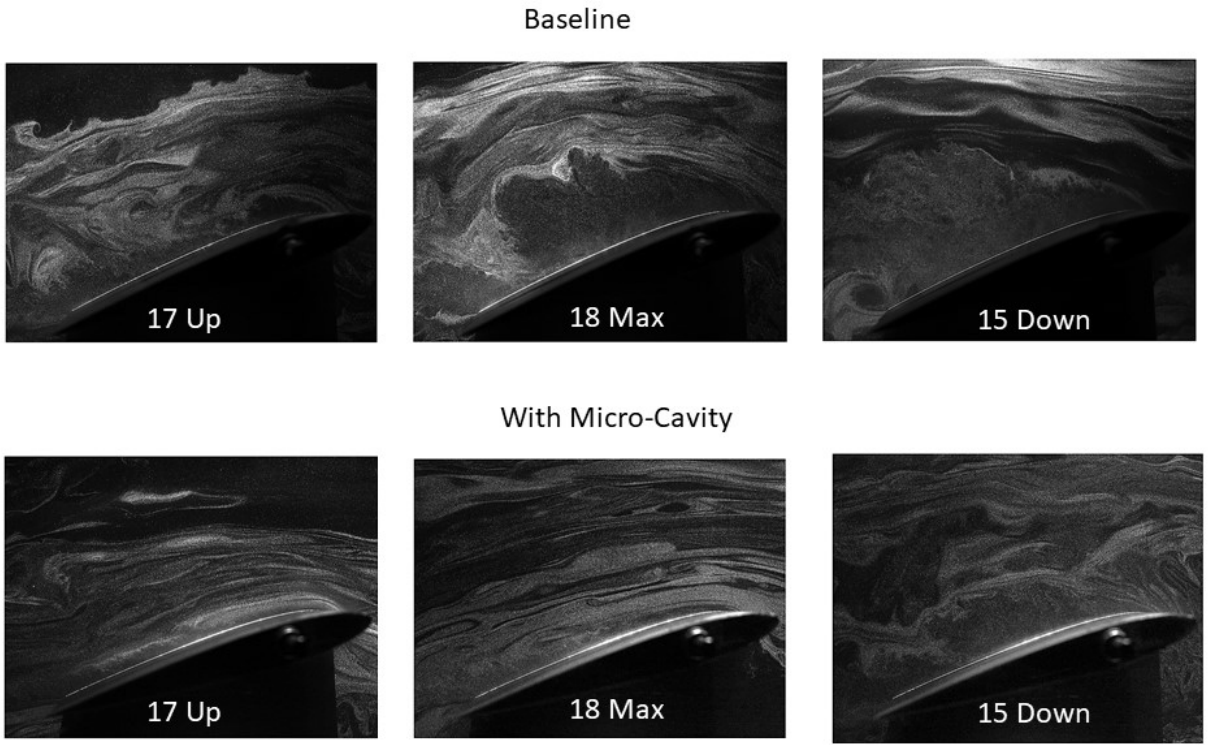

Figure 37. Sample flow visualizations at Re = 300K, k = 0.2 for Baseline and micro-cavity wings.

During this exploratory phase of the investigation conditions adjustments for minimum and maximum angle of attack around the desired values close to the CFD values (~ 4º to 18º) were tested. The features leading to dynamic stall and its suppression happen during the change from up phase to down phase, thus, small increments in these locations are needed and included typically 1-2 degrees. This means that the wing should be robustly locked. At the lower speed of 35 m/s the PIV images revealed stationary 'phase-locked' wings at a given phase with very little jittering. At the higher speed (60 m/s) the images however showed some trailing edge jittering that could have an effect in the dynamic stall. The next generation of wing design incorporates internal struts to stiffen the wing structure while keeping the weigh reasonable for proper pitching controllability. Note that the global view does not capture the leading edge due to the blockage of the view from the wing itself so a second camera was added to gather details of the leading-edge flow. It is also noted that the instantaneous shots reveal more unsteadiness than these averages during the dynamic stall phases (maximum and pitching down).

The lower Re number (300K) cases are presented in Figure 38 and 39 for some selected phases. The angle ranges for the microcavity wing (Fig. 38) and baseline (Fig. 39) are similar and the few pitching down and up phases shown reveal an improvement on separation by the use of the microcavity. For the higher speed cases (Figures 40-42), the baseline is shown alongside two cases of the wing with microcavity. In this averaged velocity field, the baseline shows much larger separation region during the pitching down phases (Fig. 40) than the microcavity case with similar range (Fig. 41). On the other hand, increasing the range in the microcavity case produce a different flow pattern leading to larger separation than the one at reduced range (Figure 42).

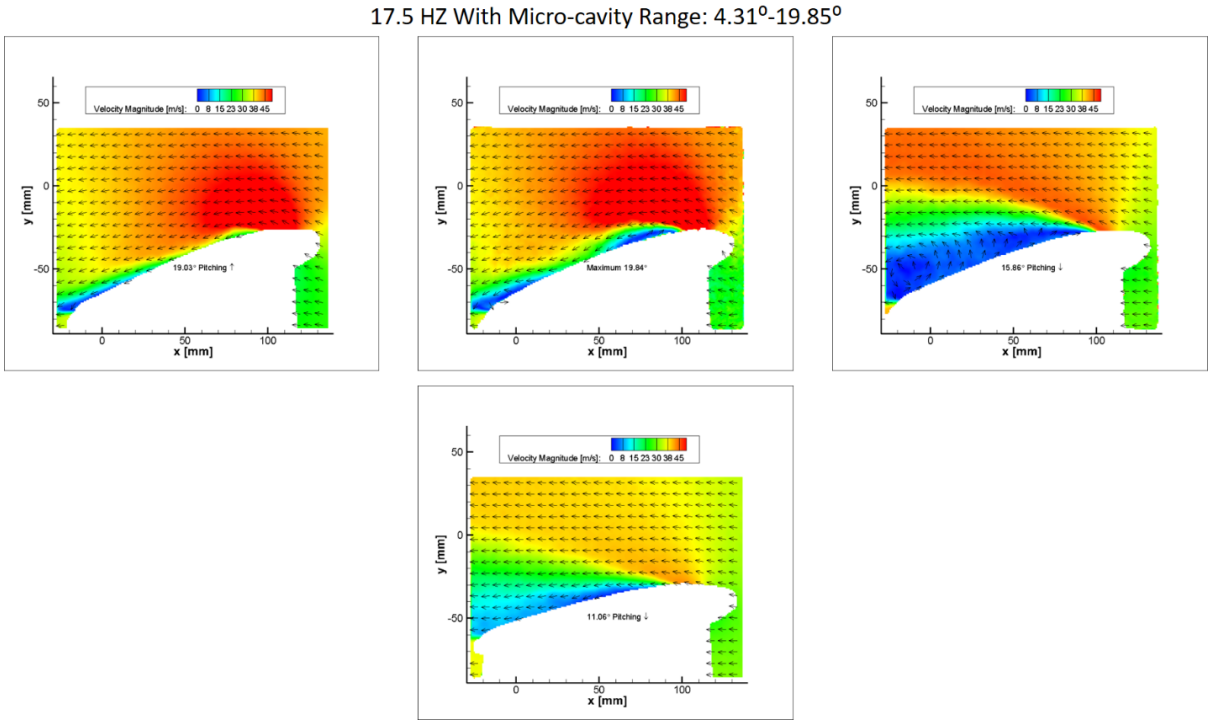

Figure 38. 300k Re, 17.5 Hz Pitching Frequency with microcavity added to LE for 19.03º pitching up (top left), 19.84º (top center), 15.86º pitching down (top right), and 11.06º pitching down (top right).

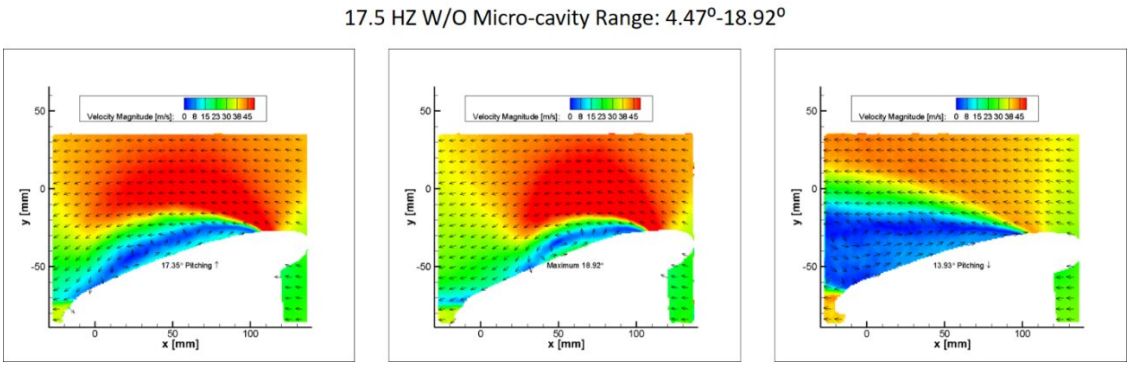

Figure 39. 300k Re, 17.5 Hz Pitching Frequency without microcavity added to LE for 17.35º pitching up (left), 18.92º (center), and 13.93º pitching down (right).

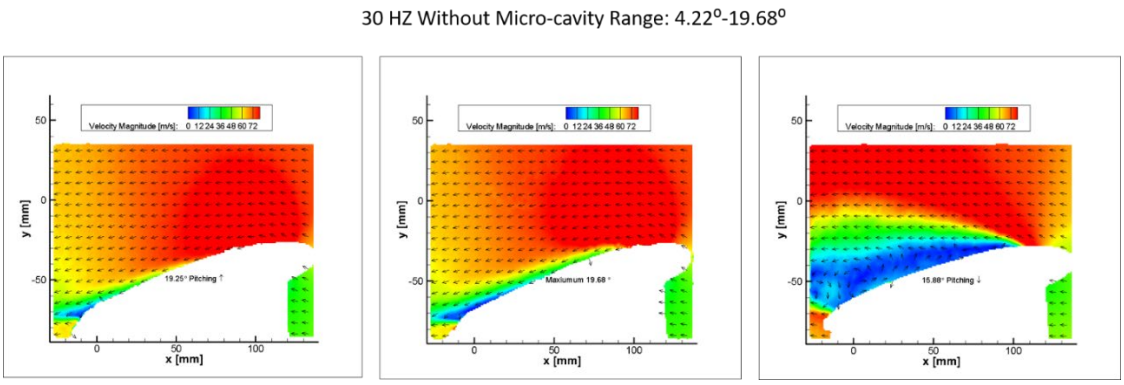

Figure 40. 500k Re, 30Hz Pitching Frequency without microcavity added to LE for 19.25º pitching up (left), 19.68º (center), and 15.88º pitching down (right).

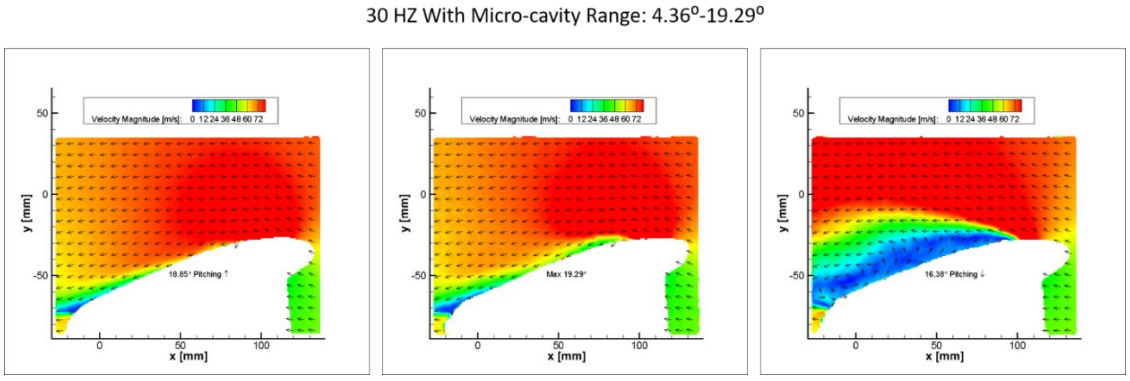

Figure 41. 500k Re, 30Hz Pitching Frequency with microcavity added to LE for 18.85º pitching up (left), 19.29º (center), and 16.38º pitching down (right).

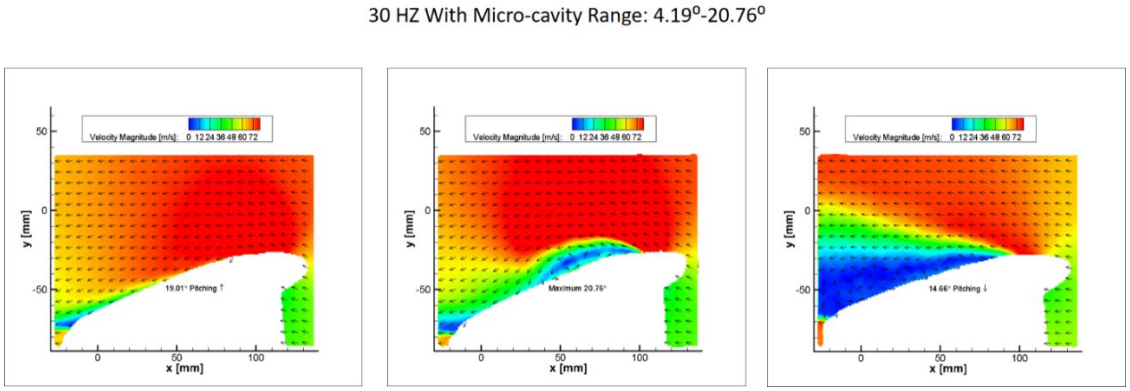

Figure 42. 500k Re, 30Hz Pitching Frequency with microcavity added to LE for 19.01º pitching up (left), 20.76º (center), and 14.66º pitching down (right).

4.4.2. Revised 127 mm Chord

After modification to the cavity through different manufacturing processes as well as the addition of ribs to the model to reduce internal vibrations. Testing was performed with larger stepper motors and more robust pitching control algorithms. PIV results are reported below. Flow visualization was performed first to qualitatively explore the experimental ranges (frequencies, angles of attack, Re) needed to detect dynamic stall and microcavity effectiveness.

During this exploratory phase of the investigation conditions adjustments for minimum and maximum angle of attack around the desired values close to the CFD values (~ 4º to 18º) were tested. The features leading to dynamic stall and its suppression happen during the change from up phase to down phase, thus, small increments in these locations are needed and included typically 1-2 degrees. This means that the wing should be robustly locked.

Data acquired and processed during this reporting period is presented in the Figures below. Note that the LE is not in the view processed this reporting period and the actual location in the data is shown as in Figure 43 for the global view cases.

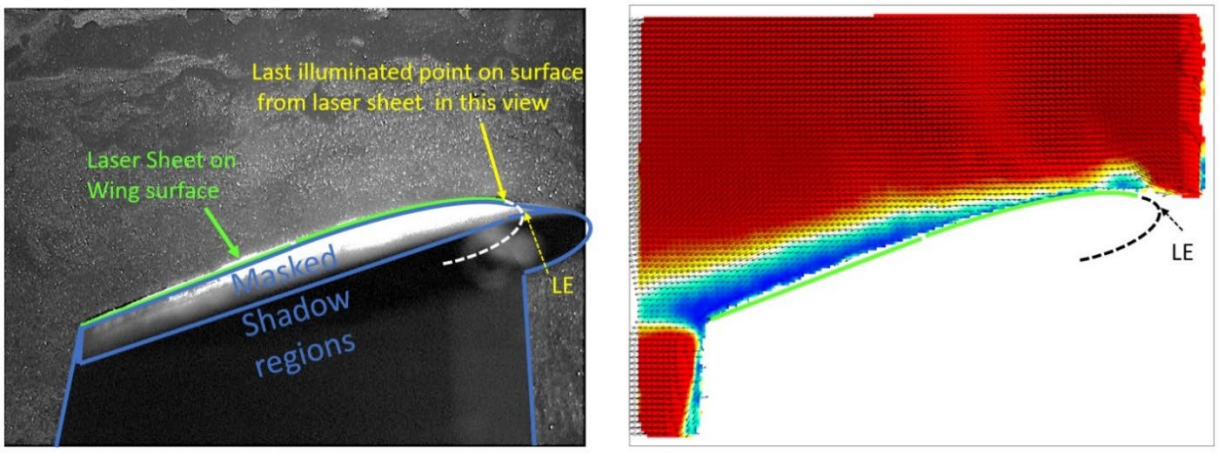

Figure 43. LE actual location in the data sets presented here.

Data is presented in the following figures for the LE view camera.

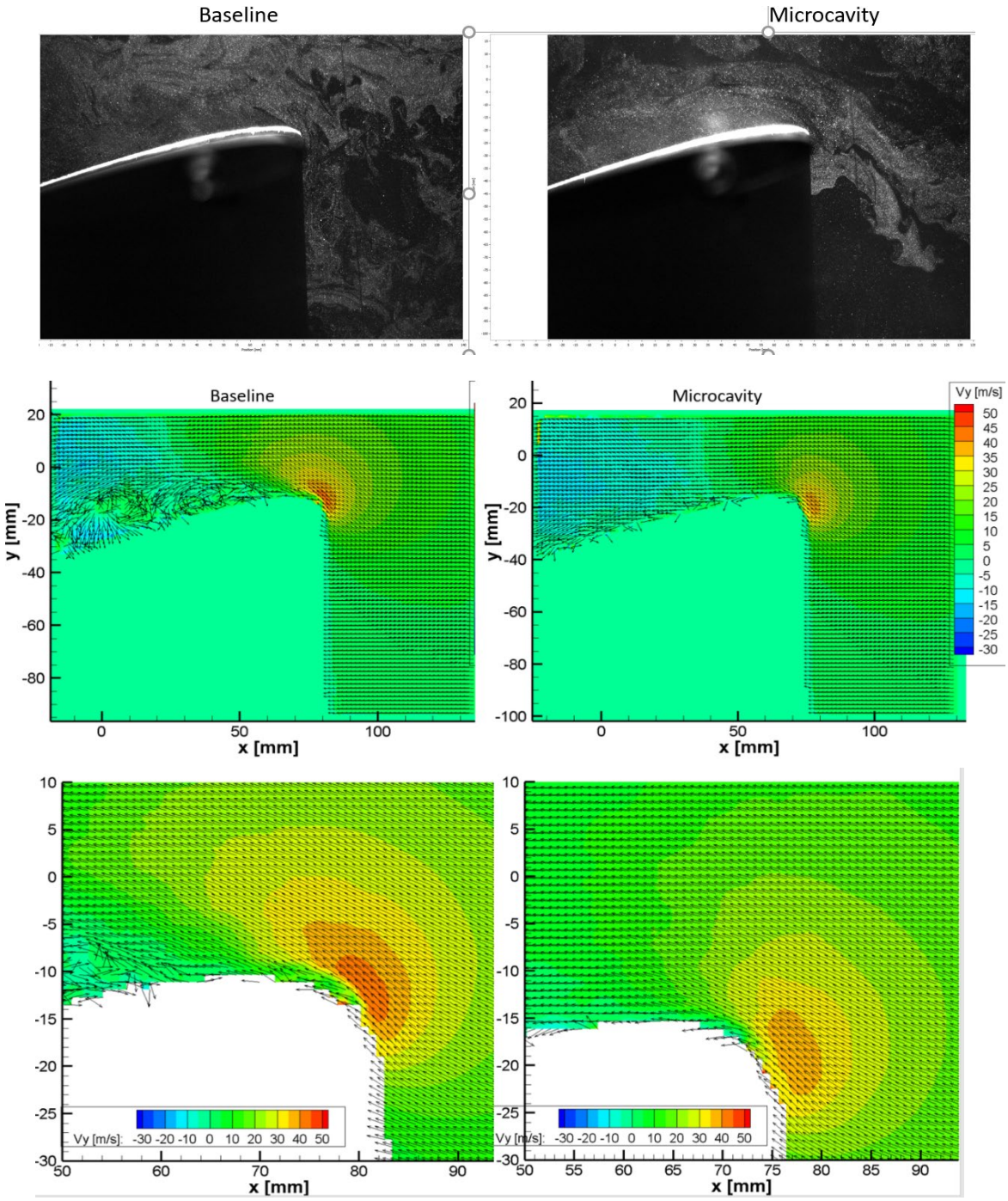

Figure 44. Averages for the Mach 0.176 and Re of 500K at 15 down phase for the LE view camera.

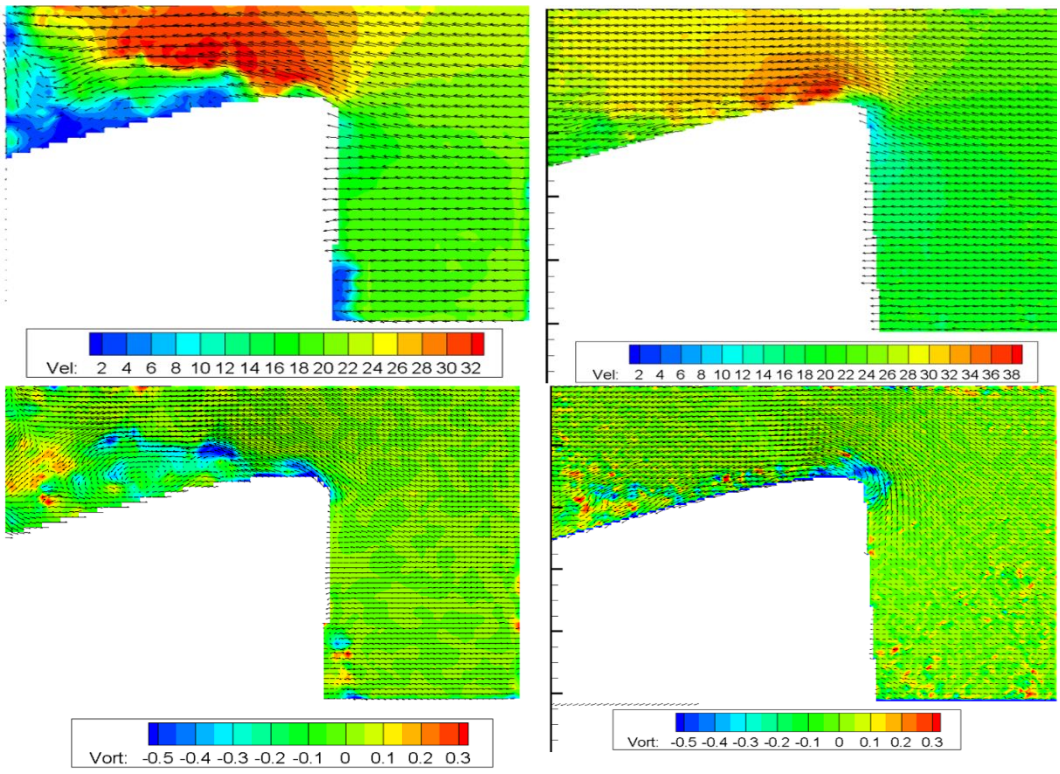

Figure 45. Instantaneous samples corresponding to Fig.5 data averages (velocity and vorticity).

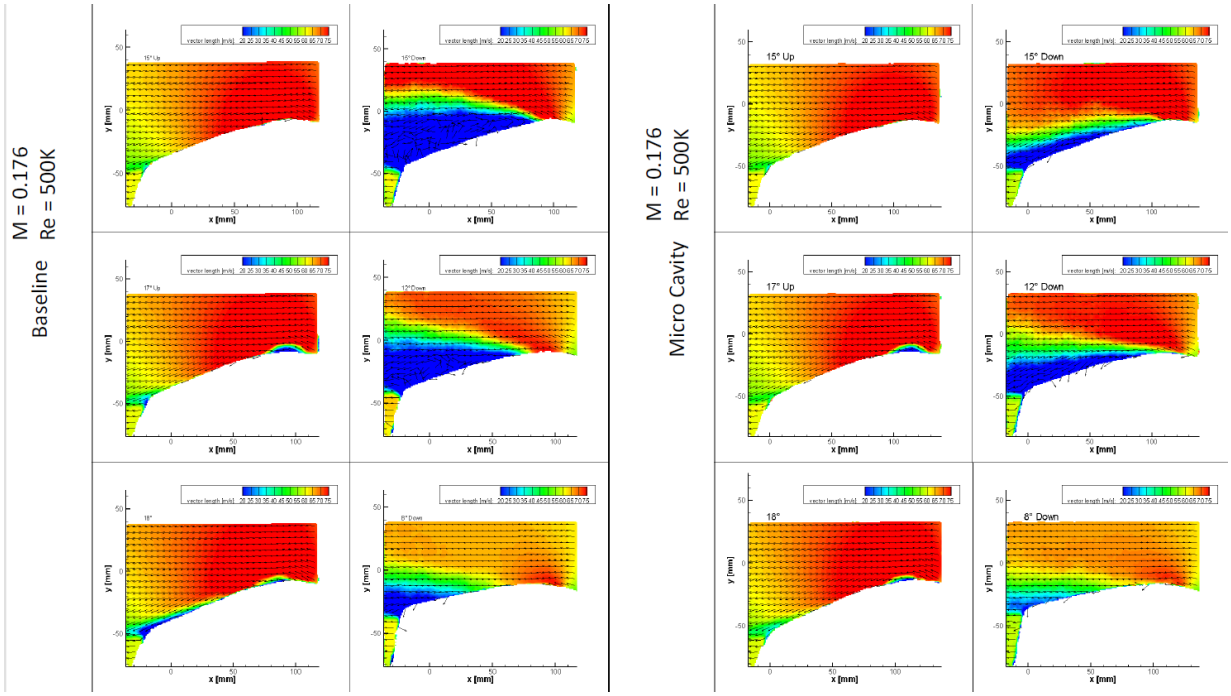

Figure 46. Baseline vs microcavity averages for various phases.

From Figure 46 above, it can be seen that full dynamic stall is not fully achieved for either the baseline or micro cavity for the 4-18° case as seen in the lower left corner. After consultation with Dr. Garmann and Dr. Visbal of AFRL it was suggested what was seen was light dynamic stall. Leading edge images can be seen in the following images shown in figure 47. Where the difference between micro cavity and baseline are compared on a per angle basis. It can be seen that the development and bursting of the laminar separation bubble is present more so in the baseline model then it is in with the microcavity primarily at the 17° and 15° down angle. This corresponds with the data shown in figure 48.

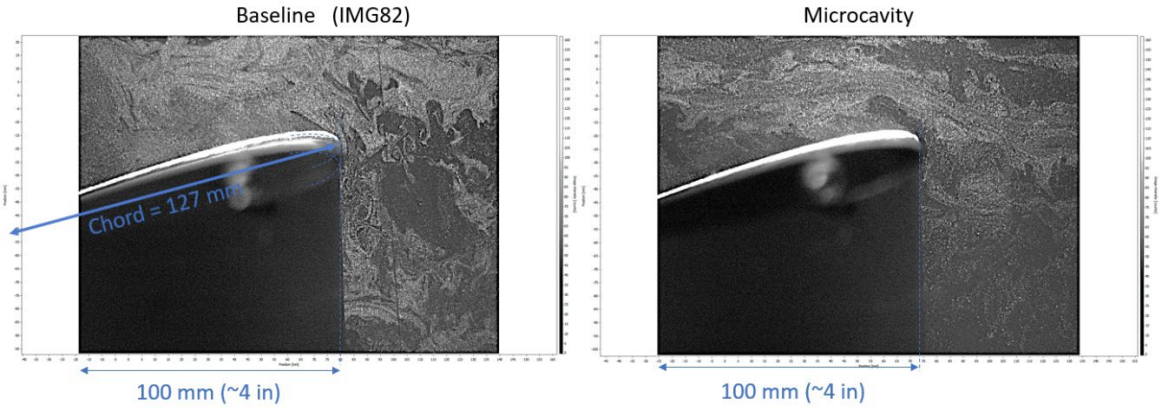

Figure 47. LE view of Baseline vs microcavity pitching data from LE view at 4-18 degree range.

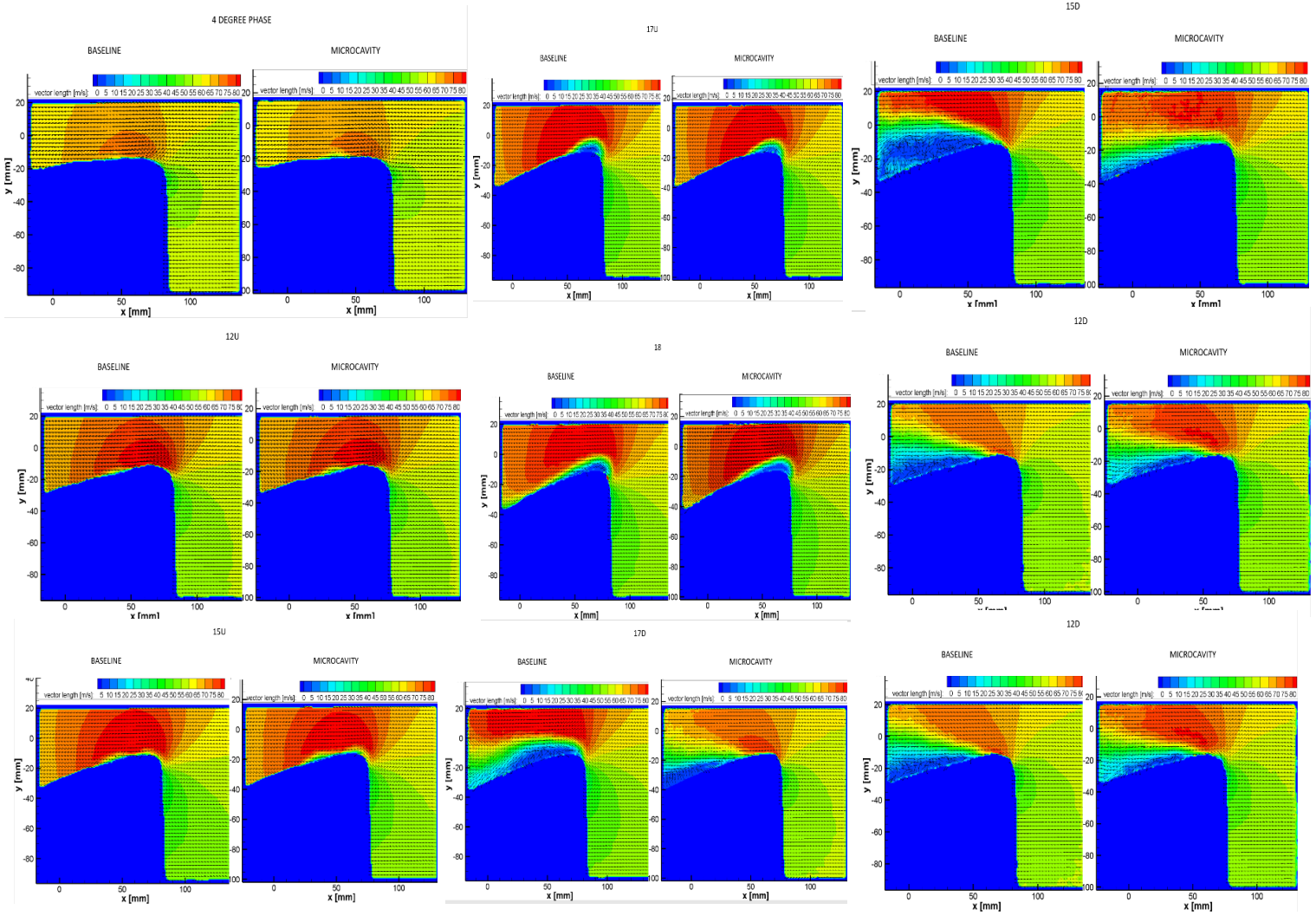

Figure 48. LE View of Baseline vs microcavity Pitching data from LE view at 4-18° range.

The findings of the current conditions do not show baseline stall (DSV) and flow seems to reattach instead (near the wing tail of TE) in what is known as 'light dynamic stall'. Notably differences between Baseline and Microcavity are LE Bubble(s) formation and evolution in the microcavity wing differs from baseline the wing with microcavity delivers some flow control over the wing and flow remains attached (without recirculation region seen in the baseline) Other observations from averages, instantaneous, and vorticity comparison shows phase locked flow (repeatable pattern at each phase); actual quantifications requiring POD or similar analyses.

It is noted that the test for 4-20 angle range did not show much of change from what was seen with 4-18 (light stall). Microcavity outperforming baseline at light dynamic stall condition but nonetheless full dynamic stall occurs for both similarly. This prompted to explore higher pitching ranges to be explored/tested (e.g. 4-20 deg, 4-22 deg) to achieve Baseline DSV.

After the limited difference found in the previous testing it was recommended a variation of the cavity be used and manufactured with a longer chord wing and a change in position of the cavity. Results of testing with the modified airfoil can be found in appendix A. But ultimately the airfoil still showed signs of dynamic stall, indicating a need for higher Mach number flow.

There are three evident reasons why this system didn't perform as expected and they are as follows:

- The wind tunnel is operating at its maximum limit of 60 m/s or a Mach number of 0.176. This is lower than the 0.2 originally intended this is the reason for the second geometry configuration.
- The turbulence intensity that the simulation was completed with is lower than the actual turbulence intensity of our tunnel

- The pitching motion is not a true sinusoid, the stepper code requires an acceleration and deacceleration to prevent skipping of steps as such the motion is achieving 30 Hz but there is not a constant acceleration as is the case with the simulation

Given these and a few other potential issues this passive system does not work at the conditions that are possible for this equipment. What this does clearly show is a potential short coming of the passive cavity. If operated outside of the required parameters, the system will not work. However, the results indicate that no negative affect on the airfoil aerodynamic performance.

4.5. Leading Edge Acoustical Resonance

A preliminary testing campaign was completed after the construction of the airfoil where an investigation was conducted to see the effects of the parameters associated with the airfoil. These parameters being, pitching speed, forcing frequency and amplitude. The testing was then narrowed down once it was understood that the Strouhal number was the primary influencer for static condition [47-50].

4.5.1. Preliminary Static Results

The first test was to determine the point of stall for the Baseline VR-12 airfoil within the wind tunnel. It was determined from this testing that a stall angle of 20° would be the target for dynamic pitching, as the baseline VR-12 undergoes a full stall while static at 20° as can be seen in the comparison in figure 49 below. At 18° the flow remains primarily attached, but when the AoA is increased to 20 the baseline VR-12 becomes fully detached, as can be seen in figure 49 below.

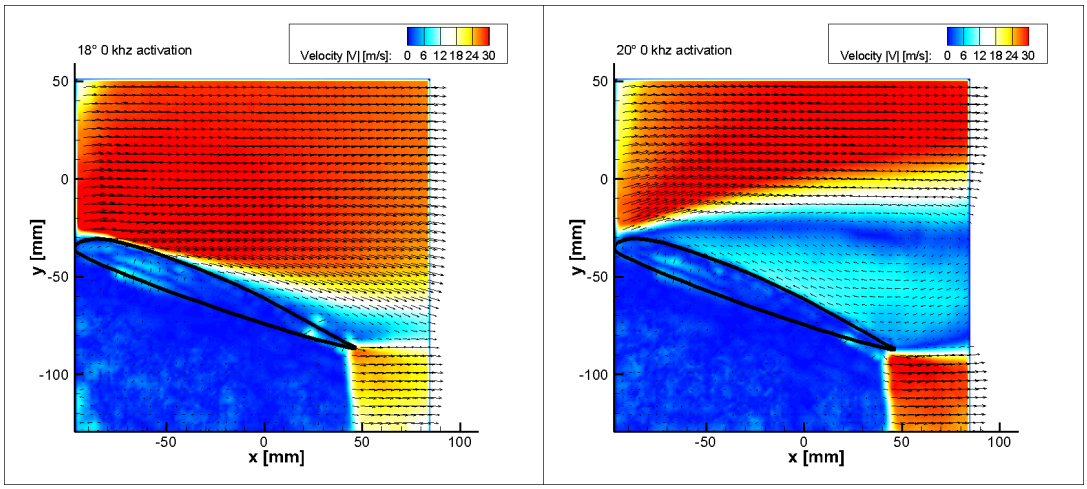

Figure 49. 600 frame average of baseline VR-12 in a static AoA 18°(left) and 20°(right) showing full separation.

Testing then continued to incorporate the actuation of the MFCs at an AoA of 20°, testing was done over a variety of frequencies, but the best result which occurred at 9 kHz which is presented below in figure 50. Where it can be seen that with the addition of the MFCs actuation the airfoil undergoes a drastic reduction in the separation occurring at 20° AoA. Thereby delaying stalling by an additional 2 degrees. 3 replicate tests were performed to ensure confidence in the results. It should be noted that this deviates from what was proposed by Visbal and Garmann for a NACA 0012. It is expected that this frequency would likely not work for the VR-12 due the variation in shape and flow conditions from what was used by Garmann and Visbal in their computational model.

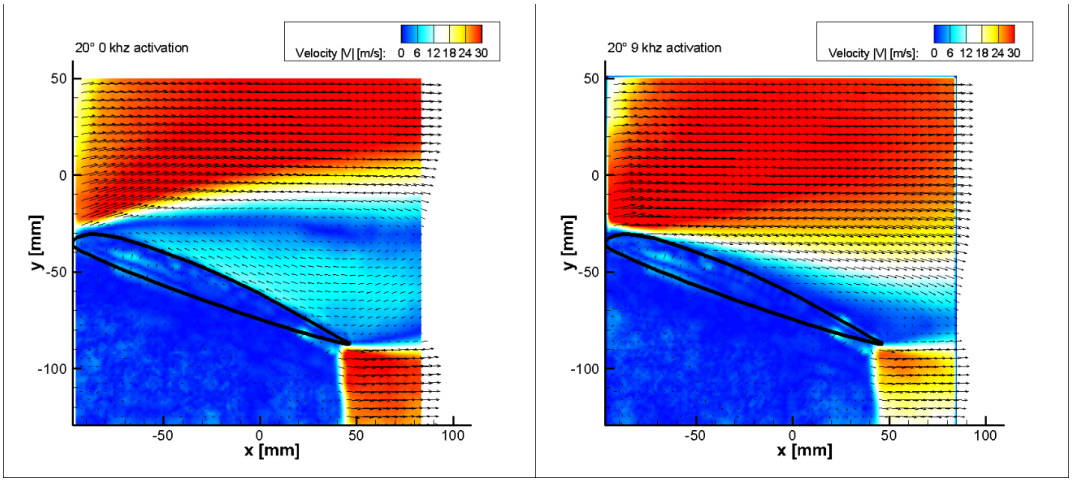

Figure 50. 600 image average of baseline VR-12(left) and 9kHz acoustic frequency(right).

4.5.2. Preliminary Pitching Results

After static cases were ran the application of the same frequencies to a pitching frequency of 7.98 Hz is shown below. From the data it was found that there were two cases where actuation provided meaningful results. These being the 9 kHz case as well as the 21 kHz case. The selection of 7.98hz was selected due to its high level of unsteady aerodynamic behavior. Where this unsteadiness caused the baseline VR-12 undergo deep dynamic stall where both a dynamic stall vortex is formed in addition to a shear layer vortex near the trailing edge. For lower pitching frequencies such as 5.08 or 2.28 Hz trailing edge vortexes dominate the flow field. A comparison of all three actuation frequencies (0, 9, 21 kHz) from left to right are shown in the following instantaneous PIV data as presented in the figures below. The figures represent the downward pitching motion starting at the max AoA of 20 degrees where every image there after represents the next degree down in AoA, until the AoA of 11 degrees is reached. At which point all three airfoils reattach and remain identical until the cycle starts again once it gets to 20°.

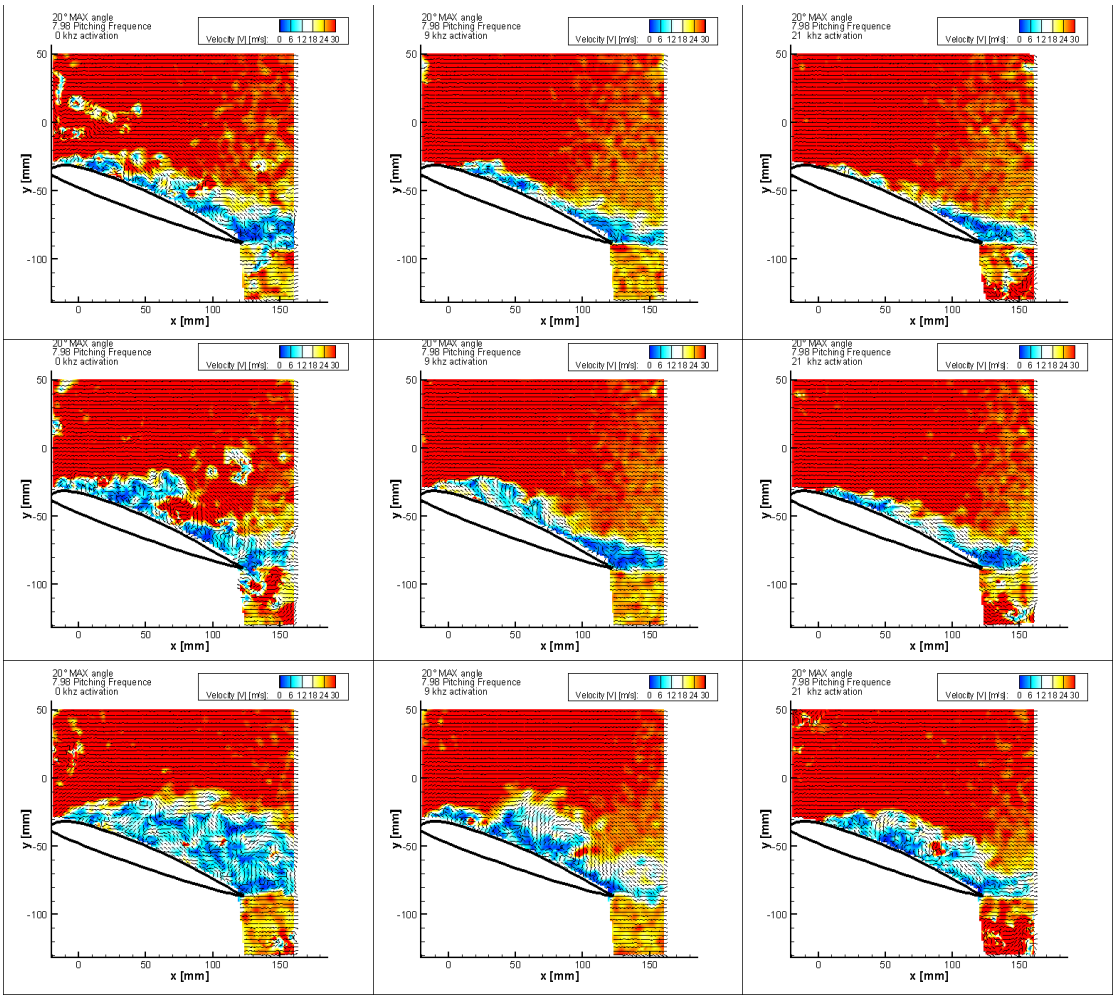

Figure 51. AoA 20,19,18 in descending order for actuation frequencies of 0kHz(left), 9 kHz(center) and 21 kHz(right).

From the figure 51-53 it can be seen that the baseline VR-12 with no actuation develops a dynamic stall vortex (DSV) at the leading edge, as well as a shear layer vortex (SLV) closer to the trailing edge. This is more apparent in the 19° AoA case. Whereas for both the 9 and 21 kHz cases remain mostly attached throughout the cycle. However, the largest demonstration of the reduction in dynamic stall can be seen in the progression from AoA 15° to 11°, where it can be seen for the baseline VR-12 the growth of the DSV as it rolls down the suction surface of the airfoil. When compared to both 9 kHz and 21 kHz where flow remains primarily attached.

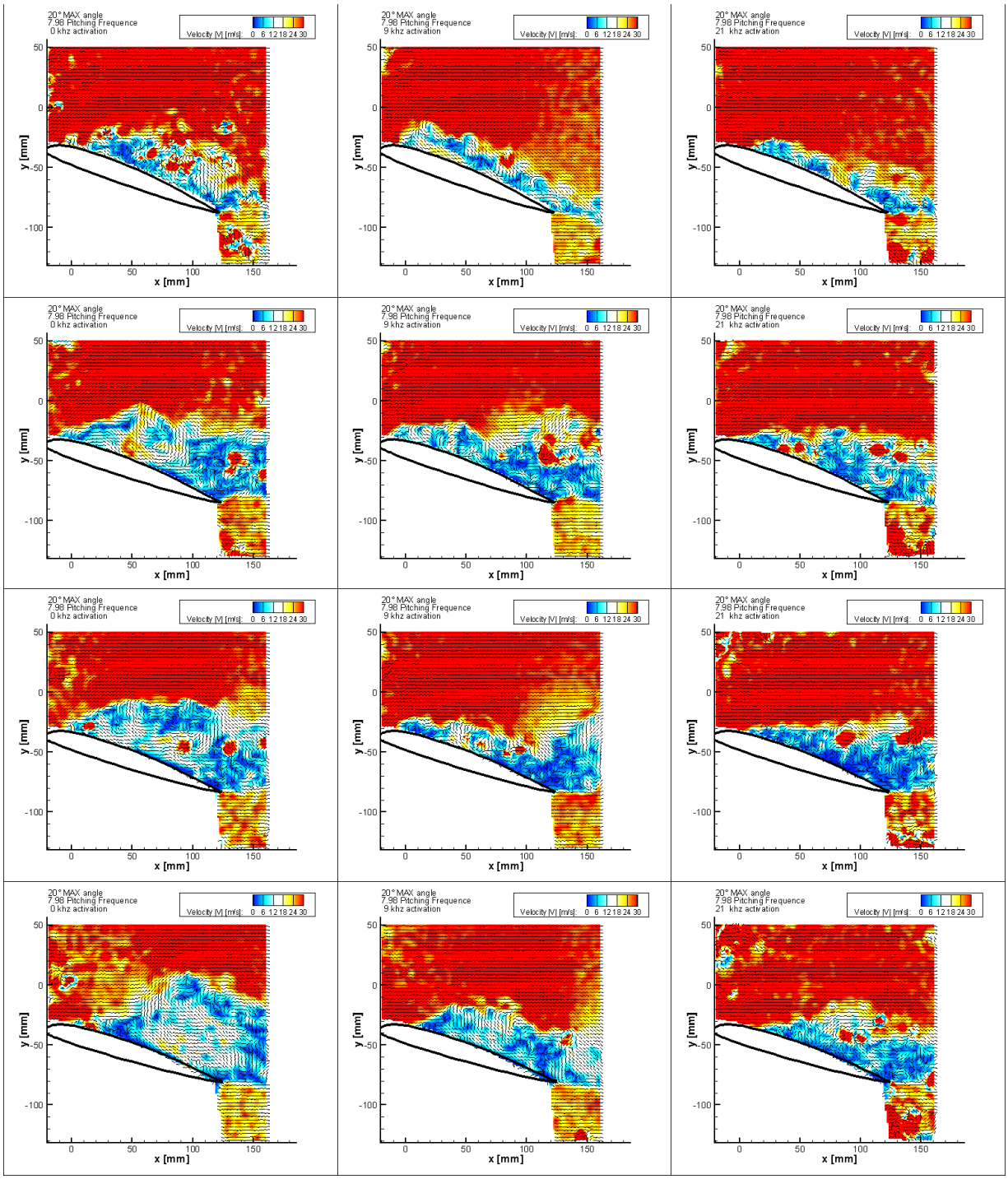

Figure 52. AoA 17,16,15,14 in descending order for actuation frequencies of 0kHz(left), 9 kHz(center) and 21 kHz(right).

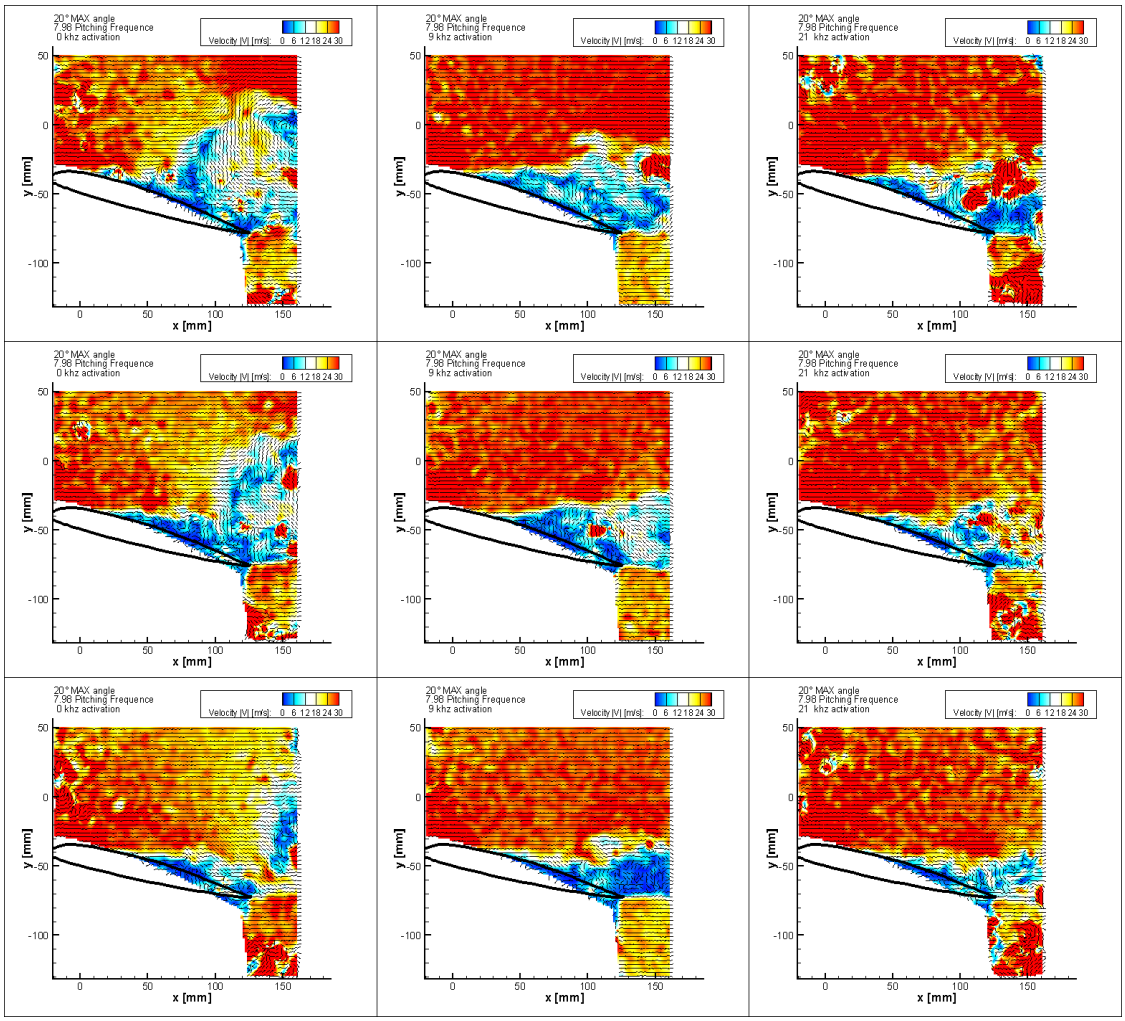

Figure 53. AoA 13,12,11 in descending order for actuation frequencies of 0kHz (left), 9 kHz (center) and 21 kHz (right).

From this data it can be concluded that acoustical vibration of MFC's on the leading edge produce a reduction in the dynamic stall for a VR-12 airfoil. The fact that two different frequencies provided improvement would indicate that there are modes to the vibration, so a third, or fourth mode could be found. Which agrees with the results shown by Visbal and Garmann [10].

During the testing of the static case, it was noted that a buildup of DEHS from the seeding system did have an effect on the performance of the vibration. As such for all data presented testing was performed with the airfoil starting clean. Though this may prove to be a

problem for prolonged pitching testing as the DEHS may build up on the airfoil and cause a reduction in performance. To adjust for this an alternative seeding method and material was used, this being propylene glycol atomized by a commercial fogging machine. The fogging machine was placed in front of the inlet of the wind tunnel's fan. The downside associated with the fogging was the coordinating of the timing between the laser sheet being on and recording occurring and the period of seeding. The fogging machines flow rate was variable during use and more or less would need to be added and multiple recordings were needed as the seeding could be come over saturated creating noise in the PIV. Although this had little effect over the flow visualization it would create areas of noise in the PIV. This can be seen in the Strouhal number of 50 section.

4.5.3. Strouhal Number of 50

From the experimental studies conducted by Visbal, Benton and Garmann [47] on high frequency forcing function, it was shown that a range of Strouhal numbers will provide control. It was shown that a Strouhal number of 50 provided the best overall. To test this theory frequencies were calculated corresponding to flow and are provided in the table below. In addition to the calculated frequencies the experimentally determined stall AoA is reported.

Table 5. Forcing frequency vs Freestream velocity and Stall AoA for baseline

Velocity (m/s)	20	25	30
Stall (AoA)	16.2	17.5	19
Forcing Frequency (Hz)	6562	8202	9843

The raw data files for 20 m/s free stream velocity can be seen below. Two cameras were used to look at the LE and the global view of the airfoil. The same methods will be used for all corresponding figures. The top row is the LE view and the bottom row images are the global view, with the baseline results shown on the left and the forcing on the right. For all images the dark region below the airfoil is the location where no laser illumination can occur.

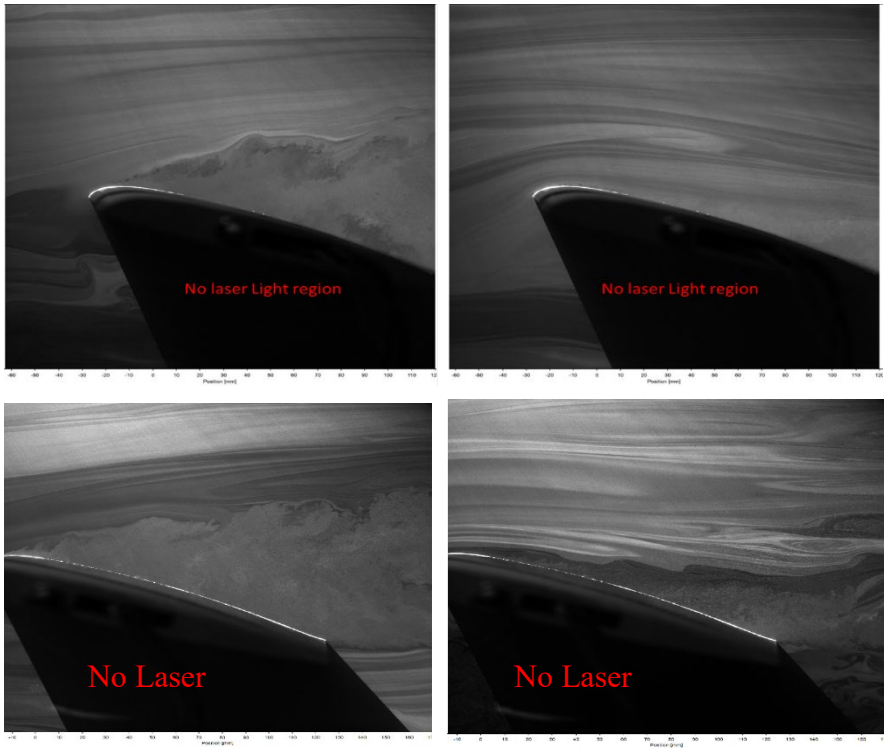

Figure 54. Leading edge camera view of baseline(left) LEAR(Right) and global view bottom row.

It can be seen from the LE view that a shear layer with vortex shedding is occurring, with a resulting burst of the LSB forming a large stall wake. The forcing on the other hand shows a continuous turbulent boundary layer near the surface of the airfoil. Instantaneous results and 300 image average results are provided.

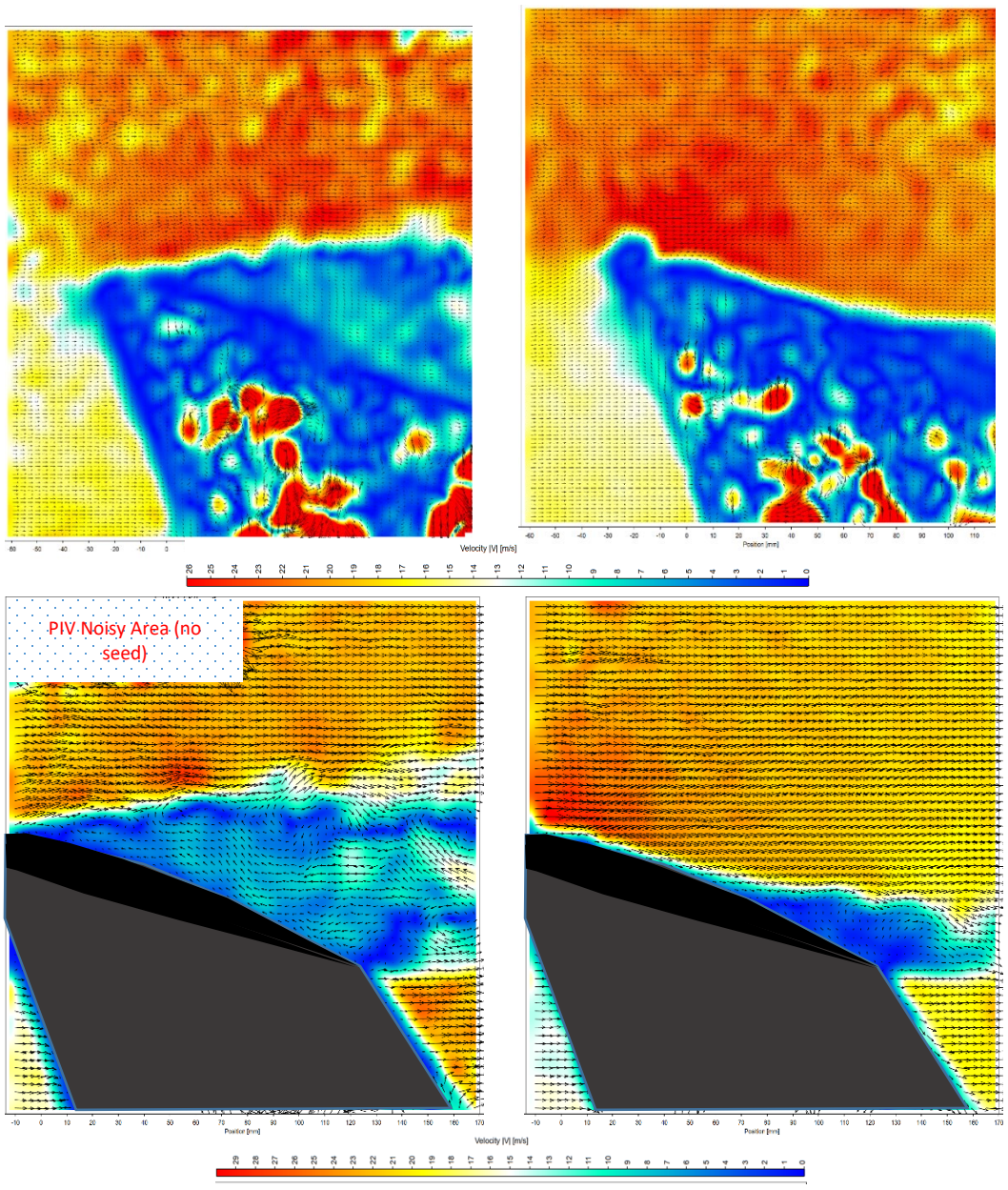

Figure 55. Instantaneous leading edge view(top), baseline(Left) and LEAR(Right), Global view(bottom).

It can be seen from the PIV results the large recirculation and stall wake forming behind the baseline airfoil. With the forcing system a slight TEV has formed due to curl coming up over the TE, similar to the what is expected for an airfoil at an AoA lower than the stall angle. It can be noted that a small turbulent boundary layer can be seen where the vicious interactions are

occurring. Indicating a dampening or stabilization of the LSB, causing immediate reattachment. This is further shown by the average PIV results shown in the figure 56 below.

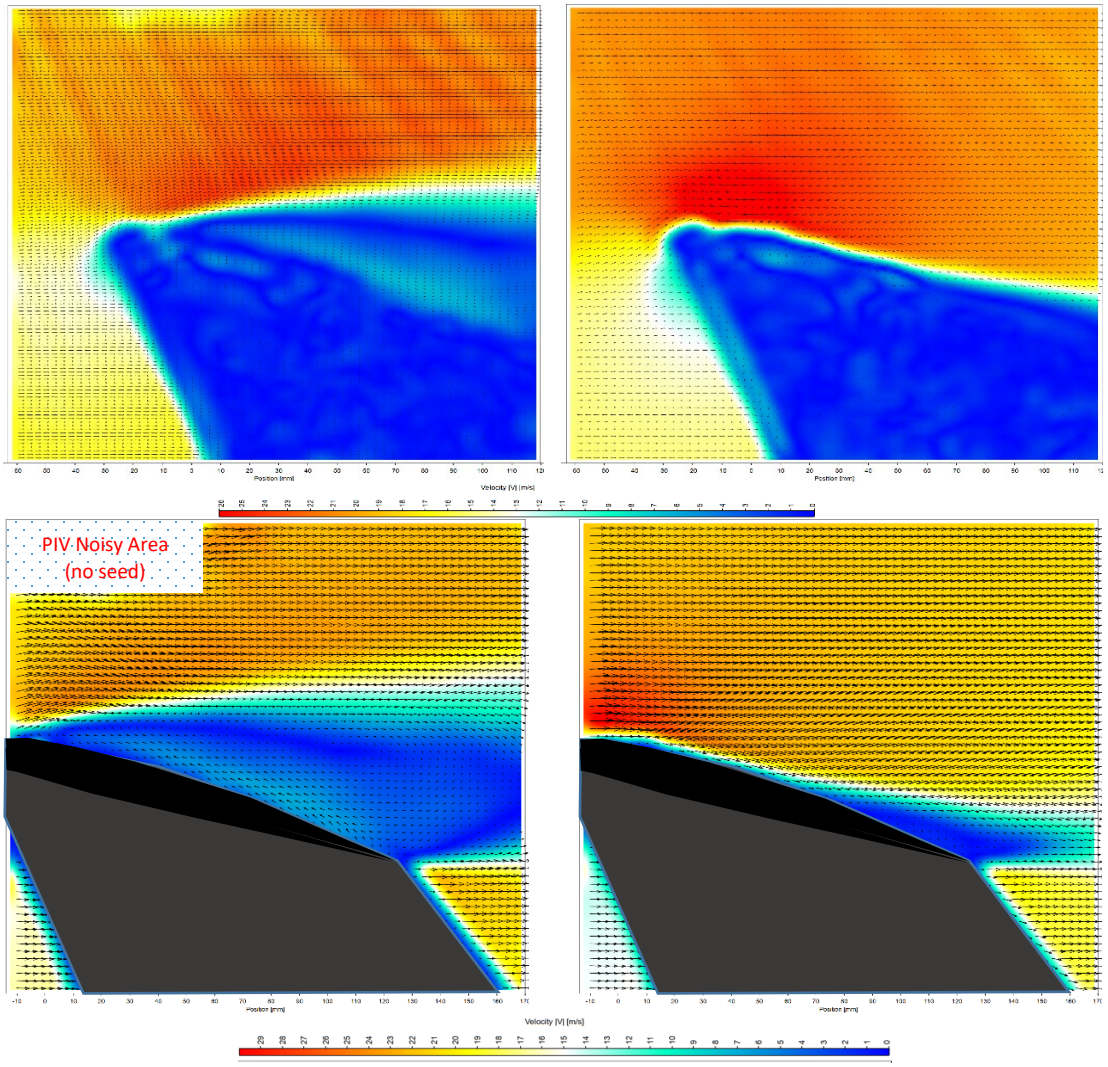

Figure 56. 300 image average leading edge view(top), baseline(Left) and LEAR(Right), Global view(bottom).

To better elucidate the effects of the leading edge the LE camera was moved closer to the wind tunnel focusing on approximately 2 cm of the LE as shown in figure 57 below. Flow visualization images for 25 m/s can be seen below with the improved LE camera view in figure 58. It can be seen from the baseline data a shear layer has formed at the LE, from this shear layer vortex shedding is seen. This is caused by the LSB forming and subsequently bursting. Whereas

the LEAR again dampens the LSB and has a turbulent reattachment. It can be seen that again the LEAR maintains an attachment with a slight development of a TEV. This effect is further emphasized when compared to the baseline global view. The length between vortexes was measured for a few frames and was to get an approximation of the shedding frequency. By use of the equation four below. Where U is the average velocity across the shear layer and λ is the measured distance.

$$f = \frac{U}{\lambda} \tag{4}$$

The calculated shedding frequency was approximately 6000-8000 Hz, depending on the frames. Suggesting the selected forcing frequency was selected well, further supporting the LEAR concept. The averaged PIV results for these same flow visualizations can be seen in figure 59. Where clear detachment and recirculation can be seen for the baseline VR-12 airfoil, and slight recirculation at the trailing edge for the LEAR. This recirculation likely being from the TEV.

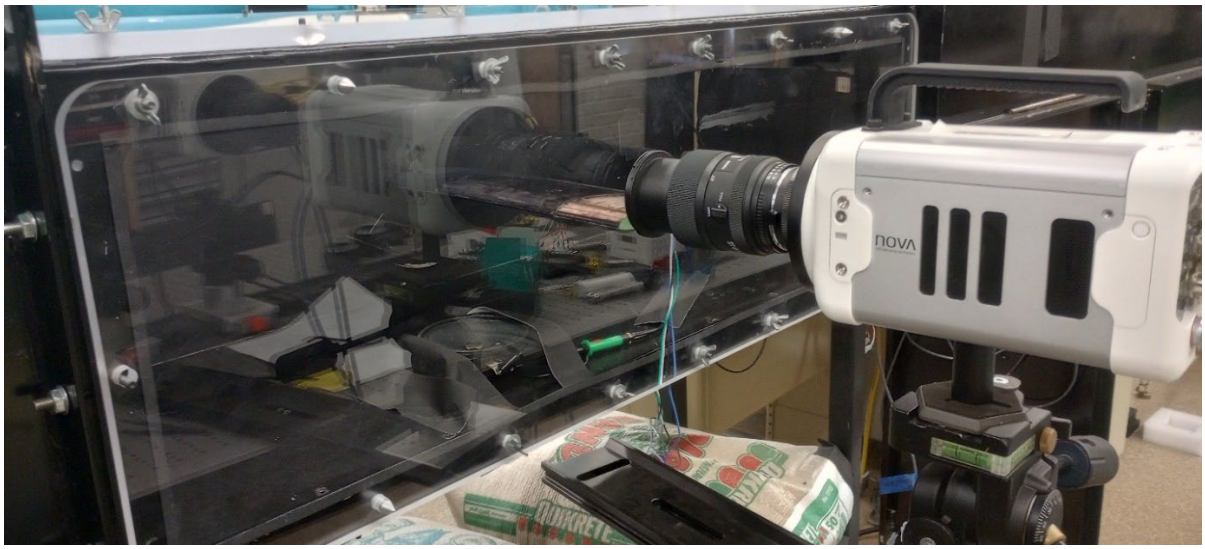

Figure 57. Adjusted camera position for closer imaging.

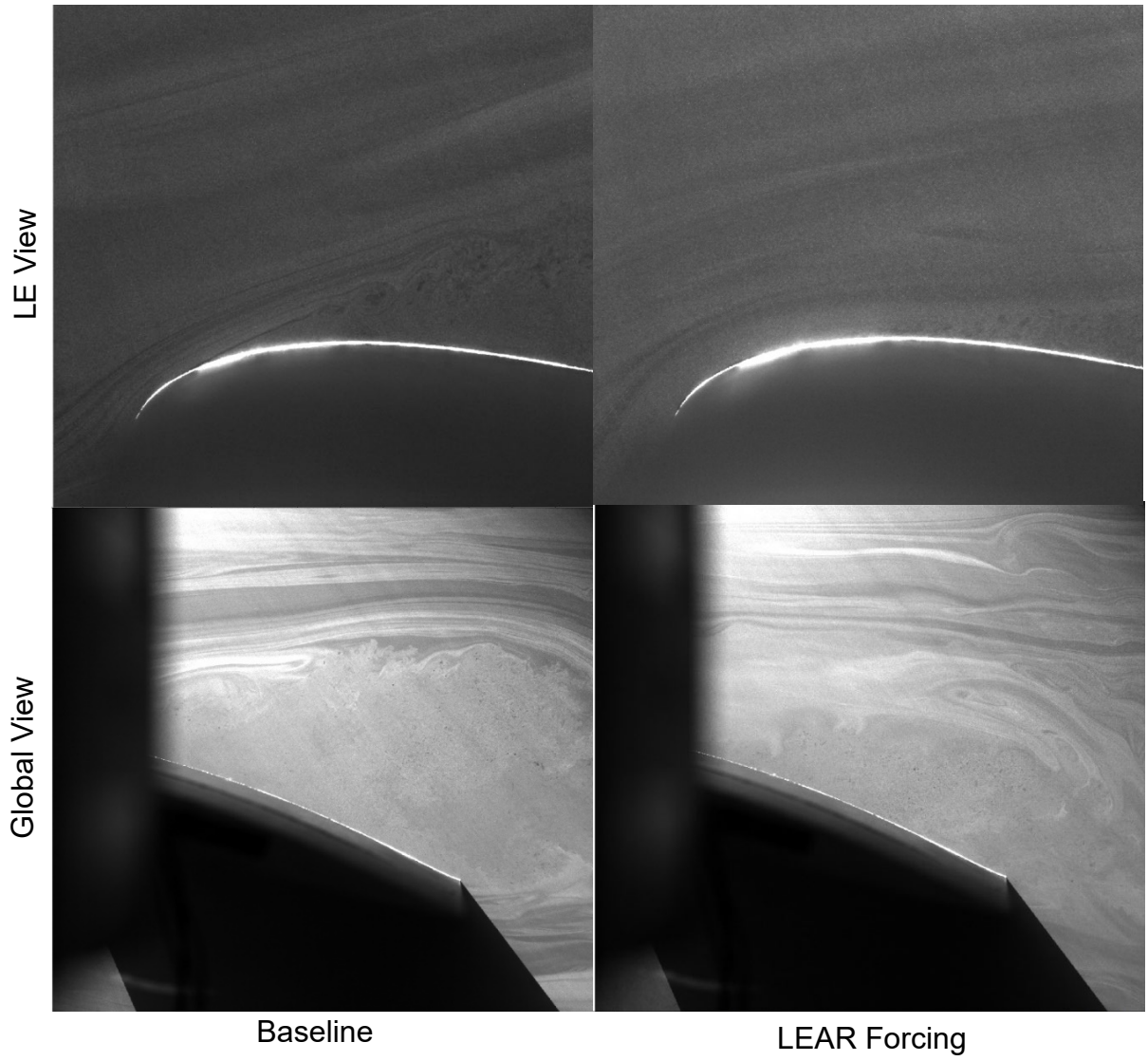

Figure 58. Comparison of flow visualization between the non-forced airfoil(left) and forced (right).

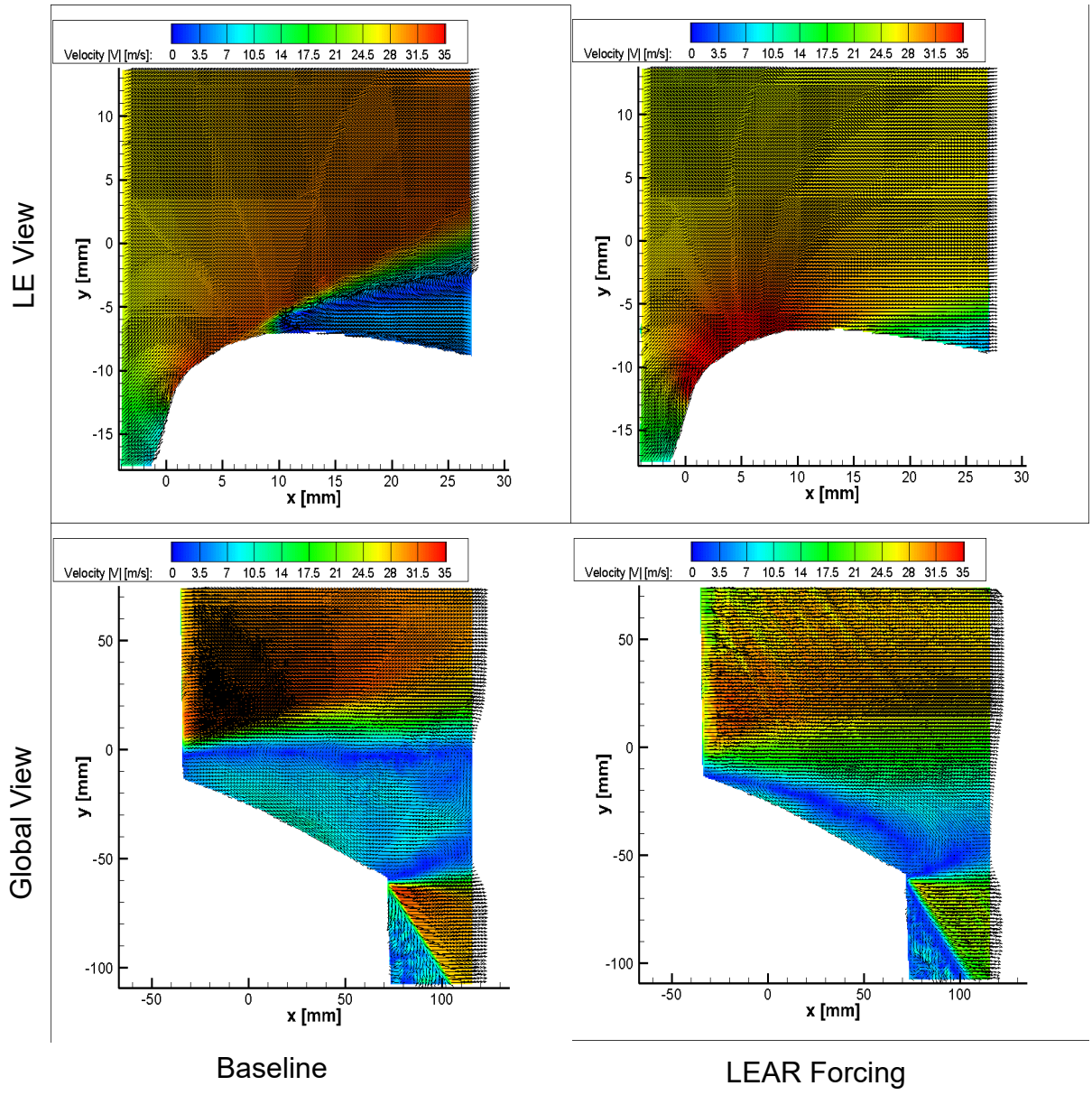

Figure 59. 300 image average for 17.5° AoA LE views(right) body view.

One last method was used to help support the effects shown by LEAR to be acoustic in nature was the implementation of a speaker upwind pointing at the LE. This speaker was fed the same frequency and amplitude while the tunnel was running with similar results.

5. CONCLUSIONS

Four types of stall mitigation where designed, fabricated and tested for the two stall conditions, these being static stall and dynamic stall caused during pitching. The four methods were permanent droop of the leading and trailing edge, active leading and trailing edge droop(active morphing), microcavity geometry and a novel leading-edge acoustical resonance (LEAR). While each showed potential, one demonstrated the highest effectiveness this being the active morphing. In this case the reduction of the stall both dynamic and static is without question. The downside associated with this methodology is the complexity associated with its construction, operation and yet to be determined lifespan. The permeant droop showed promise but was not as effective as the morphing this is due to the fact that the droop has a poor response to the low angles of AoA. The next most effective strategy was the LEAR, set with a forcing frequency that matches a St=50. Where the LSB was shown to be reduced in the static stall scenario, showing it is possible to control and good agreement with existing studies. Though the positive effects in dynamic stall where not as significant as the morphing, some reduction was seen. This implies that further refinement is necessary. This could be in the form of a corrected forcing frequency to match the pitching increase of angle of attack or a change of the wave form function may need to be changed to get the desired results. Visbal et al. allude to this in their paper[47-48].

5.1. Recommendations

A few items would be recommended for any future work conducted in these designs, some of these have been alluded to throughout the paper but are put more succinctly here with a few additions:

- Active Morphing
  - Investigation into the effect of out of phase control
  - Incorporate onboard pressure sensors and one MFC on the LE and TE to allow for a closed loop feedback
    - This does come at the cost of more computational power and a slower response
    - Use machine learning algorithms to locate proper sensor position
  - Fabricate and use fixtures during the glue up and assembly process
  - Simplify both the mechanical and electrical systems
    - Mechanical design by incorporating the compliant hinge and ribs into one assembly
    - Design and purchase one MFC assembly for the LE and TE
- Design one PCB incorporating the DC-DC converters, IMU as the design currently is bulkier due to the use of off the shelf components
- Microcavity
  - Rerun experiments with the new closed loop wind tunnel with high velocity capabilities and lower turbulence intensities
- LEAR

- Investigate the corrected forcing frequency to improve performance during pitching [47-48]
- Investigate alternative wave forms such as square, or ramp as they can provide multiple frequencies improving the effectiveness of the LEAR [47-48]

REFERENCES

[1] El-Adawy, M., Heikal, M.R., Rashid, A., Aziz, A., Opatola, R. A., "Stereoscopic Particle Image Velocimetry Measurmenets: Principles and Applications," *Alexandira Engineering Journal*, Vol 60, 3327-3344, 2021.

[2] Melling, A., "Tracer Particles and Seeding for Particle Image Velocimetry," *Measurement Science and Technology,* Vol. 8, 1997.

[3] Raffel, M., Willert, C. E., Scarano, F., Kähler, C. Wereley, S. T., and Kompenhans, J., Particle Image Velocimetry: A Practical Guide, Springer, 2018

[4] DaVis Flow Master Software, LaVision, Inc. 2019

[5] Adrian, R. J., and Westerweel, J., 2011, Particle Image Velocimetry, Cambridge University Press, New York.

[7] Liu, T. & Sullivan, J.P., "Pressure and Temperature Sensitive Paints," Springer, 2005.

[8] Pressure Sensitive Paints, Innovative Scientific Solutions Inc. https://innssi.com/psp/

[9] Fast Pressure Sensitive Paints, Innovative Scientific Solutions Inc. https://innssi.com/fast-pressure-sensitive-paints/ 2020.

[10] Visbal M. R. and Garmann D. J., "Passive control of dynamic stall using a flow-driven micro-cavity actuator," AIAA-2022-0708, AIAA SciTech Forum, San Diego CA and Virtual, January 3-7, 2022

[11] Visbal M. R. and Garmann D. J., and Estevadeordal J., "Computational/Experimental Investigation of Passive Control of Dynamic Stall Using a Micro-Cavity Actuator," submitted to AIAA Aviation 2023

[12] O'Meara M. M. and Mueller T.J., "Laminar Separation Bubble Characteristics on an Airfoil at Low Ryenolds Numbers" AIAA/ASME fourth Fluid Mechanics 1986

[13] Munson, B.R., Young D.F., and Okiishi T.H., "Fundamentals of Fluid Mechanics". Hoboken, NJ: Wiley, 2009.

[14] White, F.M., "Viscous Fluid Flow". New York, NY: McGraw-Hill, 2011.

[15] Schlichting, H., and Klaus., "Boundary-Layer Theory"., translated by J. Kestin. Berlin, Germany: Springer, 1979

[16] Wang, G., Lewalle, J., Glauser, M., and Walczak, J., 2013, "Investigation of the benefits of unsteady blowing actuation on a 2D wind turbine blade," Journal of Turbulence, 14(1), pp. 165-189.

[17] Gul, M., Uzol, O., and Akmandor, I. S., 2014, "An Experimental Study on Active Flow Control Using Synthetic Jet Actuators over S809 Airfoil," Journal of Physics: Conference Series, 524(1), p. 012101.

[18] Tang, H., Salunkhe, P., Zheng, Y., Du, J., and Wu, Y., 2014, "On the use of synthetic jet actuator arrays for active flow separation control," Experimental Thermal and Fluid Science, 57, pp. 1-10.

[19] Walker, S., and Segawa, T., 2012, "Mitigation of flow separation using DBD plasma actuators on airfoils: A tool for more efficient wind turbine operation," Renewable Energy, 42, pp. 105-110. 62

[20] Francioso, L., Pascali, C. D., Pescini, E., Giorgi, M. G. D., and Siciliano, P., 2016, "Modeling, fabrication and plasma actuator coupling of flexible pressure sensors for flow separation detection and control in aeronautical applications," Journal of Physics D: Applied Physics, 49(23), p. 235201.

[21] Stolt A., "Experimental Evaluation of a NACA 0021 Airfoil Employing Shape-Memory Alloy for Active Flow Control," M.S. Thesis, North Dakota State University, 2018

[22] Macro Fiber Composites, Smart Material Corp, https://www.smart-material.com/MFC-product-mainV2.html

[23] LaCroix B. "On the Mechanics, Computational Modeling, and Design Implementation of Piezoelectric Actuators on Micro Air Vehicles" Doctoral Dissertation, University of Florida 2013 Doi: 10.2514/6.2019

[24] Sprengeler T., Refling W., Suzen Y. B., and Estevadeordal J., "Computational Investigation of Effects of Leading and Trailing Edge Deflections on VR-12 Airfoil Aerodynamic Characteristics," AIAA2022-1950, AIAA SciTech Forum, January 3-7, 2022, San Diego, CA & Virtual.

[25] Sprengeler T., A Numerical Study and Optimization of a Morphing and Pitching Boeing VERTOL VR-12 Rotorcraft Airfoil, MS Thesis, North Dakota State University, July 2022.

[26] Goecks G., Vinicius, Camara Leal, Pedro, White, Trent, Valasek, John, Hartl, Darren, "Control of Morphing Wing Shapes with Deep Reinforcement Learning," 2018

[27] Brunton, S., Kutz, N., "Data-Driven Science and Engineering, Machine learning, dynamical systems and control." Cambridge University Press, 2019

[28] Plantim De Hugues P., McAlister K. W., and Tung C., "Effect of an Extendable Slat on the Stall Behavior of a VR-12 Airfoil," 1993

[29] Martin P. and Mcalister K. and Chandrasekhara M.S., and Geissler W., "Dynamic Stall Measurements and Computations for a VR-12 Airfoil with a Variable Droop Leading Edge," 2013

[30] Modarres, R., Peters, D., Gaskill, J., “Dynamic Stall Model with Circulation Pulse and Static Hysterisis for NACA 0012 and VR-12 Airfoils” Journal of the American Helicopter Society, 2016

[31] Refling W., Sprengeler T., Suzen Y. B., and Estevadeordal J., “Experimental Investigation of Morphing Flow Control for Unsteady Aerodynamic Applications,” AIAA2022-1958, January 3-7, 2022, San Diego, CA & Virtual

[32] Gandhi F., Anusonti-Inthra P. “Skin Design Studies for Variable Camber Morphing Airfoils,” Journal Smart Materials and Structures Volume 17, No. 1, 2008 pp. 1-8; Doi: 10.1088/9064

[33] Gandhi F. and Hayden E., “Design, Development and hover testing of a helicopter rotor blade chord extension morphing system,” Journal Smart Materials and Structures Volume 24, 2015 pp 14; Doi:10.1088/9064

[34] Olympio K.R, Gandhi F., “Flexible Skins for Morphing Aircraft Using Cellular Honeycomb Cores” Journal of Intelligent Material Systems and Structures Volume 21 No. 17, 2010 pp 1719-1735

[35] Moulton B. and Hunsaker D. F.. "3D-Printed Wings with Morphing Trailing-Edge Technology," AIAA 2021-0351. AIAA Scitech 2021 Forum. January 2021. Doi: 10.2514/6.2021-0351

[36] Wang Q., Zhao Q, “Rotor aerodynamic shape design for improving performance of an unmanned helicopter,” Aerospace Science and Technology, Vol. 87, 2019, pg. 478-487

[37] Plantim De Hugues P., McAlister K. W., and Tung C., “Effect of an Extendable Slat on the Stall Behavior of a VR-12 Airfoil,” 1993

[38] Martin P., and Mcalister K., and Chandrasekhara M.S, and Geissler, W. “Dynamic Stall Measurements and Computations for a VR-12 Airfoil with a Variable Droop Leading Edge,” 2013

[39] Chandrasekhara M. S., Martin P. B., and Tung C., “Compressible Dynamic Stall Control using a Variable Droop Leading Edge Airfoil,” Journal of Aircraft, Vol. 41, 2004, pg. 862-869

[40] Mohammad A., Suzen, Y.B., Ol, M, “Numerical Simulations of Pitching Airfoil Flow Fields for MAV Applications,” 2019

[41] Huntley S.J., Woods B.K., and Allen C.B., "Computational Analysis of the Aerodynamics of Camber Morphing," AIAA 2019-2914. AIAA Aviation 2019 Forum. June 2019.

[42] Jain R., Le Pape A., Grubb A., Costes M., Richez F., Smith M., “High-resolution computational fluid dynamics predictions for the static and dynamic stall of a finite-span OA209 wing,” Journal of Fluids and Structures, Vol. 78, 2018, pp. 126-145.

[43] Tomek K.L, Ullah A.H, Fabijanic C, Estevadeordal J. Experimental Investigation of Dynamic Stall on Pitching Swept Finite-Aspect-Ratio Wings. AIAA Scitech 2020 Forum; AIAA2020-1980.

[44] Ullah A.H., Fabijanic C., Refling W., Estevadeordal J., Experimental Investigation of the Effect of Sweep on a Pitching Finite-Aspect-Ratio Wing. AIAA Scitech 2021 Forum; AIAA2021-1733.

[45] Visbal M.R., and Garmann D.J. Effect of sweep on dynamic stall of a pitching finite-aspect-ratio wing. *AIAA Journal*. 2019; **57**(8):3274-89.

[46] Xiaohua Li, Dana Grecov, Zheng Guo, and Zhongxi Hou, "Influence of Unsteady and Kinematic Parameters on Aerodynamic Characteristics of a Pitching Airfoil," Journal of Aerospace Engineering, Vol. 32, 2019

[47] Visbal M.R., and Benton S.I., "Exploration of High Frequency Control of Dynamic Stall Using Large-Eddy Simulations" *AIAA Journal. 2018 DOI 10.2514/1.1056720*

[48] Benton S.I., and Visbal M.R., "High-frequency forcing to mitigate unsteady separation from a busting separation bubble" *Physical Review Fluids 3* 2018 DOI 10.1103/3.013907

[49] Benton S.I., and Visbal M.R., "Investigation of High-Frequency Separation Control Mechanisms for Delay of Unsteady Separation" *AIAA Aviation*. 2016 Forum. June 2016

[50] Visbal, M.R., "Analysis of the Onset of Dyanamic Stall Using high-Fidelity Large Eddy Simulations" *AIAA*

[51] Ahuja, K. K., Whipkey, R. R., and Jones, G. S., 1983, "Control of Turbulent Boundary Layer Flows by Sound," AlAA 8th Aeroacoustics Conference.

[52] Collins, F. G., and Zelenevitz, J., 1975, "Influence of Sound upon Separated Flow Over Wings," AIAA J., 13(3), pp. 408–410.

[53] Schubauer, G. B., and Skramstad, H. K., 1947, "Laminar Boundary-Layer Oscillations and Transition on a Flat Plate," J. Res. Natl. Inst. Stand., 38(2), p. 251.

[54] Celik, A., Mitra, A., Agarwal, T., Clark, J., Jacobi, I., and Cukurel, B. (November 16, 2023). "Exploring Physics of Acoustic Flow Control Over Airfoils Toward Potential Application to High Work and Lift Turbines." ASME. J. Turbomach. March 2024; 146(3): 031001.

[55] Refling W., Sprengeler T., Suzen Y. B., and Estevadeordal J., "Experimental analysis of the effect of active morphing of a VR-12 airfoil for unsteady aerodynamics optimization," AIAA2023-2611, AIAA SciTech Forum, 23-27 January 2023, National Harbor, MD & Online, doi: 10.2514/6.2023-2611.

[56] Refling W., Estevadeordal J., Suzen, Y. B., "Experimental investigation of the effects of acoustical vibration at the leading edge of a VR-12 airfoil." AIAA-Aviation 2024

APPENDIX A. PIV RESULTS FOR 152.4MM CHORD NACA 0012 AIRFOIL WITH MICRO CAVITY UNDERGOING A PITCHING CYCLE

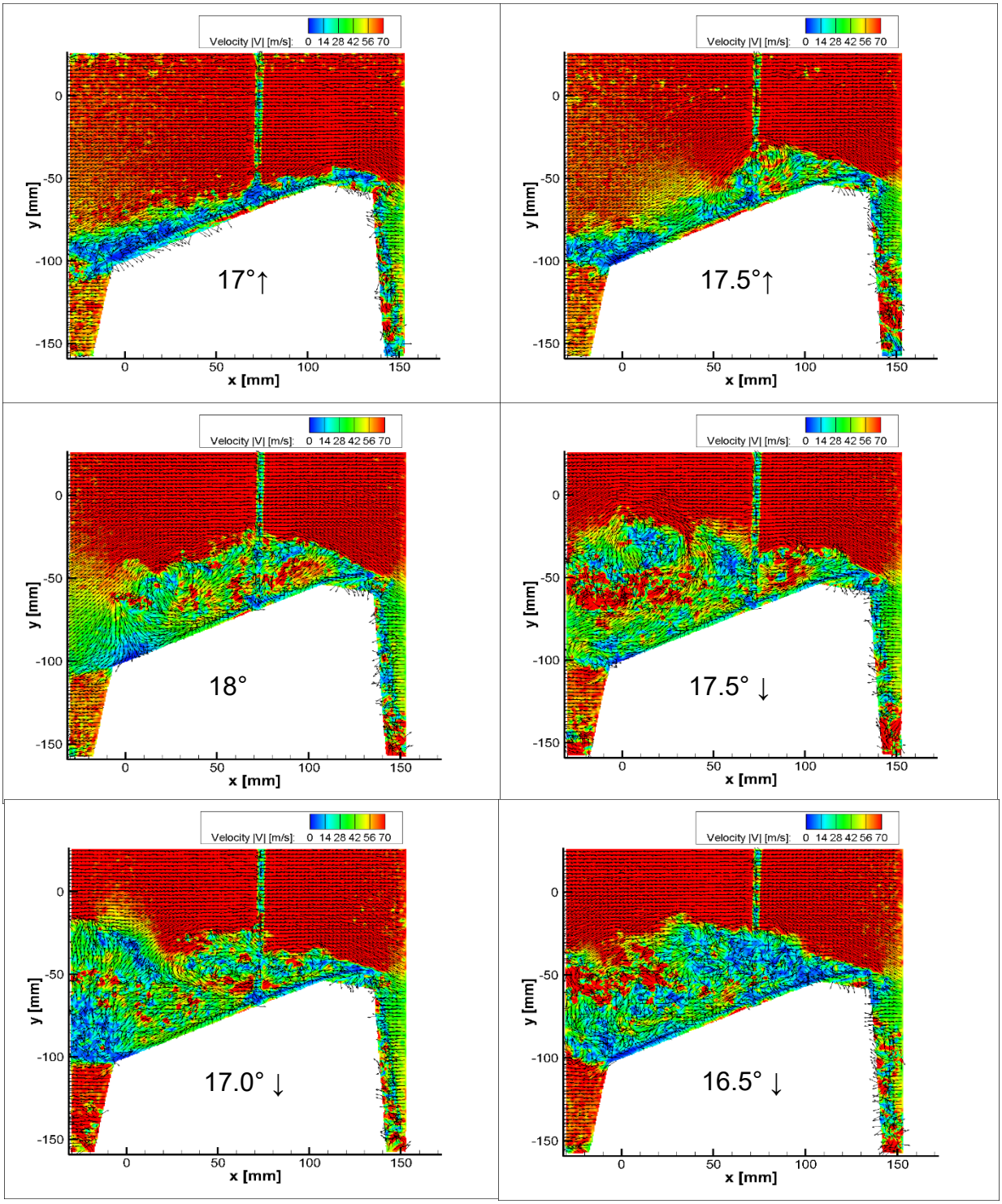

Figure A1. 152.5mm Microcavity undergoing pitching motion and dynamic stall.

APPENDIX B. MORPHING DAQ RAW DATA SAMPLE

14:03:53.995 -> -10.92 -178.59 2.94 -170.76 0.59 L.E.AnalogVal: 0.00 T.E.AnalogVal: 0.00
14:03:53.995 -> -8.38 -178.54 2.99 -197.14 0.67 L.E.AnalogVal: 12.90 T.E.AnalogVal: 12.90
14:03:53.995 -> -5.20 -178.52 3.26 -245.34 0.64 L.E.AnalogVal: 38.23 T.E.AnalogVal: 38.23
14:03:54.042 -> -2.00 -178.46 4.98 -249.16 1.07 L.E.AnalogVal: 63.75 T.E.AnalogVal: 63.75
14:03:54.042 -> 1.19 -178.39 5.17 -249.57 1.36 L.E.AnalogVal: 89.17 T.E.AnalogVal: 89.17
14:03:54.042 -> 4.36 -178.33 5.49 -249.76 1.33 L.E.AnalogVal: 114.43 T.E.AnalogVal: 114.43
14:03:54.042 -> 7.26 -178.28 4.29 -229.05 1.05 L.E.AnalogVal: 137.58 T.E.AnalogVal: 137.58
14:03:54.089 -> 8.77 -178.25 0.79 -116.30 0.45 L.E.AnalogVal: 149.55 T.E.AnalogVal: 149.55
14:03:54.089 -> 9.91 -178.24 2.01 -88.90 0.01 L.E.AnalogVal: 158.67 T.E.AnalogVal: 158.67
14:03:54.089 -> 10.84 -178.24 1.01 -71.07 -0.14 L.E.AnalogVal: 166.07 T.E.AnalogVal: 166.07
14:03:54.136 -> 11.84 -178.21 0.55 -76.52 0.05 L.E.AnalogVal: 174.04 T.E.AnalogVal: 174.04
14:03:54.136 -> 11.54 -178.21 1.05 26.81 -0.53 L.E.AnalogVal: 171.66 T.E.AnalogVal: 171.66
14:03:54.136 -> 10.94 -178.21 0.99 52.50 -0.60 L.E.AnalogVal: 166.90 T.E.AnalogVal: 166.90
14:03:54.136 -> 10.59 -178.24 -2.79 33.47 -0.59 L.E.AnalogVal: 164.11 T.E.AnalogVal: 164.11
14:03:54.183 -> 10.31 -178.25 -0.53 23.45 -0.68 L.E.AnalogVal: 161.86 T.E.AnalogVal: 161.86
14:03:54.183 -> 8.75 -178.26 -0.25 129.39 -1.01 L.E.AnalogVal: 149.40 T.E.AnalogVal: 149.40
14:03:54.183 -> 7.21 -178.28 -1.85 126.32 -0.97 L.E.AnalogVal: 137.18 T.E.AnalogVal: 137.18
14:03:54.183 -> 5.77 -178.31 -2.32 121.02 -0.98 L.E.AnalogVal: 125.63 T.E.AnalogVal: 125.63
14:03:54.230 -> 4.12 -178.34 -1.22 135.18 -0.87 L.E.AnalogVal: 112.49 T.E.AnalogVal: 112.49
14:03:54.230 -> 1.75 -178.35 -0.05 192.32 -1.15 L.E.AnalogVal: 93.65 T.E.AnalogVal: 93.65
14:03:54.230 -> -1.29 -178.38 -2.80 249.75 -1.75 L.E.AnalogVal: 69.40 T.E.AnalogVal: 69.40
14:03:54.230 -> -4.33 -178.42 -2.52 249.75 -1.65 L.E.AnalogVal: 45.20 T.E.AnalogVal: 45.20